Search for SUSY signals with τ-leptons in the ATLAS detector

Master Degree Thesis in Experimental Particle Physics

by

Therese Sjursen

Department of Physics and Technology
University of Bergen
Norway

Feb. 2008

Acknowledgments

First of all I want to thank my supervisor Prof. Anna Lipniacka for her excellent inputs and guidance throughout this master thesis. Thank you for giving me the opportunity to visit various schools and conferences, and in this way to introduce me to the particle physics community, and for always having time for answering my questions. I also want to thank Prof. Per Osland for providing me with the theoretical framework of particle physics through his courses. Especially I would like to thank you for setting up an extra course spring 2007, introducing us to supersymmetry.

The analysis performed in Chapter 7 in this thesis has been carried out in collaboration with Alex Kastanas. Thank you Alex, for all your help with programming, useful discussions and for being so patient. It has been great fun working together with you! I am also very grateful to Øysten Djuvsland for excellent help with programming. My other colleague students, Hilde Skjerdal, Maren Ugland and Øyvind Sætre deserve a special thanks as well; for constant support, and good times.

Finally, I want to thank my parents for all their support, and most of all I want to Christian: Thank you, simply for your presence!

Therese Sjursen

Contents

Preface

The main topic of this thesis is the study of the discovery potential of the ATLAS detector for SUSY, by considering a supersymmetric decay chain involving two tau leptons. In supersymmetric models where R-parity is conserved, the lightest supersymmetric particle (LSP) is stable. This makes the LSP a natural candidate for dark matter if it is electrically neutral. Thus, in this case the LSP will escape detection, complicating the task of determining sparticle masses. The end-point of the invariant mass distributions of the visible particles in the decay chain will contain information on the masses of the supersymmetric particles involved in the decay chain. We have investigated the end-point of the invariant mass distribution of the two taus originating from the process $\widetilde{\chi}_2^0 \to \widetilde{\tau}\tau \to \tau\tau\widetilde{\chi}_1^0$ in one benchmark point. Here, the $\widetilde{\chi}_1^0$ is the LSP and the benchmark point under consideration lies in the coannihilation region within the mSUGRA parameter space. This is done with the full simulation of the ATLAS detector, and an inclusive and detailed study of background rejection has been performed.

Due to their short life time, tau leptons can not be detected directly in the ATLAS detector, thus making physics analysis with taus complicated. The tau reconstruction algorithms in ATLAS reconstruct taus from their visible hadronic decay products. The main difficulty in this task is distinguishing these so-called tau-jets from jets originating from QCD processes. In this analysis, we have therefore focused on single-prong taus, since this minimises the contributions from fake reconstructed taus.

...wir müssen uns daran erinnern, daß das, was wir beobachten, nicht die Natur selbst ist, sondern Natur, die unserer Art der Fragestellung ausgesetzt ist.

W. Heisenberg
Physik und Philosophie

Chapter 1

Introduction

Particle physics is the branch of physics that studies the smallest constituents of matter and the interactions between them. The study of symmetries has been an important tool in developing theories describing the physics of these elementary particles, and the current theoretical framework describing it is the *standard model*. Hence, the standard model is a theory built upon the existence and breaking of symmetries. An introduction to this theory is given in Chapter 2, where the importance of symmetries is emphasized. Though, in spite of its success, the standard model is not an ultimate theory. As an example, cosmological measurements give rise to questions that can not be answered with our current understanding of nature; new physics is required. One theory beyond the standard model that can answer some of these questions is supersymmetry (SUSY). The basic concepts of this theory will be discussed in Chapter 3.

Cosmology on the other hand, is the study of the universe as a whole. Cosmological measurements done with the Wilkinson Microwave Anisotropy Probe (WMAP) satellite [1] shows that only 4 % of the universe consists of 'ordinary matter' made up of protons, neutrons and electrons [2]. This type of matter is normally referred to as *baryonic matter*. The rest of the universe is believed to consists of 22 % *dark matter*, and 74 % *dark energy*. Dark energy is a mysterious phenomenon and its nature will not be discussed in this thesis.

Dark matter (DM) is a type of matter that does not emit nor absorb light, thus we can not observe it directly. However, it can be detected via its gravitational effects. In addition to WMAP measurements, the measurement of galactic rotation curves and velocities indicates the existence of DM. The

rotational velocity v of an object on a stable Keplerian orbit with radius r around a galaxy scales like $v(r) \propto \sqrt{M(r)/r}$ where $M(r)$ is the mass inside the orbit [3]. In absence of a dark type of matter, one would expect that the velocity outside the visible part of the galaxy would be $v(r) \propto 1/\sqrt{r}$. Instead one finds that the velocity v is approximately constant for large values of r, where the rotation curves can be measured. The presence of a dark type of matter that can not be 'seen', but has gravitational impact, could explain such a phenomenon. The first evidence of this kind was found already in 1933 by the Swiss astrophysicist Fritz Zwicky. He estimated the mass of the Coma galaxy cluster by measuring the movement of galaxies at the edges of the cluster. He found the measurements to be inconsistent with what was expected from the amount of light emitting matter inside the nebulae he investigated. [4].

Figure 1.1: The picture shows an example of a rotating galaxy. The picture is taken with the Hubble Space Telescope and it shows the M101 Galaxy, located 25 million light years from the earth. The picture is taken from Ref. [5].

Although the existence of DM is by now well established [3], the origin of it is not understood. Astrophysicists suggest that DM may be due to a 'new' type of matter that only interacts weakly with standard model particles. These are often referred to as *weakly interacting massive particles* (WIMPs).

If the DM is a new, or until now undiscovered, type of matter that was produced in the Big Bang, how can we explore its nature? The method of particle physicists is to accelerate particles to high energies before colliding

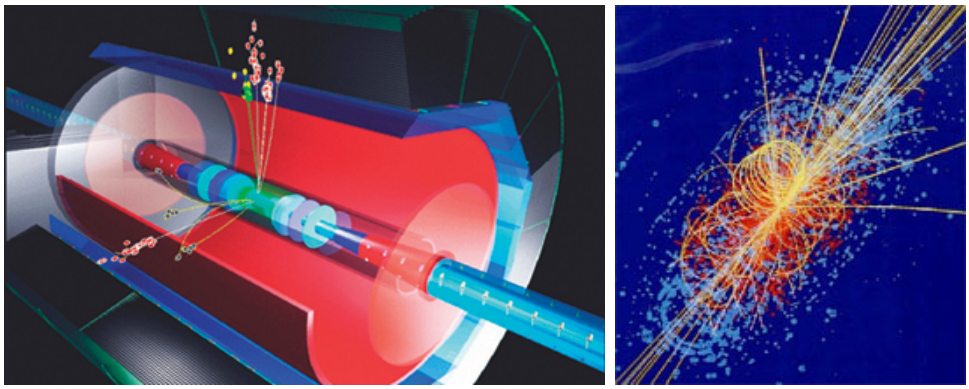

Figure 1.2: The figure to the left shows the basic idea of a particle collider, whereas the figure to the right shows a simulation of two colliding particle beams.

them. In this way one can achieve an energy density, or energy per particle, corresponding to the conditions in a fraction of time after the Big Bang. The new accelerator under construction at CERN, the Large Hadron Collider (LHC) will accelerate protons to collide at a center of mass energy of 14 TeV[1]. This is the highest energy ever reached in an accelerator, and the achieved energy density corresponds to that at a time $\sim 10^{-12}$ s after the Big Bang. This makes the ATLAS detector one of the most exiting places to search for new physics. The LHC and the ATLAS experiment will be introduced in Chapter 4. The LHC is scheduled to have its first proton-proton collision in July 2008.

Monte Carlo simulations play an important role in high energy physics. The study of simulated events helps to understand the complicated physics processes that are to take place in a hadron collider experiment. By analysing simulated events prior to the experiment we may also be prepared for new physics discoveries. An introduction to the tools used for the simulation process and for analysis is given in Chapter 5.

Some supersymmetric models predict the existence of a massive, stable particle. If this *lightest supersymmetric particle* (LSP) is electrically neutral and only interacts through the weak force, it satisfies all the criteria for a WIMP. Hence, SUSY may incorporate a natural candidate for DM in the theory. If supersymmetry is a symmetry of nature, how can we prove its existence? One way may be to determine the masses of supersymmetric particles. In

[1] The commonly used energy unit in high energy physics is electron Volt (eV). 1 eV corresponds to the energy gained by accelerating an electron through a potential difference of one volt.

models where the LSP is electrically neutral, this process is complicated. The LSP will then traverse the ATLAS detector, leaving no signals except for a pronounced amount of missing energy. In models where a symmetry called R-parity is conserved, SUSY particles, or sparticles, are produced in pairs, meaning that one sparticle must decay to another sparticle, which finally decays to the LSP. This enables the study of a SUSY decay chain, where the visible decay products can be used to estimate the masses of the sparticles involved in the decay chain. One method for this is to study end-points of invariant mass distributions.

This thesis investigates the potential for discovering SUSY in one particular benchmark point in a SUSY model called mSUGRA, where the end-point method has been applied. An introduction to the method as well as the results are given in Chapter 7. The analysis in this chapter has been carried out in collaboration with A. Kastanas. An important element in such a study is availability of a reliable reconstruction of the visible particles involved in the decay chain. The decay chain studied in this thesis involves two tau leptons. Physics analysis with taus is complicated, due to the fact that tau leptons can not be detected directly. Thus this study involves a good understanding of the properties of the tau lepton and of the reconstruction process of these in the ATLAS detector. An overview of the properties of the tau lepton, as well as a description of the tau reconstruction algorithms and how they perform is given in Chapter 6. Concluding remarks are given in Chapter 8.

Chapter 2

The Standard Model

Particle physics is the branch of physics that studies the fundamental constituents of matter and the interactions occurring among these elementary particles. Today's theory of particle physics is summed up in the standard model (SM), a theory in well agreement with experimental observations. In spite of its success, the standard model contains some unsatisfying theoretical aspects; it contains at least 19 free parameters and it does not include gravity. This chapter will shortly introduce the basic ideas of the standard model and the mathematical framework describing it.

The standard model is built upon a quantum field theory (QFT), a mathematical framework consistent with both quantum theory and special relativity, in order to describe relativistically moving particles at the smallest possible scale. In the first section, some highlights of the history of particle physics will be mentioned, mainly to introduce the particles included in the standard model. Further, a short introduction to group theory in particle physics will be given, followed by the mathematical description of how to construct a Lagrangian density describing the theory.

2.1 History of particle physics

One may say that the beginning of the history of modern particle physics falls together with the one of quantum theory that started in the beginning of the 20th century. This is related to a phenomenon referred to as black-body radiation [6]. In order to explain the spectrum of black-body radiation, Planck suggested in 1900 that the emission and absorption of radiation in

atoms occurs discontinuously in discrete quanta. Based on Planck's quantum hypothesis, Einstein suggested in 1905 that electromagnetic radiation itself was quantized, i.e. it consists of particles called photons [7]. This interpretation was shown to be consistent with experimental observations such as the photoelectric effect and Compton scattering.

The electron was the first elementary particle to be discovered, although it was not then known to be elementary. It was discovered in 1897 by J.J Thomson in a cathode ray experiment [8]. In 1911 Rutherford proposed his famous atom-model on the background of the observations of his experiments on α-scattering on gold foil [9]; the atom consists of a positively charged massive nucleus surrounded by negatively charged electrons, in analogy with planets orbiting around the sun. Further experiments led to the discovery of the proton in 1919 and the neutron in 1932. During the 1960's a lot of exotic particles were discovered in different collider experiments, leading to the proposal that nucleons have an internal structure, i.e. they consists of particles called quarks.

In 1922, de Broglie proposed a wave-particle dualism, suggesting that a moving particle has an associated wave. The work of Schrödinger, Bohr, Dirac and Heisenberg among others led to the *Copenhagen interpretation* of quantum mechanics that includes Heisenbergs uncertainty principle and the hypothesis that a quantum mechanical state is completely described by a wave function ψ. Heisenberg postulated that measurements of a quantum mechanical system are not deterministic, but must be characterized by a probability distribution. In its most famous form, Heisenbergs uncertainty principle is given mathematically as $\Delta x \Delta p \geq \hbar/2$, i.e. position and momentum can not both be accurately determined at the same time.

From the missing energy in β-decays, Pauli suggested the existence of a neutral light particle, the neutrino in 1930 [10]. The neutrino only interacts through the weak interaction, and it was first detected through experiments as late as in 1956 [11], 26 years after Pauli suggested its existence. Dirac found in his equations negative energy solutions, and he interpreted them as anti-particle states - he postulated the existence of anti-particles in 1928. In 1933 the first anti-particle was indeed observed. The *positron*, the anti-electron, was observed by Anderson in a cosmic ray experiment.

These are just a fraction of the theoretical and experimental discoveries that were done during the last century, leading to our current understanding of matter, summed up in the standard model. The standard model describes all known particles and the interactions occurring among them. It is described

mathematically by a quantum field theory, built upon the work of Dirac, Feynman, Dyson and others.

2.2 Overview

The elementary particles of the standard model can be grouped into fermions of spin 1/2 and bosons of integer spin[1]. The fermions are the particles that make up all matter and bosons are the particles mediating the interactions between fermions[2]. The fermions are divided into leptons and quarks, which again are grouped, according to their masses, in three different generations of similar properties. The fermions can be represented in doublets, due to a symmetry called weak isospin symmetry of the $SU(2)$ group, which will be discussed later in this chapter.

Quarks	$\begin{pmatrix} u \\ d \end{pmatrix}$	$\begin{pmatrix} c \\ s \end{pmatrix}$	$\begin{pmatrix} t \\ b \end{pmatrix}$
Leptons	$\begin{pmatrix} e \\ \nu_e \end{pmatrix}$	$\begin{pmatrix} \mu \\ \nu_\mu \end{pmatrix}$	$\begin{pmatrix} \tau \\ \nu_\tau \end{pmatrix}$
Generation	I	II	III

Table 2.1: The fermions are grouped in three generations of similar properties, according to their masses. Only particles of the first generation are stable.

The *up*-type quarks in the first row (*u (up), c (charm), t (top)*) have electric charge +2/3, whereas the *down*-type quarks in the lower row *(d (down), s (strange), b (bottom))* have electric charge -1/3 of the elementary charge e, where e is the absolute value of the electron charge. The leptons e, μ and τ all have the electric charge $-1e$, and their corresponding neutrinos (ν) are electrically neutral. All particles of the standard model have a corresponding anti-particle. The masses of the quarks span over a wide energy range[3], from $m_u \sim 3$ MeV for the up-quark, to $m_t = 174.2 \pm 3.3$ GeV for the top-quark. The lepton masses range from $m_e \sim 0.5$ MeV for the electron to

[1] Spin is considered as a quantum number, and not as a physical quantity. Spin is given in 'units' of $\hbar$. Throughout this thesis, natural units are applied, i.e. $c = \hbar = 1$.

[2] This is not entirely true; self-interactions between certain bosons may also occur.

[3] In high energy physics, mass is given as $m = \frac{E}{c^2}$. In natural units $c = 1$, so mass is given in the units of energy, i.e in eV.

$m_\tau = 1776.9 \pm 0.3$ GeV for the tau lepton. The neutrinos are considered as massless in the standard model, even though several experiments have found evidence for neutrino oscillation, for which mass is a necessity.

INTERACTION	PARTICLE	MASS [GeV]	CHARGE [e]
Electromagnetic	γ (photon)	0	0
Weak	$W^{\pm}, Z^0$	$\sim$ 81.4, 91.2	$\pm 1, 0$
Strong	8 gluons (g)	0	0

Table 2.2: The table shows the gauge bosons that mediates the interaction between fermions in the standard model.

The particles mediating interactions are represented in Table 2.2. Only charged particles are influenced by the electromagnetic interaction, mediated by the massless spin-1 boson γ, whereas all fermions interact weakly. The quarks have an additional colour charge, called red, blue and green. Due to this they are the only fermions interacting through the strong force, mediated by gluons (g). Quarks are said to have colour, whereas anti-quarks have anti-colour. Gluons have both colour and anti-colour. A free quark has never been observed, but they are observed in bound states called hadrons. A hypothesis of confinement states that only colour neutral particles can exist in nature. Hadrons are either named baryons or mesons, depending on if they consist of three quarks or a quark anti-quark pair respectively. Only particles with integer values of the elementary charge e have been observed in a free state in nature. This means that baryons and mesons have to consist of quarks with electrical charge that adds up to an integer of e, and in addition a colour charge that adds up to zero.

2.3 Group theory essentials

The study of symmetries has been an important tool in developing our current understanding of elementary particles. The importance of symmetries was emphasized already in 1918, by the German mathematician Emmie Noether. She showed that a conservation law can be derived from every continuous symmetry. This is known as Noether's theorem. The standard model is a theory built upon Lagrangian densities which are required to be invariant

under certain transformations, thus is based on the principle of Noether's theorem. Group theory is the mathematical tool for treating symmetries and invariance, and the symmetry groups transforming the standard model Lagrangians are called *gauge transformation groups*. It will be shown in Section 2.4 that the requirement of invariant Lagrangian densities under these gauge transformations leads to the introduction of some vector fields. These fields are interpreted as the fields of the particles mediating interactions in the standard model.

2.3.1 Definition of a group

A group is a set G on which a multiplication operator $\{\cdot\}$ is defined with the following properties [12]:

1. If $x, y \in G$, then $x \cdot y \in G$.
2. There exists an identity element $e \in G$ such that $e \cdot x = x \cdot e = x$ for any $x \in G$.
3. For any $x \in G$, there is an inverse element in G called x^{-1} such that $x \cdot x^{-1} = x^{-1} \cdot x = e$.

A group G is said to be Abelian if the operation is commutative, that is for every x and $y \in$ G, $x \cdot y = y \cdot x$. If this is not true, the group is called non-Abelian. The $U(1)$ group of QED is the only one of the three standard model groups that is Abelian.

2.3.2 Some properties of unitary and special unitary groups

The gauge transformation groups of the standard model are unitary groups, meaning that there exists a representation of the group in terms of complex valued $n \times n$ unitary matrices. A unitary matrix is a matrix satisfying the condition

$$U^{\dagger}U = I_n, \tag{2.1}$$

where I_n is the $n \times n$ identity matrix and $U^\dagger = (U^*)^T$. A unitary group is called special if it satisfies the condition

$$\det U = 1, \tag{2.2}$$

denoted $SU(n)$. The order of a group G is the number of its elements. All the gauge groups of the standard model are hence of infinite order, since they have an infinite number of elements. The $U(1)$ group consists of complex numbers of modulus = 1, i.e. they are of unit length. This implies that the $U(1)$ group is Abelian, which is not the case for the $SU(2)$ and the $SU(3)$ groups. For every group there exists a set of generators S_i, with $S_i \in G$ such that every element $U \in G$ can be written as a product of these. The element U can be written as

$$U = e^{iS_i\chi_i}, \tag{2.3}$$

where χ denotes some complex parameter in general. The generators S of the standard model groups are Hermitian, i.e. $S = S^\dagger$. For the $SU(n)$ groups the generator matrices are also required to be traceless, i.e the sum of the diagonal elements in the matrix should equal zero, $\mathrm{Tr}(S_i) = 0$.

Three gauge symmetry groups are used to describe transformations of particle states in the standard model, $U(1)$, $SU(2)$ and $SU(3)$. This leads to conservation of certain quantum charges of the elementary particles. Quantum Electro Dynamics (QED) is the gauge field theory of electromagnetic interaction occurring among electrically charged fermions. The invariance of the QED-Lagrangian under a symmetry transformation of the $U(1)_Y$ group leads to conservation of electric charge. The weak interaction mediated by massive gauge bosons, $W^\pm$ and Z^0, is described by the $SU(2)_L$ group. At sufficiently high energies (the electroweak scale) QED and the weak interaction are unified in an electroweak theory, described by the symmetry group $SU(2)_L \times U(1)_Y$. This will be described later in this chapter. The $SU(3)_C$ is the basis of the strong interaction, the Quantum Chromo Dynamics (QCD). All these transformation groups lead to conservation of internal symmetries, referred to as quantum charges. Y is the hypercharge of QED, L denotes the left-handed chirality state of weak isospin symmetry, and C is the colour charge of QCD. In addition to the conservation of the quantum charges, which are referred to as internal symmetries, the theory requires an external space-time symmetry in order to conserve energy and momentum (or four-momentum) and angular momentum. Einstein introduced the Poincaré

group in his theory of special relativity for describing these symmetries. The Poincaré group will not be discussed here.

2.4 Gauge theories and invariance in the standard model

2.4.1 QED and the $U(1)$ transformation group

QED is the quantized field theory of the electromagnetic field that was introduced by Maxwell in 1861. Maxwell showed that the eletric field **E** and the magnetic field **B** could be unified, and that they can be written in terms of an unphysical vector potential field $\mathbf{A(x)}$ and a scalar potential field $\phi(x)$,

$$\mathbf{E}(\mathbf{x}) = -\nabla\phi(\mathbf{x}) - \frac{\partial \mathbf{A}(\mathbf{x})}{\partial \mathbf{t}}, \qquad \mathbf{B}(\mathbf{x}) = \nabla \times \mathbf{A}(\mathbf{x}) \tag{2.4}$$

The field $A_\mu(x) = (\phi(x), \mathbf{A}(\mathbf{x}))$ is not unique, i.e. it can be shown that an arbitrary transformation of the field

$$A_\mu(x) \rightarrow A'_\mu(x) = A_\mu(x) + \partial_\mu f(x) \tag{2.5}$$

leaves the physical fields **E** and **B** unchanged. Such a transformation is an example of a $U(1)$ local gauge transformation. In 1928, Dirac formulated the first relativistic quantum field theory, describing a free spin-1/2 particle. For a particle with mass m, represented by a field $\psi(x)$, the free Lagrangian density is given as

$$\mathcal{L} = \bar{\psi}(x)(i\gamma^\mu\partial_\mu - m)\psi(x), \qquad \mu = (0, 1, 2, 3) \tag{2.6}$$

where γ^μ are the Dirac gamma matrices and $\bar{\psi}(x) \equiv \psi^\dagger(x)\gamma^0$. The $U(1)$ group of QED is the gauge transformation group where the transformation operator U acting on a particle state $\psi(x)$ with electric charge q is given as

$$\psi(x) \rightarrow \psi'(x) = U\psi(x) = e^{iqf(x)}\psi(x). \tag{2.7}$$

The function $f(x)$ is here the generator of the transformation group, and locality is implied by $f(x)$ being a function of the space-time coordinate x,

$x = (t, \mathbf{x})$. By requiring the Dirac Lagrangian density, Eq. 2.6, to be invariant under the transformation on the particle state (Eq. 2.7), the derivative ∂_μ must be substituted by a covariant derivative D_μ that couples the electric charge q to the four-vector potential field $A_\mu(x)$,

$$\partial_\mu \rightarrow D_\mu = \partial_\mu + iqA_\mu(x) \tag{2.8}$$

This is known as *minimal substitution* [13]. The field A is interpreted as the photon field, and the new term in the Lagrangian can hence be interpreted as an interaction term between a spin-1/2 particle and a photon. Invariance under the $U(1)$ transformation gives rise to a conserved current given as

$$s^\mu = q\bar{\psi}(x)\gamma^\mu\psi(x) \tag{2.9}$$

which corresponds to the conservation of electric charge. For the electron, $q = -e$.

To obtain the complete Lagrangian density, the free electromagnetic field, i.e the electromagnetic field, A_μ, in absence of charges, must be added to Eq. 2.6 together with the minimal substitution, Eq. 2.8. The complete theory of QED can then be expressed in the Lagrangian density

$$\mathcal{L} = \bar{\psi}(x)(i\gamma^\mu D_\mu - m)\psi(x) + \frac{1}{4}F^{\mu\nu}(x)F_{\mu\nu}(x), \tag{2.10}$$

where

$$F_{\mu\nu} = \partial_\mu A_\nu - \partial_\nu A_\mu \tag{2.11}$$

is the electromagnetic field strength tensor. The fields describing the fermion $\psi(x)$ and the photon $A(x)$ contain annihilation and creation operators that are introduced through a second quantization. It remains to be shown that the theory is renormalizable, but this will not be discussed here. The QED theory looks very elegant and maybe even intuitive through its simplicity. This motivated physicists to search for a similar description of the other interactions included in the standard model.

2.4.2 The electroweak theory and the $SU(2) \times U(1)$ transformation group

The electroweak theory is the unified description of QED and the weak interaction, describing nature at sufficiently high energies, at the order of $E \sim 10^2$

GeV. The theory was introduced in the late sixties by Weinberg, Glashow and Salam. The occurence of massive vector bosons in the theory leads to the introduction of mass terms in the electroweak Lagrangian. This is done via the Higgs mechanism, a mechanism of spontaneous symmetry breaking that will be discussed in more details in Section 2.5.

The weak interaction was introduced as an attempt to describe the nuclear β-decay process, where a neutron decays to a proton, an electron and an anti electron-neutrino.

$$n \rightarrow p + e^{-} + \bar{\nu}_e \tag{2.12}$$

On quark level, this process appears to be flavour changing, i.e. a *down*-quark changes to an *up*-quark by emission of a charged gauge boson. A new theory was needed to explain this phenomenon, and so the field theory of weak interaction was built analogous to the well understood QED. In 1956, Lee and Yang discovered that the weak interaction violates parity, meaning that processes due to the weak interaction are not invariant under spatial reflection [14]. In the following it was indeed shown that parity is violated maximally in all charged current weak processes. To understand this breaking of space symmetry, *chirality* has to be introduced as a property of fermions. Only certain components of particle (anti-particle) states, referred to as handedness or chirality states, participate in weak interactions. These states are called left- and right-handed chirality states, and chirality operators, P^L and P^R, are introduced in order to project out either the left- or right-handed component of a state,

$$\left.\begin{array}{l} \psi^L(x) = P^L\psi(x) \\ \psi^R(x) = P^R\psi(x) \end{array}\right\} = (1 \pm \gamma^5)\psi(x). \tag{2.13}$$

The spin of the particles can be used to define the *helicity* state of particles. For massless particles, helicity and chirality states are the same. A particle is said to be in a right-handed helicity state if it has its spin along the direction of propagation, whereas a particle in a left-handed helicity state has spin opposite to this. Massive fermions consists of both these states, whereas massless fermions only have one helicity state in the SM. Anti-particles have opposite helicity. This invites to an isospinor representation of particles due to their chirality; left-handed neutrinos and charged leptons are combined in a doublet while the right-handed states are treated as singlets.

$$\Psi_l^L(x) = \begin{pmatrix} \psi_l^L(x) \\ \psi_{\nu_l}^L(x) \end{pmatrix}, \qquad \psi_l^R(x) = (\psi_l^R(x)) \qquad \psi_{\nu_l}^R(x) = (\psi_{\nu_l}^R(x)) \tag{2.14}$$

The free Lagrangian density $\mathcal{L}_0$ can then be written as

$$\mathcal{L}_0 = \bar{\Psi}_l^L(x)(i\gamma^\mu\partial_\mu)\Psi_l^L(x)+\bar{\psi}_l^R(x)(i\gamma^\mu\partial_\mu)\psi_l^R(x)+\bar{\psi}_{\nu_l}^R(x)(i\gamma^\mu\partial_\mu)\psi_{\nu_l}^R(x) \quad (2.15)$$

The $SU(2)$ gauge symmetry transformation acts only on particles in left-handed chirality states (right-handed anti-particle states) represented in weak isospinor doublets and leaves the right-handed states unchanged. Analogous to the $U(1)$ gauge transformation of QED, the fields are required to transform as

$$\Psi_l^L(x) \to U(\alpha)\Psi_l^L(x) \equiv e^{i\alpha_j\sigma_j/2}\Psi_l^L(x) \qquad \psi_l^R(x) \to \psi_l^R(x) \qquad (2.16)$$

where σ_j are the Pauli matrices given as

$$\sigma^1 = \begin{bmatrix} 0 & 1 \\ 1 & 0 \end{bmatrix}, \qquad \sigma^2 = \begin{bmatrix} 0 & -i \\ i & 0 \end{bmatrix}, \qquad \sigma^3 = \begin{bmatrix} 1 & 0 \\ 0 & -1 \end{bmatrix} \qquad (2.17)$$

and α_j are some real-valued vectors. The Pauli matrices are the generators of the $SU(2)$ transformation group. The requirement of an invariant Lagrangian density under these transformations leads to the introduction of three conserved currents, $J_i^\alpha(x)$. They are referred to as weak isospin currents and are given as

$$J_i^\alpha(x) = \frac{1}{2}\bar{\Psi}_l^L(x)\gamma^\alpha\sigma_i\Psi_l^L(x), \qquad i = 1, 2, 3. \qquad (2.18)$$

In addition, the corresponding quantities I_i^W called weak isospin charges, given as $I_i^W = \int d^3x J_i^0$, are conserved. The two first currents J_1^α and J_2^α can be written in a linear combination that gives rise to two charged currents, $J^\alpha(x)$ and $J^{\alpha\dagger}(x)$, connecting electrically charged and neutral fields $\psi_l^L(x)$ and $\psi_{\nu_l}^L(x)$. The third current J_3^α is a neutral current that couples left-handed particles of the same type. The three currents are given as

$$\begin{aligned} J^\alpha &= 2[J_1^\alpha - iJ_2^\alpha] = \bar{\psi}_l(x)\gamma^\alpha(1-\gamma^5)\psi_{\nu_l}(x) \\ J^{\alpha\dagger} &= 2[J_1^\alpha + iJ_2^\alpha] = \bar{\psi}_{\nu_l}(x)\gamma^\alpha(1-\gamma^5)\psi_l(x) \\ J_3^\alpha &= \frac{1}{2}[\bar{\psi}_{\nu_l}^L(x)\gamma^\alpha\psi_{\nu_l}^L(x) - \bar{\psi}_l^L(x)\gamma^\alpha\psi_l^L(x)] \end{aligned} \qquad (2.19)$$

The neutral third current has a similar structure as the electromagnetic current given in Eq. 2.9. This was a first hint indicating that the electromagnetic and the weak interaction could be unified in an electroweak theory, invariant under the transformation group $SU(2)_L \times U(1)_Y$. These transformation groups, leading to conservation of weak isospin charges I_i^W and weak hypercharge Y respectively, are global phase transformations. In order to generalize from global to local phase transformations, the real vector α needs to be replaced with three real differentiable functions $\alpha(x)$ in the $SU(2)$ transformation and similar for the $U(1)$ group. The local $SU(2)$ and $U(1)$ transformations are given as

$$U(\alpha(x)) = e^{ig_W \alpha_j(x)\sigma_j/2} \qquad U(f(x)) = e^{ig'Yf(x)}, \tag{2.20}$$

respectively. Here g_W is identified with the coupling constant of the weak interactions, Y is the hypercharge, and g' is a second coupling constant of the combined electroweak theory. For the theory to be consistent with experiments, the fields in Eq. 2.15 must be invariant under both these transformations.

To retain an invariant Lagrangian under the transformations given in Eq. 2.20, the derivatives ∂_μ in Eq. 2.15 must be replaced by the covariant derivatives D_μ. The Lagrangian density of the combined electroweak theory is hence given as

$$\mathcal{L} = i\bar{\Psi}_l^L(x)\not{D}\Psi_l^L(x) + i\bar{\psi}_l^R(x)\not{D}\psi_l^R(x) + i\bar{\psi}_{\nu_l}^R(x)\not{D}\psi_{\nu_l}^R(x) \tag{2.21}$$

where $\not{D} = \gamma^\mu D_\mu$, and the covariant derivatives acting on the different fields are given as

$$\begin{aligned} D_\mu \Psi_l^L(x) &= [\partial_\mu + ig\sigma_j W_\mu^j(x)/2 - ig'B_\mu(x)/2]\Psi_l^L(x) \\ D_\mu \psi_l^R(x) &= [\partial_\mu - ig'B_\mu(x)]\psi_l^R(x) \\ D_\mu \psi_{\nu_l}^R(x) &= \partial_\mu \psi_{\nu_l}^R(x) \end{aligned} \tag{2.22}$$

The requirement of an invariant Lagrangian density under the local phase transformations leads to the introduction of four new vector fields; three fields for the $SU(2)$ transformation, denoted $W_i(x)$ and one corresponding to the $U(1)$ transformation, $B(x)$. This is analogous to the three weak currents,

Eq. 2.19, and to the electromagnetic current given in Eq. 2.9. The two fields W_1 and W_2 can be linearly combined, giving rise to two physical fields W_μ and $W_\mu^\dagger$ which are interpreted as the fields of the charged gauge bosons, $W^\pm$. Their fields are given as

$$\begin{aligned} W_\mu(x) &= \frac{1}{\sqrt{2}}[W_{1_\mu}(x) - iW_{2_\mu}(x)] \\ W_\mu^\dagger(x) &= \frac{1}{\sqrt{2}}[W_{1_\mu}(x) + iW_{2_\mu}(x)]. \end{aligned} \tag{2.23}$$

The two remaining fields, W_3 and B are neutral, and can be written as a linear combination of the two Hermitian fields $A_\mu(x)$ and $Z_\mu(x)$ defined as

$$\begin{aligned} W_{3_\mu}(x) &= \cos\theta_W Z_\mu(x) + \sin\theta_W A_\mu(x) \\ B_\mu(x) &= -\sin\theta_W Z_\mu(x) + \cos\theta_W A_\mu(x), \end{aligned} \tag{2.24}$$

where the angle θ_W is referred to as the weak mixing angle, or the Weinberg angle. The fields $A_\mu(x)$ and $Z_\mu(x)$ are interpreted as the photon field of the electromagnetic interaction and the field of the neutral gauge boson Z^0 of the weak interaction respectively. The appearance of a neutral weak current in the Lagrangian is a remarkable result of a theory which aim was to describe nuclear β-decays, Eq. 2.12. This led to the prediction of interactions coupling neutral leptons, like the process $e^+ + e^- \to \nu_\mu \bar{\nu}_\mu$, and to the existence of the neutral vector boson Z^0.

At low energies, the range of the weak force is limited to very small distances as is known from experiments. This implies that the gauge bosons, $W^\pm$ and Z^0, are very massive. Mass terms are introduced to the theory through a breaking of symmetry of the $SU(2)_L \times U(1)$ gauge group. This is done using the Higgs mechanism, and will be discussed in Section 2.5.

2.4.3 QCD and the $SU(3)$ transformation group

Quantum Chromodynamics is the gauge theory of the strong interaction, describing interactions between quarks and gluons, i.e. particles carrying colour charge. It is a non-Abelian gauge theory, described by the $SU(3)_C$

symmetry transformation group. The most remarkable feature of QCD is confinement; colour charged particles can not be isolated, but are bound to exist in colour neutral objects. This feature is experimentally motivated to be valid at energies probed at accelerators. The strong force confine quarks to form doublets or triplets that are colour neutral, and there exist eight gluons mediating this interaction. The metaphor of colour charge and colour neutrality is motivated from the property of visible light; white light consists of all colours of the visible spectrum of the light. There are three colour charges in the theory of QCD, called *red*, *green* and *blue*. Adding all of them together results in a colour neutral object, forming a triplet. The triplets are referred to as baryons. A colour neutral object can also be achieved by adding a colour and its anti-colour. This results in a doublet, referred to as mesons.

The $SU(3)$ transformation group has eight generators, λ_a where $a = 1, ..., 8$, that must satisfy the relationship

$$[\lambda_a, \lambda_b] = 2if_{abc}\lambda_c, \tag{2.25}$$

where f_{abc} denotes some constants, and λ_a are 3×3 matrices. This is satisfied by the eight Gell-Mann matrices (listed in Ref. [12], p.61). The $SU(3)$ transformation acting on a three-component spinor[4] $\psi_q(x)$ is given as

$$\psi_q(x) \rightarrow e^{ig_s\chi^a(x)\lambda_a/2}\psi_q(x) \tag{2.26}$$

q denotes here the flavour of the quark, g_s is the coupling constant of QCD and $\chi^a(x)$ are eight differentiable functions. Following the same procedure as for QED and the electroweak theory, the requirement of the free Lagrangian density $\mathcal{L}_0$

$$\mathcal{L}_0^{QCD} = \sum_q \bar{\psi}_q(x)(i\gamma^\mu\partial_\mu - m_q)\psi_q(x), \tag{2.27}$$

to be invariant under the transformation Eq. 2.26, leads to the introduction of eight vector fields. These are interpreted as the fields of the eight gluons. It can be shown that the total Lagrangian of QCD can be written as

[4] Colour indexes are suppressed for simplicity.

$$\mathcal{L} = \sum_q \bar{\psi}_q(x)(i\gamma^\mu D_\mu - m_q I)\psi_q(x) + \frac{1}{4}F_a^{\mu\nu}(x)F_{a\mu\nu}(x), \tag{2.28}$$

I is here the identity matrix. The field strength tensor $F_a^{\mu\nu}(x)$ of the gluon fields $G_a^\mu(x)$ is given as

$$F_a^{\mu\nu}(x) = \partial^\mu G_a^\nu(x) - \partial^\nu G_a^\mu(x) - g_s f_{abc} G_b^\mu(x) G_c^\nu(x) \tag{2.29}$$

and the covariant derivatives $D^\mu(x)$ are given as

$$D^\mu(x) = I\partial^\mu + ig_s G_a^\mu(x)\lambda_a/2 \tag{2.30}$$

The field strength tensor of the gluon fields given by Eq. 2.29 has an additional last term compared with the field strength tensor of the photon field, Eq. 2.11. This gives rise to a coupling between gluons, meaning that gluons are self-interacting contrary to photons.

2.5 The Higgs Field

As emphasised in Section 2.4.2, the electroweak theory predicts massless leptons and gauge bosons, and hence the mass terms must be introduced otherwise. In order to obtain a renormalizable theory, it is essential to introduce the masses by a mechanism which retains the gauge invariance of the Lagrangian density [13]. The Higgs mechanism of spontaneous symmetry breaking was inroduced in 1964, generalized from the Goldstone Model to be invariant under the local $U(1)$ gauge transformation in order to give mass to charged leptons and the W and Z bosons. The photon, neutrinos, and gluons remain massless [15]. The idea of the Higgs mechanism is that particles acquire masses by interacting with a scalar field, referred to as the Higgs field. The quantum of the Higgs field is the massive Higgs boson. The Higgs boson is the only particle of the standard model that has not yet been observed in experiments. In the following, only a short introduction to the basic idea of the Higgs mechanism will be given, without going into details.

A Higgs field is introduced as a complex scalar field $\phi(x)$,

$$\phi(x) = \frac{1}{\sqrt{2}}(\phi_1(x) + i\phi_2 x) \tag{2.31}$$

with a corresponding Lagrangian density

$$\mathcal{L}_H = [\partial^\mu \phi^\dagger(x)][\partial_\mu \phi(x)] - V(x) \tag{2.32}$$

where $V(x)$ is the Higgs potential given as

$$V(x) = \mu^2(\phi^\dagger(x)\phi(x)) + \lambda(\phi^\dagger(x)\phi(x))^2 \tag{2.33}$$

For the energy of the field to be bound from below, λ must be positive. If in addition, $\mu^2 < 0$ the potential $V(x)$ possesses a local maximum at $\phi(x) = 0$ and a whole circle of absolute minima at

$$\phi(x) = \phi_0(x) = (\frac{-\mu^2}{\lambda})^{1/2} e^{i\theta} \tag{2.34}$$

where the phase angle θ defines a direction in the complex ϕ-plane [13].

In field theory, the state of lowest energy is the vacuum. Spontaneous symmetry breaking is only relevant to field theory if the vacuum state is non-unique, as is the case here. The form of the potential is shown in Figure 2.1 where the Higgs potential has a so-called *Mexican hat shape*. In a 2-dimensional plane of the value of a complex field, the lowest energy state forms a circular valley.

The symmetry is spontaneously broken if one particular direction θ is chosen to represent the vacuum ground state. This shows the idea of spontaneous symmetry breaking. To apply this to the electroweak theory, the Higgs field is introduced as an isospin doublet of two complex scalar fields transforming under the $SU(2)_L \times U(1)_Y$ symmetry group. The Lagrangian is again required to be invariant under this transformation. Omitting all details, a very simplified description of the process is to follow the same procedure on obtaining the invariant Lagrangian. Using the gauge freedom of the $SU(2)_L \times U(1)_Y$-group (called *unitary gauge*), one ends up with a real massive vector field. This is quantized as the neutral massive Higgs boson. Readers interested in a detailed description of the Higgs mechanism are referred to Chapter 13 and 14 of Ref. [13].

Figure 2.1: The so-called Mexican hat potential describing the spontaneous symmetry breaking of the electroweak theory.

2.6 Shortcomings of the standard model

Although the SM shows an astonishing agreement with experimental data, it can not be the full explanation of our universe. A theory of everything (TOE) is still searched for. In the following, some of the problems and shortcomings of the standard model will be listed.

1. *Many free parameters*: The standard model contains at least 19 free parameters that need to be integrated in the theory by experimental data. This includes the masses of the fermions and the massive vector bosons, the weak mixing angle θ_W, and three gauge coupling constants of the standard model forces among others.

2. *The flavour problem*: The standard model does not explain why there are three families of fermions or why there are so many different flavours.

3. *Symmetry questions*: There is no underlying symmetry implying why the electron-charge and the proton-charge is the same, or why lepton and baryon numbers are being conserved in all experimental processes.

4. *CP-violation*: The origin of CP violation, or an asymmetry in the amount of matter and anti-matter, is not understood.

5. *Gravitation*: It is not known how to include the gravitational force in the theory, thus the standard model cannot be an ultimate theory describing all phenomena in nature.

6. *Hierarchy problem*: Measurements of the properties of the weak interaction predicts the mass of the Higgs boson roughly to be in the order of $m_H^2 \sim (100 \text{ GeV})^2$. Radiative corrections to the Higgs mass in form of vacuum polarization diagrams are within the standard model framework several order of magnitude higher than the predicted mass. This is known as the *hierarchy problem*. The Higgs mass is sensitive to loop corrections of every SM particle it couples to. Contributions from loop diagrams with the different particles depends on a renormalization cut-off scale. As an example, the corrections it gets from a fermion which couples to the Higgs field with λ_f is

$$\Delta m_H^2 = -\frac{|\lambda_f|^2}{8\pi^2}\Lambda_{UV}^2 + \cdots \quad (2.35)$$

[5]

where Λ_{UV} is an ultra violet cut-off parameter used to regulate the loop integral, i.e. to make the loop integral finite, and it is interpreted as the energy scale at which new physics enters to regulate the high-energy behaviour of the theory [16]. If Λ_{UV} is of the order of the Planck scale[6] the quantum corrections to m_H^2 are about 30 orders of magnitude larger than the predicted value $m_H^2 \sim (100 \text{ GeV})^2$. Loop corrections from bosons have the same structure as Eq. 2.35, but with a coupling constant λ_b and they are of opposite sign. In principle, this allows for a cancellation between the contributions Δm_H from bosons and fermions, but this involves an extreme fine-tuning of the masses of the standard model particles. This is often referred to as the *fine-tuning problem*.

7. *Energy density in the universe*: Astrophysical observations such as the rotational speed of galaxies and measurements of microwave background radiation done with WMAP satellite indicates the existence of

[5] The dots represents higher order radiative corrections.

[6] The Planck scale, at the order of $\sim 10^{19}$ GeV, is the scale at which quantum effects of gravity become compatible with the standard model interactions.

a huge amount of non-luminous matter. In fact the baryonic matter of the standard model particles can only account for 4% of the total energy in the universe. The remaining 96 % are divided in dark matter, 22 %, and dark energy, 74 %. The dark matter does not interact electromagnetically, i.e. it does not absorb or emit light, but it can be measured indirectly through its gravitational influence. The dark energy on the other hand is a bigger mystery. It has a negative pressure and in that way it acts as an anti-gravity. The dark energy is believed to be responsible for the increasing expansion of the universe. The standard model has no candidate for dark matter and has no explanation for dark energy.

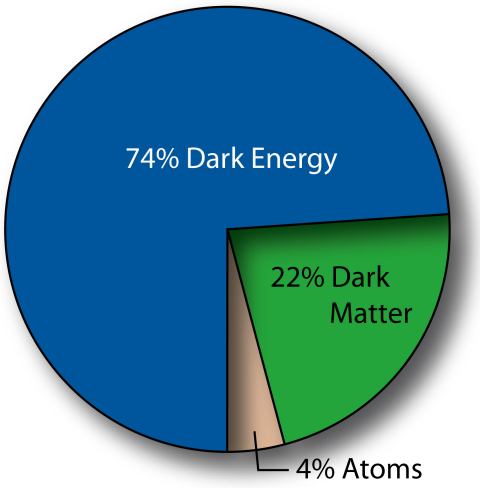

Figure 2.2: The energy density in the universe shown in a cake diagram. The baryonic matter made up from the standard model particles only makes up 4 % of the total amount of energy in the universe.

8. *Grand unification*: The coupling constants for the three standard model interactions appear to be changing with energy. For aesthetic reasons, it would be satisfying to see a unification of the three interactions at some energy scale. This would also reduce the number of free parameters in the theory, discussed above. The theory where the unifying of the SM couplings occur is called the Grand Unified Theory (GUT) and the energy scale at which they unify is referred to as the GUT scale.

Figure 2.3 shows the extrapolation of the inverse of the three standard

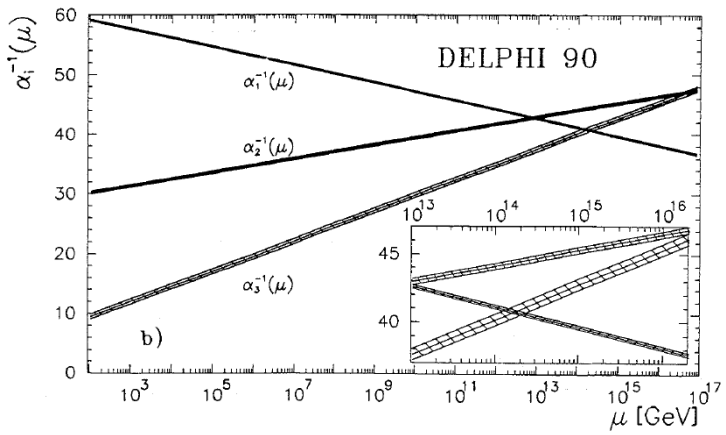

Figure 2.3: The figure shows the extrapolation of the inverse of the three standard model coupling constants to high energies. The figure is taken from Ref. [17].

model coupling constants to high energies. The tend towards unification may be seen as an indication for some new physics.

Chapter 3

Supersymmetry

As mentioned at the end of Chapter 2, the standard model is not an ultimate theory. Some serious questions need to be answered, and some new physics are required to do so. This chapter will focus on one of the theories beyond the standard model, namely supersymmetry (SUSY). Supersymmetry is a theory predicting that nature is symmetric under the interchange of the spin-1 force carriers (bosons) and the spin-1/2 mass particles (fermions), and it is today the most promising extension of the standard model. This chapter will give a short phenomenological introduction to supersymmetry, concentrating on the *minimal supersymmetric extension of the standard model* (MSSM). Starting with a general introduction to supersymmetry, followed by mentioning some motivations for believing that supersymmetry might be realized at the TeV-scale, the basic structure and the idea of supersymmetry breaking, will be given. At the end of this chapter, the observability of SUSY within a certain model (mSUGRA) will be discussed.

3.1 Introduction and overview

In Chapter 2 concerning the standard model, only internal symmetries where discussed. However, the particles also exhibit external space-time symmetries for rotation, boosts and translation in four-dimensional space-time. This was introduced by Einstein in the special theory of relativity, and the Poincaré group is the symmetry group that describes all external symmetries in relativistic field theories. Supersymmetry is a generalization of the space-time symmetry of QFT that transforms fermions into bosons and vice versa. Historically, the introduction of supersymmetry was based on an attempt to

unify these internal and external symmetries. In 1967, Coleman and Mandula proved the *no-go* theorem that, under certain assumptions, states the "impossibility of combining space-time and internal symmetries in any but a trivial way" ([18], p. 1251). Though, in 1974 it was shown by Haag, Łopuszánski and Sohnius that by weakening some of the assumptions, allowing both commuting and anticommuting symmetry generators, there is a nontrivial extension of the Poincaré algebra, namely the supersymmetry algebra:

> Recently, Wess and Zumino discovered field theoretical models with an unusual type of symmetry [...] which connects Bose and Fermi fields and is generated by charges transforming like spinors under the Lorentz group. These spinorial charges give rise to a closed system of commutation-anticommutation relations, which may be called "a pseudo Lie algebra". It turns out that the energy-momentum operators appear among the elements of this pseudo Lie algebra, so that in some sense a fusion between internal and geometric symmetries occur. ([19], p. 257)

In other words, Haag, Łopuszanski and Sohnius found that by "expanding" the definition of the Lie algebra, a fusion of internal and external symmetries could be obtained. The pseudo Lie algebra (normally called a graded Lie algebra, or a Lie superalgebra) defines the structure of this new symmetry group. Since the Poincaré algebra is a Lie algebra, it can then be generalized to a Poincaré superalgebra, defining the algebra for sypersymmetric transformations.

The basic idea of supersymmetry is the existence of fermionic charges Q that relate bosons to fermions [20] that, in a very simplified version, transforms as

$$Q|Boson\rangle = |Fermion\rangle \qquad Q|Fermion\rangle = |Boson\rangle \tag{3.1}$$

These charges Q are the spinorial generators of the supersymmetric transformations. With P^μ being the energy-momentum generators of space-time translations, the generators Q and its hermitian conjugate $Q^\dagger$ must satisfy the following algebra of commuting and anti-commuting relations[1] [16],

[1] Spinor indices are suppressed for simplicity.

$$\begin{aligned} \{Q, Q^\dagger\} &= P^\mu \\ \{Q, Q\} &= \{Q^\dagger, Q^\dagger\} = 0 \\ [P^\mu, Q] &= [P^\mu, Q^\dagger] = 0 \end{aligned} \tag{3.2}$$

This algebra is then the extension of the Poincaré algebra to contain anti-commuting fermionic operators. Thus, the original attempt to unify internal and external symmetries resulted in an expansion of the external space-time symmetry group, leaving the internal symmetries out.

3.1.1 Motivations for SUSY at the TeV-scale

The main motivation for expecting supersymmetry at an energy-scale $\lesssim 1$ TeV is that it would provide an elegant solution to the mass hierarchy problem discussed in Section 2.6. The minimal supersymmetric extension of the standard model, the MSSM, predicts one supersymmetric partner to every standard model particle that differs by half an integer spin. Since bosonic and fermionic loop corrections to the Higgs mass are of opposite sign, the corrections cancel if there are equal numbers of bosons and fermions with identical couplings. Recall the fermionic loop correction[2] given in Eq. 2.35,

$$\Delta m_H^2 = -\frac{|\lambda_f|^2}{8\pi^2}\Lambda_{UV}^2 + \cdots \tag{3.3}$$

For bosons with a coupling λ_B to the Higgs, the loop correction is given as

$$\Delta m_H^2 = \frac{\lambda_b}{8\pi^2}\Lambda_{UV}^2 + \cdots \tag{3.4}$$

The coupling constant λ_b must be positive for the potential to be bound from below. In an MSSM world, the higher order corrections to the Higgs mass would cancel if $|\lambda_f^2| = \lambda_b$. This can be achieved without fine-tuning if the supersymmetric masses lie at the TeV-scale.

Another consequence of introducing SUSY at the TeV-scale, is that it could provide a unification of the standard model gauge couplings at an energy scale $M_{GUT} \sim 10^{16}$ GeV. This is illustrated in Figure 3.1, where the standard model forces are extrapolated to high energies. The graph shows the extrapolation of the inverse of the SM coupling constants to high energies.

[2] The dots represents higher order radiative corrections.

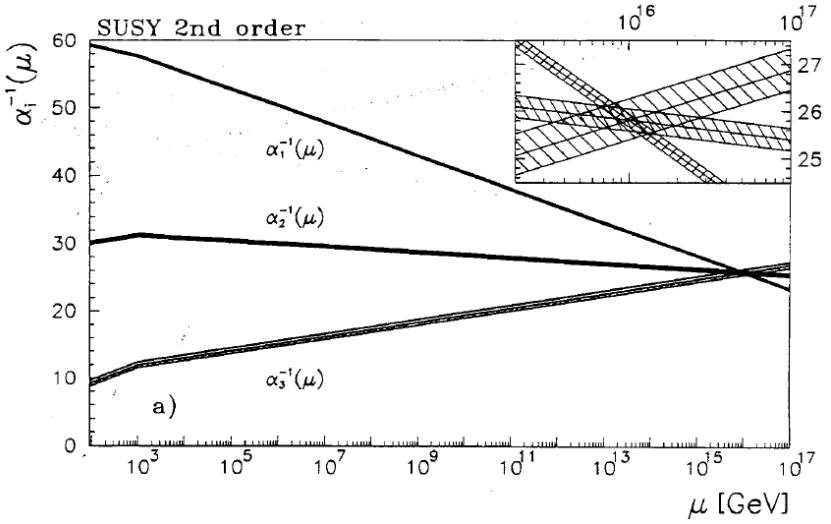

Figure 3.1: The plot shows the extrapolation of the inverse of the three standard model coupling constants. The plot is taken from Ref. [17].

A third motivation for SUSY is that it can incorporate a natural candidate for dark matter (DM) to the theory. Since DM particles are 'dark', they should be electrically neutral and not interact through the electromagnetic interaction. Direct DM searches also indicate that it can not interact through the strong interaction. Hence the only SM interaction DM particles may be exposed to is the weak interaction. Such particles are often referred to as *weakly interacting massive particles* (WIMPs). In order to make up for the dark matter observed in the universe today, the DM particles should be non-relativistic. This indicates that sparticles have high masses.

3.2 Basic structure of the MSSM

The MSSM is the supersymmetric extension of the standard model with minimal particle content. Assuming the existence of only one set of transformation generators, $\{Q, Q^\dagger\}$, leads to the introduction of one *superpartner* to every standard model particle. This is often referred to as $N = 1$ supersymmetry, and the superpartners are referred to as *sparticles*. The sparticles and the corresponding SM particles are identical in every aspect except for spin, and they are organised in supermultiplets. The superpartners of the SM fermions are scalar particles with spin-0, and they are described by chiral

superfields. The scalar fermions, or *sfermions* are grouped in *sleptons* and *squarks*. The superpartners of the gauge bosons and the Higgs bosons[3] have spin 1/2, and are referred to as *gauginos* and *higgsinos*. Table 3.1 lists the particles of the MSSM. The SUSY particles are distinguished from their SM partners by placing a tilde over the particle symbol.

Name	**Multiplet**	**Spin 0**	**Spin 1/2**	**Spin 1**	$SU(3)_C, SU(2)_L, U(1)_Y$
squarks, quarks (3 families)	Q $\bar{u}$ $\bar{d}$	$(\widetilde{u}_L \quad \widetilde{d}_L)$ $\widetilde{u}_R$ $\widetilde{d}_R$	$(u_L \quad d_L)$ u_R d_R		(3, 2, +1/6) (3, 1, -2/3) (3, 1, +1/3)
sleptons, leptons (3 families)	L $\bar{e}$	$(\widetilde{\nu}_L \quad \widetilde{e}_L)$ $\widetilde{e}_R$	$(\nu_L \quad e_L)$ e_R		(1, 2, 1/2) (1, 1, 1)
Higgs, higgsinos	H_u H_d	$(H_u^+ \quad H_u^0)$ $(H_d^0 \quad H_d^-)$	$(\widetilde{H}_u^+ \quad \widetilde{H}_u^0)$ $(\widetilde{H}_d^0 \quad \widetilde{H}_d^-)$		(1,1,+1/2) (1,1,-1/2)
gluino, gluon winos, W-bosons bino, B-boson	G W B		$\widetilde{g}$ $\widetilde{W}^\pm \quad \widetilde{W}^0$ $\widetilde{B}^0$	g $W^\pm \quad W^0$ B^0	(8, 1, 0) (1, 3, 0) (1, 1, 0)

Table 3.1: The particles of the MSSM. The squarks and sleptons, which have spin = 0, are labeled with L and R; this refers to the helicity states of their SM partner.

It follows from the supersymmetry algebra, Eq. 3.2, that all particles within a multiplet must have the same mass. It should be noted that the table lists two Higgs doublets. This is required by the MSSM in order to give mass to all particles. The H_u doublet gives mass to *up*-type quarks and the H_d to the *down*-type quarks. The gauginos and higgsinos mass eigenstates will mix due to effects from electroweak breaking and SUSY breaking. This results in four neutral and two charged mass eigenstates, referred to as *neutralinos*, $\widetilde{\chi}_i^0$, and *charginos*, $\widetilde{\chi}_j^\pm$.

[3] Supersymmetry requires the introduction of a second Higgs doublet in order to give mass to all particles in the MSSM.

3.2.1 R-parity

A general supersymmetric Lagrangian will contain gauge-invariant terms that can violate lepton and baryon number conservation. In order to regain this conservation, a new symmetry is introduced, called R-parity, and defined as

$$R = (-1)^{3(B+L)+2s} \tag{3.5}$$

where B is the baryon number, L denotes the lepton number and s is the spin of the particle. R-parity is a multiplicative symmetry. From the definition it follows that all SM particles have R-parity +1, while all SUSY particles have R-parity -1. If R-parity is exactly conserved, there can be no mixing between particles and sparticles. Furthermore, every interaction vertex in the theory contains an even number of $R = -1$ sparticles. This has three important phenomenological consequences [16]:

- The lightest supersymmetric particle (LSP) must be absolutely stable. If the LSP is electrically neutral and only interacts weakly with ordinary matter, it is an attractive candidate for the non-baryonic dark matter required by cosmology.
- Each sparticle other than the LSP must eventually decay into a state that contains an odd number of LSPs (usually just one).
- In collider experiments, sparticles can only be produced in even numbers.

Violation of lepton and baryon number may cause rapid proton decays. This has never been observed in nature and conservation of R-parity prevents such decays.

3.3 Supersymmetry breaking

If supersymmetry was an exact symmetry of nature, particles and their super partners would be degenerate in mass. Since sparticles have not yet been observed in experiments, the conclusion is that SUSY must be broken if it is to exist. As stated above, one of the main motivations for supersymmetry is that it provides an elegant solution for the mass hierarchy problem. The

breaking of SUSY should hence be carried out carefully in order not to destroy this feature. Such a symmetry breaking is said to be *soft*. SUSY breaking is a rather technical procedure, and no details will be given. A few remarks should though be made.

Within the framework of the MSSM, supersymmetry is believed to be broken spontaneously in a similar manner as the electoweak symmetry breaking. Though, SUSY breaking is believed to occur in a *hidden* sector of particles that have no direct coupling to the *visible* sector of the MSSM particles [16]. The particles of this sector are believed to be very heavy and out of the scope of accelerator research. The breaking is then mediated to the visible sector by a *messenger field*, as illustrated in Figure 3.2.

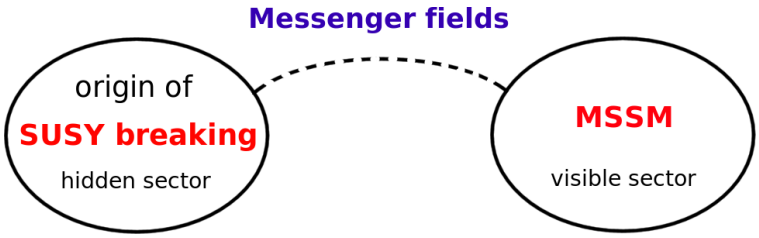

Figure 3.2: An illustration of the process of SUSY breaking in the MSSM.

There exist different mechanisms for transmitting the soft SUSY breaking from the hidden to the visible sector. The most established ones suggest that it is mediated by either gravity (supergravity models), by gauge bosons (gauge mediated supersymmetry breaking models) or by anomalies, i.e. higher order effects (anomalous mediated supersymmetry breaking models). In the following, a short description of the minimal supergravity model will be given, since the analysis of this thesis focuses on this model.

3.3.1 mSUGRA

The most economical mechanism for transmitting the breaking of SUSY to the MSSM fields uses gravitational interaction [21], and the simplest of such models are *minimal supergravity* (mSUGRA) models. The MSSM imposes 105 new parameters to the theory in addition to those of the standard model. Built upon the hypothesis of a grand unification of the coupling constants at a scale $M_{GUT} \simeq 10^{16}$ GeV, the parameter space of mSUGRA models reduces drastically. Assumption of a common scalar mass, a common gaugino mass,

a common trilinear coupling parameter at the GUT scale, and a quantity $\tan(\beta)$ where β is the ratio between the Higgs vacuum expectation values, reduces the number of free parameters to four. In addition, the sign of the Higgs mass parameter is not set. These parameters determine all SUSY masses and couplings. For clarity, the parameters are listed below:

1. A universal gaugino mass at M_{GUT}, denoted $m_{1/2}$,
2. a universal scalar mass at M_{GUT}, denoted m_0,
3. a common value for all trilinear couplings in the Lagrangian, A_0,
4. a quantity $\tan\beta$ introduced as the ratio between the two Higgs doublet vacuum expectation values (VEVs), given as $\tan\beta = \frac{\langle H_d \rangle}{\langle H_u \rangle}$, where H_u gives mass to the up-type quarks and H_d to the down-type quarks,
5. and the sign of the Higgs mass parameter μ.

The mSUGRA model thus limits the parameter space to contain 4 free parameters and a sign. In addition, there exist experimental constrains and bounds, excluding most of the parameter space. In the following, a brief discussion of this will be given.

3.4 Observing SUSY at the LHC

As stated above, a consequence of R-parity conservation is that supersymmetric particles are produced in pairs. This causes the lightest supersymmetric particle (LSP) to be stable and hence an end product of every supersymmetric decay chain. If the LSP is electrically neutral it will escape detection, leaving a pronounced signature of missing energy. Though, missing energy is not enough to state the existence of SUSY.

In mSUGRA models, the parameter space is defined by the 4 parameters and the sign listed above. There are in addition several experimental constraints making the parameter space more manageable in the search for supersymmetric particles. The first constraint is the LEP2 bound on the Higgs mass to be $m_H > 114.5$ GeV. Other constraints include the measurements of the corrections on the muon anomalous magnetic moment, $g_\mu - 2$, and the branching

fraction for the process $b \to s\gamma$ as well as WMAP measurements of the dark matter relic density in the universe. These exclude most of the mSUGRA parameter space. There remains four favoured distinct regions;

- The *bulk region*, a region with relatively low value of the SUSY mass scale.
- The *focus point region*. For $m_{1/2} >> m_0$ there exist a region where the lightest neutralino $\widetilde{\chi}_1^0$ has a significant higgsino component, enhancing the $\widetilde{\chi}_1^0\widetilde{\chi}_1^0$ annihilation cross section.
- The *Higgs funnel region*. For large values of $\tan\beta$ there is a funnel in the parameter space where the mass of the scalar Higgs boson is nearly twice the one of $\widetilde{\chi}_1^0$, enhancing the $\widetilde{\chi}_1^0\widetilde{\chi}_1^0$ annihilation cross section.
- The *coannihilation region*. This region is characterised by a small mass difference between the scalar tau, or the *stau*, and the $\widetilde{\chi}_1^0$ to be $\Delta m \lesssim 5 - 15$ GeV, allowing an annihilation of $\widetilde{\tau}$ and $\widetilde{\chi}_1^0$.

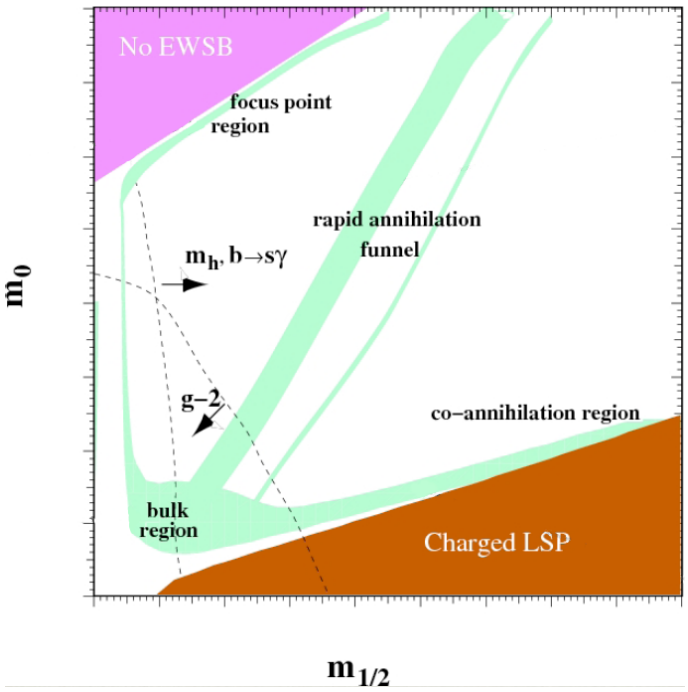

Figure 3.3: The figure shows a qualitative plot of the mSUGRA parameter space, where no mass scales are introduced. The figure is taken from Ref [22].

Figure 3.3 shows a sketch of the regions where the density of the lightest neutralino is consistent with the WMAP measurements of the amount of DM in the universe today.

In the search for SUSY, measurement of sparticle masses is an important task. A frequently used method for this, and also the method used in the analysis of Chapter 7 in this thesis, is the end-point method, where end-points of invariant mass distributions are calculated. A typical decay chain well adapted for this method is

$$\widetilde{q} \rightarrow \widetilde{\chi}_2^0 q \rightarrow \widetilde{l} l q \rightarrow \widetilde{\chi}_1^0 l l q \tag{3.6}$$

This will be discussed in Chapter 7, but the basic idea is to calculate the theoretical end-point and then to compare this with the end-point of invariant mass distributions obtained by analysing simulated data. When real data is available, the end-point of the invariant mass distributions in simulated data can be compared with the results obtained with real data. To study the process given in Eq. 3.6, two criteria have to be fulfilled. First of all, the mass hierarchy must allow the decay chain, and secondly, the cross section for the entire process should be large enough to allow analysis [23].

Chapter 4

The Experiment

The experimental tools in particle physics are mainly particle accelerators, and detectors to investigate what happens in the interaction point of two colliding particle beams. This chapter will shortly introduce the largest particle physics laboratory in the world, CERN, and give an overviewable description of the Large Hadron Collider (LHC) and the ATLAS detector.

4.1 CERN

The European Organization for Nuclear Research CERN (Conseil Europen pour la Recherche Nuclaire) is the world largest particle physics laboratory, and it is situated on the Swiss/French border just outside Geneva. CERN was established and founded by 12 member states in 1954. Today the number of member states has grown to 20, and 35 other states are involved in CERN projects. Throughout the years, several important discoveries and achievements have been made at CERN in a wide range of experiments. The first accelerators, the Synchro Cyclotron (SC) and the Proton Synchrotron (PS) became operative in 1957 and 1959 respectively. The SC accelerated protons to an energy of 600 MeV, and pion decays, such as $\pi^- \rightarrow e^-\nu$ and pion 'beta decay' $\pi^+ \rightarrow \pi^0 e^+ \nu$, were observed for the first time. The PS were using a method of alternating gradient (AG) focusing principle for providing a dipole magnet field for bending the beams, which allowed for a much higher energy to be reached. The protons were accelerated to an energy of 28 GeV. An upgraded version of the PS is still in use, and serves as a part of the injector system for a number of accelerators [24]. Figure 4.2 shows an overview

of the existing injector system that will be used to pre-accelerate the particles for the LHC experiments. An On-Line Isotope Mass Separator facility (ISOLDE), a facility mainly dedicated to the production and investigation of exotic nuclei, conducted its first experiment in 1967. ISOLDE was using the SC until 1990, before the Proton Synchrotron Booster (PSB) was introduced as a part of the facility in 1992 [25]. In 1976, the Super Proton Synchrotron (SPS) started running, and in 1989 the 27 km long Large Electron Positron Collider (LEP) was completed and installed in a circular tunnel 100 m underground. These and other accelerators with different corresponding detectors have led to the discovery of many new particles and phenomena in particle physics. The perhaps most important achievements made at CERN are the discoveries of Charge-Parity (CP) violation and of the vector bosons of weak interaction. The SPS accelerator was originally colliding protons accelerated up to an energy of 450 GeV. In 1981 it was converted to collide protons with anti-protons, and in 1983 the first signatures for the theoretically predicted vector bosons Z and W were seen. The e^+e^- LEP collider started its runs in 1989 with a center of mass energy of 90 GeV, and throughout its run-time it produced large quantities of Z and W bosons. In 2001, the NA48 collaboration announced the confirmation of the existence of direct CP violation [26]. NA48 was an experiment using the SPS accelerator. When the LHC starts to be operative in 2008, we hope to discover supersymmetry, or some other new physics that can give answers to some of the many unsolved questions of particle physics.

4.2 The Large Hadron Collider

The Large Hadron Collider (LHC) is a 27 km long synchrotron storage ring installed in the old LEP tunnel. It is built mainly to collide protons at a center of mass energy of 14 TeV, the highest energy ever reached in an accelerator. The design luminosity of LHC is 10^{34} cm^{-2}s^{-1}. With a bunch crossing rate of 40 MHz, the proton bunches will collide every 25 ns. Each bunch contains $\sim 10^{11}$ protons, and on average 23 interactions will occur in each bunch crossing. In addition to proton-proton collisions, the LHC will also collide heavy nuclei such as lead and gold nuclei. LHC is scheduled to have its first $p-p$ collision in July 2008.

Four main experiments are to take place at the LHC-ring. Figure 4.1 shows their location. The ALICE experiment(A Large Ion Collider Experiment) is mainly dedicated to the study of quark-gluon plasma. This high energy den-

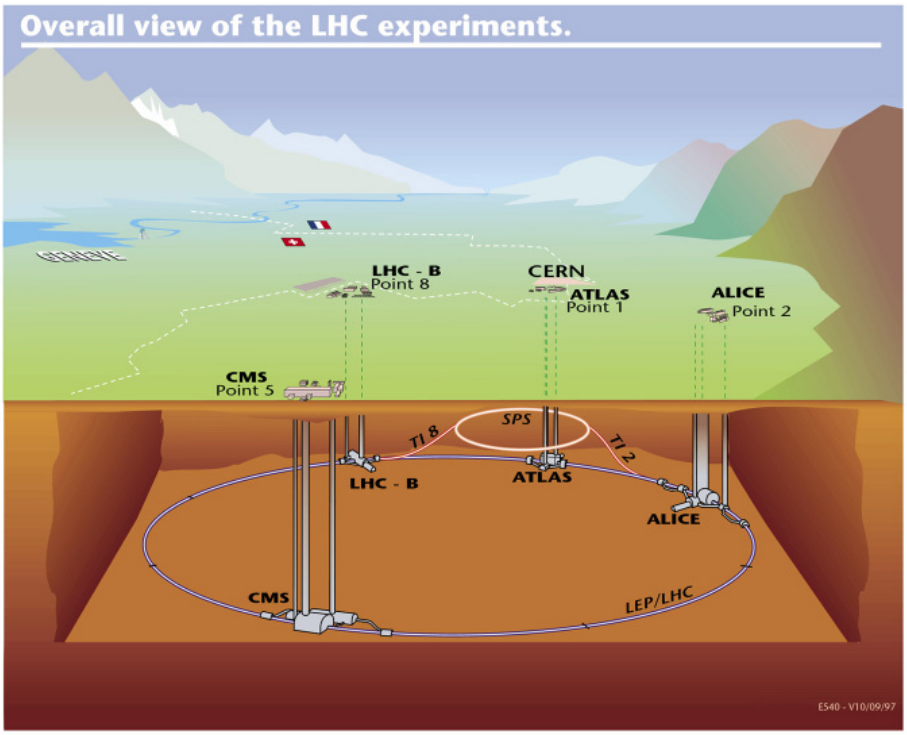

Figure 4.1: The figure shows the LHC storage ring and the location of the four main experiments taking place.

sity phase of matter will be studied by colliding heavy ions. This is the only nuclear physics experiment at the LHC. LHCb is a smaller experiment, which main purpose is to study CP-violation and rare B-meson decays. The CP violation occurring in the weak interaction is still a mysterious phenomenon, and the LHCb experiment will hopefully provide more information on this topic. The Compact Muon Solenoid (CMS) detector and the ATLAS detector are the two largest experiments at the LHC. Both of them are so called general purpose detectors, and they will serve as validational partners of each others measurements.

The high beam intensities implied by a luminosity of 10^{34} $\mathrm{cm}^{-2}\mathrm{s}^{-1}$ exclude the use of anti-proton beams and one common vacuum and magnet system for both circulating beams (as it is done at TEVATRON) and implies the use of two proton beams [27]. The LHC is hence designed to collide two equally charged particles with separate magnet fields and vacuum chambers, with only common sections at the interaction points where the detectors are located. The complicated magnet system uses twin bore magnets consisting

of two sets of coils and beam channels within the same mechanical structure and cryostat. The superconducting dipole magnets will have a maximum field strength of 8.65 T. They are cooled to a temperature below 2 K by super-fluid Helium, a temperature comparable to that in outer space. Since accelerated charged particles will loose energy in form of radiation, there is a limitation on the reachable energy. Though, due to the large mass of the proton (compared with electrons that were accelerated in the LEP machine), energy losses due to synchrotron radiation effect are small in a circular accelerator with a radius of 4 km. Hence, the limitation on reachable energy at the LHC is the strength of the magnets.

The LHC will be supplied with protons from the existing injector chain comprising Linac, booster, the PS and the SPS [27]. Figure 4.2 shows an overview of the CERN injector system. Linac accelerates the protons to an energy of 50 MeV, the booster up to 1 Gev, PS to 26 GeV and the SPS up to 450 GeV. Protons with an energy of 450 GeV will then be injected in the LHC ring where they will be accelerated to an energy of 7 TeV. The whole sequence will take approximately 400 seconds.

4.3 The ATLAS detector

ATLAS (A Toroidal LHC AparatuS) is the largest detector at the LHC ring, and it is located at point 1 on Figure 4.1, just across the road from the CERN site. ATLAS is a general purpose detector, meaning that it is designed to enable studies in a wide range of physics processes and phenomena foreseen at the TeV-scale. Its design is therefore focused to provide well-preformed information at all detector levels. The ATLAS detector consists of four main parts; three sub-detector systems and a magnet system. Figure 4.3 shows a sketch of the ATLAS detector, where the sub-systems are indicated with different colours. The three detector systems are the inner detector tracker, the calorimeters and the muon spectrometer. The inner detector tracks charged particles precisely, the calorimeters measure the energy of (easily) stopped particles, the muon spectrometer assists in identifying and in energy measurement of muons. The magnet system bends charged particles, allowing their momenta to be measured. Neutrinos are the only well established particles that cannot be probed in the ATLAS detector. Figure 4.7 shows a cross-section view of the detector in a transverse $x-y$ plan at $z = 0$, indicating where the different types of particles will be detected. In the following, the geometry of the ATLAS detector will be described, followed by a short

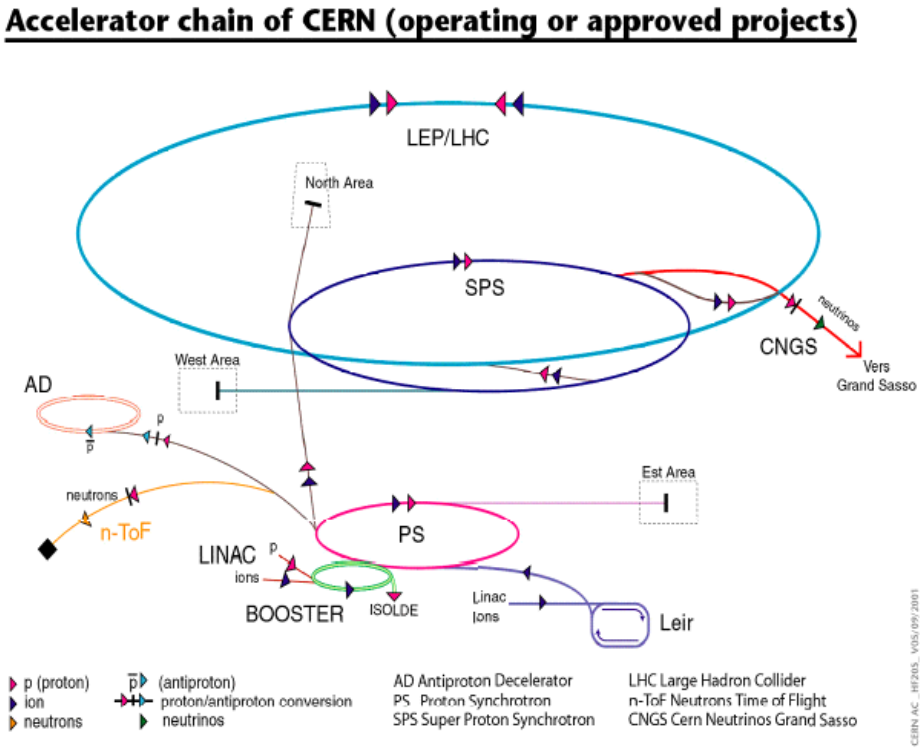

Figure 4.2: The injector system. LHC will be supplied with protons pre-accelerated in the injector system, where Linac accelerates the protons to an energy of 50 MeV, the booster up to 1 Gev, PS to 26 GeV and the SPS up to 450 GeV. Protons with an energy of 450 GeV will then be accelerated to an energy of 7 TeV in LHC.

description of the sub-detectors and the trigger system of ATLAS.

4.3.1 Geometry

The detector has a right-handed coordinate system, where the beam direction defines the z-direction and the positive x-axis is defined to point from the interaction point towards the center of the LHC ring [29]. This determines the positive y-axis to point upwards. The azimuthal angle ϕ is measured around the z-axis and the polar angle θ is the angle from the z-axis. The pseudorapidity, defined as

$$\eta = \ln \tan \frac{\theta}{2}, \tag{4.1}$$

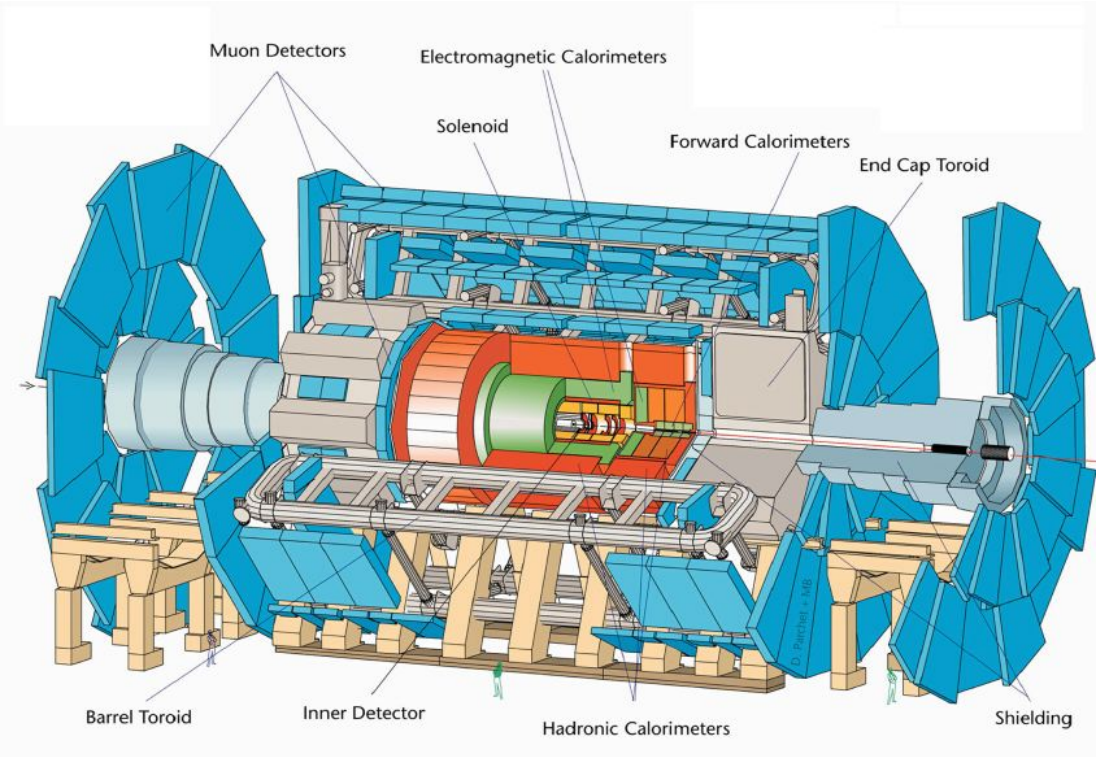

Figure 4.3: Overview of the ATLAS detector. The different colours refers to different sub-detector systems. The dimensions of the detector are 25 m in height and 44 m in length. The overall weight of the detector is approximately 7000 tonnes. The figure is taken from Ref. [28].

is introduced as a spatial coordinate to indicate closeness to the beam, i.e. to describe the angle of a particle relative to the beam axis. For $\theta = 0°$, $\eta = \infty$ and $\theta = 90°$ corresponds to $\eta = 0$. This means that particles traveling along the beam axis have high values for $|\eta|$. In high energy physics, the pseudorapidity is preferred as a coordinate instead of the polar angle.Many new physics scenarios are characterised through a signature of missing energy in the event. For this reason a good hermeticity is required, which include high η-coverage.

The general layout for the ATLAS detector is that of a barrel structure along the beam which is centered at the interaction point, with end-caps in the region for large values of the pseudorapidity in the ATLAS coordinate system. This structure is repeated for all detector layers.

4.3.2 Inner Detector

Approximately 1000 particles will emerge from the collision point every 25 ns in the region $|\eta| < 2.5$ [30]. To cope with this large track density, a good tracking system witch enables high-precision measurements is required. Closest to the collision point, the Inner Detector (ID) is located. The ID tracks charged particles from the LHC beam-pipe to the electromagnetic calorimeter system, and it consists of three different sub-systems which will be introduced in the following.

The Pixel Detector [31]

The pixel detector is designed to provide a very high-granularity, high-precision set of measurements as close to the interaction point as possible. It has three precision layers, and consists of approximately 80.4 million detector elements, with read-out channels for each element, to cope with the large density of tracks. The detecting material is silicon. The pixel detector mostly determines the impact parameter[1] resolution and the ability of the ID to find short-lived particles such as τ leptons and B-hadrons. A charged particle will typically leave three signals in the pixel detector, due to the three layers.

The Semiconductor Tracker

The Semiconductor Tracker (SCT) consists of eight layers of silicon microstrip detectors. The system is designed to give eight precision measurements per track, contributing to the measurement of momentum, impact parameter and vertex position. The SCT also provides good pattern recognition, due to its high granularity. The detector contains 61 m^2 of silicon strips and the total number of read-out channels in the SCT is approximately 6.3 million.

Both the pixel and the SCT have a pseudorapidity coverage $|\eta| < 2.5$ [30].

The Transition Radiation Tracker

The Transition Radiation Tracker (TRT) is a straw tube detector which gives a large number of tracking points, typically 36 per track in the barrel region.

[1] The impact parameter is defined in Section 4.4.6

The straws are filled with a gas mixture of 70% Xenon, 27% CO_2 and 3% O_2, and each straw is 4 mm in diameter. The barrel of the detector consists of 50 000 straws, each divided in two at the center, in order to reduce the large occupancy at the LCH design luminosity, and readout at each end. The end-caps contain 320 000 straws, with the readout at the outer radius. The TRT has a pseudorapidity coverage $|\eta| < 2.0$ [30].

4.3.3 The ATLAS Central Solenoid

The central solenoid (CS) surrounds the ID, providing it with a magnetic field of 2 T. This results in a deflection of charged particles in the transverse plane in the ID, allowing their momenta to be measured.

4.3.4 The Calorimeters

The calorimeters are mainly dedicated to energy measurements, and thereby to provide particle identification. ATLAS has two calorimeters, one electromagnetic (EM) and one hadronic calorimeter. The EM calorimeter measures the energy of electrons, positrons and photons, while the hadronic calorimeter measures the energy of hadrons. As mentioned in section 4.3.1, an important signal for many new physics scenarios, including supersymmetry, is large missing transverse energy in the event. Therefore, a high η coverage is particularly important for the ATLAS calorimeters. As mentioned above, 23 collisions will be produced on average in each bunch crossing (i.e. every 25 ns) at the LHC design luminosity. This will give rise to so-called 'pile-up'. To minimise the impact of pile-up on the physical performance, a fast detector response (< 50 ns) and fine granularity is required [32]. All calorimeters in ATLAS are so-called sampling calorimeters, meaning that they consists of alternating layers of active and passive material. Only energy collected in the active material is measured [33]. A sketch of the ATLAS calorimeters is shown in Figure 4.4.

Electromagnetic Calorimeter

The electromagnetic calorimeter absorbs and measures energy of electromagnetically interacting particles. It is a sampling calorimeter that uses liquid Argon (LAr) as active material and lead as absorber. The EM calorimeter

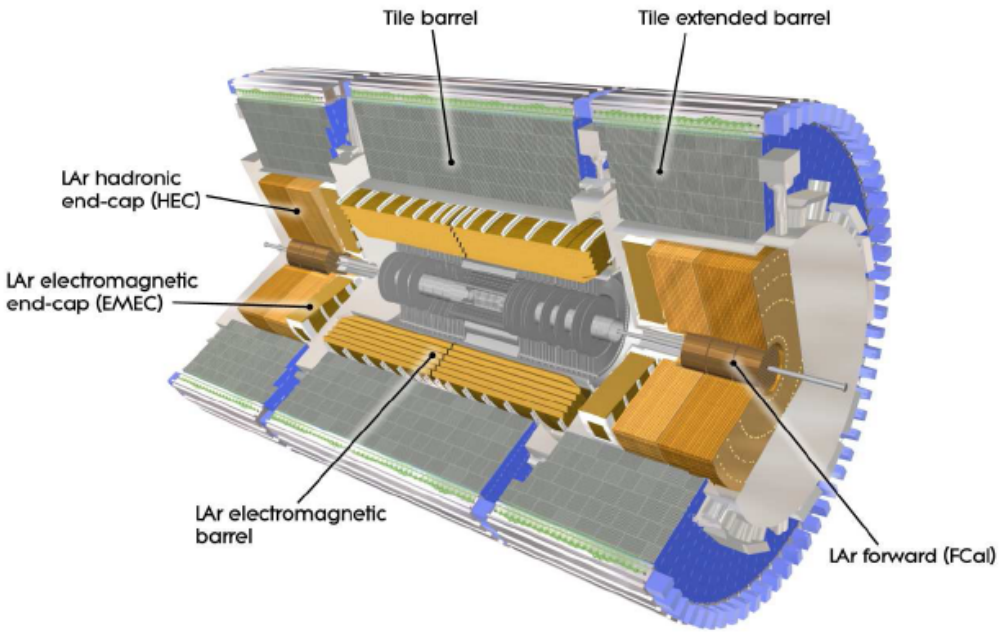

Figure 4.4: 3-D view of the ATLAS calorimetry. The figure is taken from Ref.[30]

has an accordion geometry constructed of equally thick lead absorber plates, interleaved with gaps of liquid Argon which increase with the radius. Most of the energy is absorbed in the Pb plates, and the LAr is ionized by charged particles produced in the absorption process of the primary particles. The ionization electrons are then collected as a signal. The accordion geometry provides complete ϕ symmetry without azimuthal cracks [30].

The EM calorimeter is divided into a barrel, covering the pseudorapidity range $|\eta| < 1.475$, and two end-cap components, covering $1.375 < |\eta| < 3.2$. The barrel calorimeter consists of two identical half-barrels, separated by a small gap of 4 mm at $z = 0$. Both end-caps are divided in two coaxial wheels; an outer wheel covering the region $1.375 < |\eta| < 2.5$ and an inner wheel covering the region $2.5 < |\eta| < 3.2$.

In addition to the requirements of a good η coverage and high granularity, the EM calorimeter should be capable of reconstructing electrons in the energy range spanning from 1-2 GeV up to 5 TeV, in order for new physics to be dis-

covered. An excellent energy resolution is among other requirements to the performance of the EM calorimeter. An important task for EM calorimeter for the analysis in this thesis, is an excellent tau/jet separation capability, meaning a high rejection factor of QCD jets from those originating from hadronically decaying tau leptons. This will be discussed in more detail in Chapter 6. Information from the EM calorimeter, the hadronic calorimeter and from the ID have to be combined for obtaining such a rejection factor. Since the EM calorimeter has a higher granularity than the hadronic calorimeter, the contributions from the EM calorimeter will be important to distinguish a tau-jet from a QCD-jet on the basis of the shape of the shower.

Hadronic Calorimeter

The main task of the hadronic calorimeter is reconstruction of jets and measurement of missing transverse energy in the event [32]. The hadronic calorimeter consists of three sub-systems; the tile calorimeter, the hadronic end-cap calorimeter and the forward calorimeter, all situated outside the EM calorimeter.

The tile calorimeter covers the barrel region with a centered barrel in the range $|\eta| < 1.0$ and two extended barrels covering the region $0.8 < |\eta| < 1.2$. It uses plastic scintillator tiles as active material, interleaved with steel absorber tiles. At each side, the end-cap region is divided into a hadronic end-cap calorimeter and a high density forward calorimeter, covering different regions of the η-range. The end-cap calorimeter has a coverage $|\eta| < 3.2$, whereas the forward calorimeter covers the region $3.1 < |\eta| < 4.9$ [30]. The end-cap calorimeter uses liquid Argon as active material and copper as absorber, while the forward calorimeter uses tungsten as absorber instead of copper, due to its higher radiation resistance.

4.3.5 The Muon Spectrometer

The muon spectrometer surrounds the hadronic calorimeter and it is the largest sub-system in the ATLAS detector. Its main task is to measure momenta of muons and it is based on the magnetic deflection of muons in a superconducting air-core toroid magnet. In addition, the muon spectrometer is instrumented with a fast trigger system and precision tracking chambers. The magnet configuration consists of eight separate magnets covering the

barrel region, and two additional end-cap toroids. The strength of the magnetic field ranges from 0.5 - 2 Tesla, and the bending direction of the field is in the $R-z$ plane, where R is the radial coordinate. The precision measurements of the muon tracking system are made in a direction parallel to the bending plane, where the z coordinate is measured in the barrel region, and R is measured in the transition and end-cap region. Four different chamber technologies are used in the muon spectrometer; two for precision measurement and two for trigger and pattern recognition. Figure 4.5 shows the layout of the muon spectrometer.

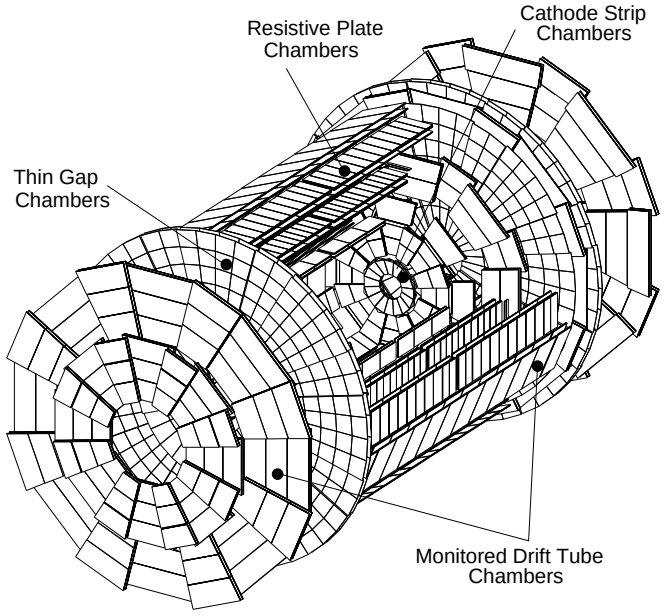

Figure 4.5: 3-D view of the muon system, indicating where the different chamber technologies are used [34].

The different detector technologies used in the precision tracking system are Monitored Drift Tubes (MDT) in the barrel region and Cathode Strip Chambers (CSC) in the end-cap region. The basic detector elements of the MDT chambers are aluminium tubes of 30 mm diameter. The tubes are filled with an Argon-based gas mixture at a pressure of 3 bar, and a wire of W-Re runs through the center of them. The W-Re wires have a diameter of 400 μm. The tubes have a total volume of 800 m^3 divided on a number of 370 000 tubes

that varies in length from 70 - 630 cm. The CSCs are multiwire proportional chambers with shorter response-time and higher granularity than the MDTs [33]. They are employed in the end-cap region, covering the pseudorapidity range $2.0 < |\eta| < 2.7$, where the flux of particles are at the highest [34].

The trigger system covers the pseudorapidity range $|\eta| < 2.7$ and it uses two different chamber technologies; resistive plate chambers (RPC's) in the barrel region and thin gap chambers (TGC's) in the end-cap regions. The trigger chamber of the muon spectrometer serve a threefold purpose; provide bunch-crossing identification, provide well-defined p_T thresholds, and measure the muon coordinate in the direction orthogonal to that determined by the precision tracking chambers [30].

4.3.6 The trigger system

In each bunch crossing, 23 protons are expected to collide in the detector. Bunches are crossing every 25 ns, giving a bunch-crossing rate of 40 MHz at the LHC design luminosity. The interaction rate will then be $\sim 10^9$ Hz. In each event approximately 1000 particles will emerge from the collision point, creating a very large track density in the detector [30]. This corresponds to an event size of ~ 1 MB. To deal with this huge amount of information, a fast and efficient trigger system is required. The data rate needs to be reduced to about 100 events per secound for permanent storage, that is a rejection factor of 10^7. The ATLAS trigger and data-acquisition (DAQ) system is based on three levels of on-line event selection. Each trigger level refines the decisions made at the previous level, and applies additional selection criteria where it is necessary. Figure 4.6 illustrates the event reduction procedure.

Level-1 Trigger

The level-1 trigger (LVL1) is a hardware based trigger that makes the initial selections based on reduced-granularity information from a subset of detectors. High transverse momentum muons are identified using only the trigger chambers of the muon spectrometer. Objects such as high p_T electrons and photons, jets, and hadronically decaying τ-leptons are searched for by the calorimeter trigger. The LVL1 for these selections are based on reduced-granularity information from all the calorimeter parts. All the detector data

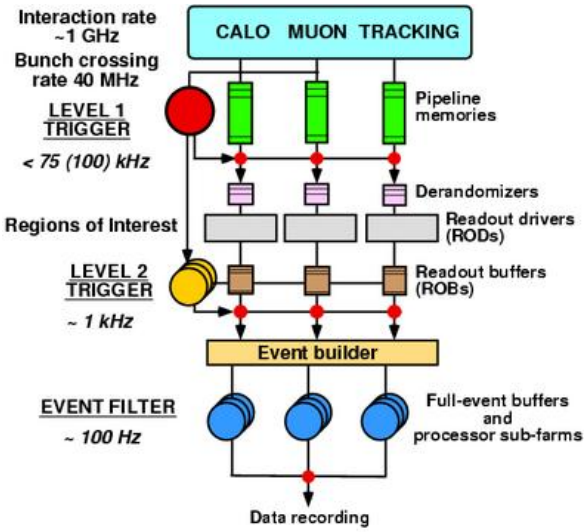

Figure 4.6: The trigger and Data Acquisition system (DAQ) for ATLAS. The primary data produced in the detector has to be rejected with a factor of 10^7 for full time storage. The LVL1 trigger reduces the amount of data from $\sim$ 40 MHz to $\sim$ 100 kHz, the LVL2 has a rejection factor of 100, and the Event Filter reduces the 1 kHz that passed the LVL2 trigger to 100 Hz.

for the event selected by the LVL1 trigger is stored in readout buffers (ROBs), until the level-2 (LVL2) trigger either rejects or accepts the event. In case of acceptance, the data will be held in the ROBs until it is successfully transferred by the DAQ system to storage associated with the third level of event selection, the event filter. The LVL1 trigger makes a so called Region of Interest (RoI), containing all the information that contributes to the selection of the event. The RoIs are then passed over to the LVL2 trigger. This includes information on the position (η- and ϕ-values), p_T of candidate objects and energy sums (missing and total transverse energy).

Level-2 Trigger

One of the rejection criteria for the LVL2 is a requirement of isolation. In the case of the muon trigger, the isolation requirement uses the calorimeter information in a region around the muon candidate, whilst for isolated electrons an additional rejection power is the requirement of matching high-p_T tracks in the ID. For the hadron/tau trigger, rejection at LVL2 is achieved using the full-granularity calorimeter information and the ID. A localized and isolated hadronic calorimeter cluster with matching p_T is required. In

the LHC environment, high p_T jets are dominant. The threshold behaviour of the LVL1 trigger is reasonably sharp in the case of jets, so a much lower rejection rate is possible for the LVL2 jet trigger. It is expected that the LVL2 will reduce the bunch amount of data from ca. 100 kHz to 1 kHz.

Event Filter

The last stage of on-line selection is performed by the event filter (EF), and it will make the final selection of physics events which will be kept for full-time storage. The EF should reduce the output rate from the LVL2 trigger by an order of magnitude, giving a final output rate of 100 Hz (or 100 MB/s). The EF will employ offline algorithms and methods adapted to the on-line environment in its decisions. The EF will first confirm the results of the LVL2 decisions and subsequently use the result of LVL2 to seed its own analysis.

4.4 Physics in ATLAS

ATLAS is constructed to identify muons, electrons, photons and jets. The different objects are reconstructed using different algorithms carefully constructed for that purpose. The algorithms collect information from the various sub-systems in which the object under consideration are expected to leave hits, and then compare it with the expected behaviour of the object one wants to reconstruct. The basic idea of how the different particle types will interact with the different layers of the ATLAS detector is shown in Figure 4.7.

4.4.1 Muons

The muons have a long lifetime, $c\tau = 658.7$ m [3], and great penetration power. Muons produced in the center of the detector will give hits in the ID and the muon spectrometer before they leave the detector. They will deposit only a fraction of their energy in the calorimeters. The reconstruction of muons is mainly based on track measurement combination, from reconstructed tracks in the ID and the muon spectrometer. For muons with $p_T > 6$ GeV, the reconstruction efficiency is $\sim 90\%$.

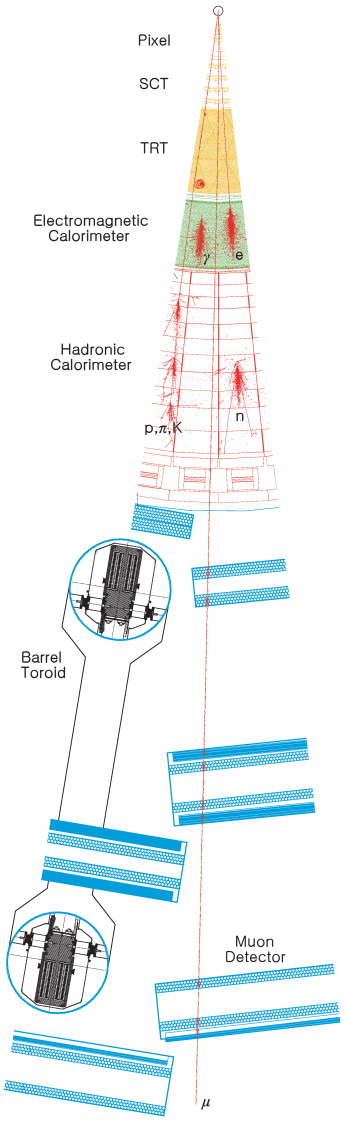

Figure 4.7: The figure indicates where the different types of particles decay and in which detector layers they leave tracks in the ATLAS detector, starting from the beam pipe interaction point at the top. Charged particles give hits in the ID, whereas neutral particles are only seen in the calorimeters where they either decay or are slowed down. The muon detector is the largest detector system in ATLAS, as the figure indicates, and its task is to track high energetic penetrating muons [35].
The ID is surrounded by a central magnet, with a field strength of 2T, which purpose is to bend charged particles, allowing their momentum to be measured. The muon detector is also provided with a magnetic field surrounding the hadronic calorimeter. The cross-section view is in the transverse xy-plane at $z = 0$. The figure is taken from Ref. [35]

4.4.2 Electrons

Electrons will be identified with combining hits from the ID and the electromagnetic calorimeter. When the electrons reach the calorimeter, a procedure of *bremsstrahlung* and *pair-production* will take place, causing the electrons to stop here. There is a sizeable probability for an electron to loose a significant fraction of its energy before leaving the ID, for instance 20% of the electrons with $p_T = 20$ GeV will loose half of their energy by the time they leave the ID barrel. Although much of the bremsstrahlung will be collected

in the EM calorimeter, the tracking in the ID may be seriously affected by this [29]. For low energetic electrons ($p_T < 15$ GeV), the best energy measurements is obtained by the ID, and for high energetic electrons by the EM calorimeter. In the environment of the LHC dominated by QCD jets, a good separation between electrons and jets are required. A good rejection is provided by the ratio between the calorimeter energy and the momentum, E/p, which should be close to one for electrons.

4.4.3 Photons

Photons will not leave hits in the ID, but will deposit all their energy in the EM calorimeter. Its reconstruction is therefor mainly based on information from the EM calorimeter. Though, due to the significant amount of material in front of the calorimeters, about 30% of all photons are converted to e^+e^- pairs in the ID. By combining pairs of oppositely charged tracks and require them to meet in a common vertex, and that the reconstructed photon point back to the beam line, conversions can be recovered with an overall efficiency $\sim 60\%$ [33].

4.4.4 Jets

As stated above, the main production in a hadron collider such as the LHC will be jets originating from QCD processes. The quarks and gluons produced in proton-proton collisions will fragment and produce colour neutral objects called jets. Charged objects will give hits in the ID and all jets will then deposit their energy in the calorimeters. There exists a number of different jet reconstruction algorithms aimed for meeting the requirements for analysis of different physics processes. They use different approaches reconstructing jets from the information obtained from the ID and the EM- and hadronic calorimeter. A description for these methods can be found in Ref. [29]. Narrow jets are also produced in hadronic tau decays. A separation between jets origin from QCD processes and these tau-jets will be discussed in Chapter 6.

4.4.5 Missing transverse energy

The transverse energy, E_T, and other transverse variables are defined in the $x-y$ plane, due to the fact that the initial momentum in the beam direction

of the colliding partons[2] is unknown, but initial momentum in the transverse plane is $\sim$ zero. Good measurements of the missing transverse energy, E_T^{miss}, is essential in the search for new physics (NP). In the case for supersymmetry, the lightest supersymmetric particle will, if electrically neutral, escape detection leaving no signals except from a pronounced amount of missing energy. Therefore, a minimization of fake E_T^{miss} produced by instrumental effects, such as badly reconstructed objects and dead cells in the calorimeters, is mandatory in order to observe NP events that are characterised by missing energy.

Readers interested in a more detailed description of the detector and/or the object identification procedure are referred to Ref. [29].

4.4.6 Some useful quantities

In the following, some quantities and variables often used in high energy physics analysis will be introduced.

A distance ΔR is defined in the pseudorapidity-azimuthal angle space as

$$\Delta R = \sqrt{\Delta\eta^2 + \Delta\phi^2}. \tag{4.2}$$

This is a quantity used to define the distance between the direction of two objects, i.e two particles in the detector. Another quantity frequently used is the transverse impact parameter, d_0. This is defined as the transverse distance of the beam axis and the point of closest approach. The transverse impact parameter is proportional to the flight distance of a particle, (which corresponds to the life time of the particle multiplied with the γ-factor).

The cross section is a quantity used to express the probability for a certain interaction to occur. As the name indicate, it is given in area, normally in the unit of barn.

[2] Protons are composite particles existing of quarks and gluons. These are refered to as partons.

4.5 Current status of the experiment

After suffering many delays, the LHC start-up is now just around the corner. The installation of the machine is now completed; what remains is the cooling of the magnets. The beam pipe will be closed in March, and if no cooling problems occur, the LHC machine will be ready in May 2008. The first collision is scheduled to take place July 28th, with a luminosity of $\mathcal{L} = 10^{30}$ cm^{-2}s^{-1}. During the summer 2008, the luminosity will increase to $\mathcal{L} = 10^{32}$ cm^{-2}s^{-1}. During the first part of 2009, the LHC will start running with a luminosity of $\mathcal{L} = 10^{33}$ cm^{-2}s^{-1}. The design luminosity of $\mathcal{L} = 10^{34}$ cm^{-2}s^{-1} will then finally be reached within 2012.

The installation of the ATLAS detector in the cavern started in the summer 2004. It is now fully installed, except from relatively small parts of the muon spectrometer (so called Muon small wheels) and parts of the LVL1 trigger system. Commissioning with cosmic rays is being carried out and the data flow chain has been tested with real-like data.

Chapter 5

Simulation and analysis tools

Monte Carlo simulated data plays an important role in high energy physics research. In order to understand the complicated physics involved in hadron collisions, and also to investigate the potential for new physics discoveries at the LHC, we depend on good and accurate simulations of the experiments. The LHC is scheduled to have its first proton-proton collision in July 2008, and the analysis of this thesis is hence performed on simulated data. When real data is available, the analysis of these can be compared with analysis of simulated data to gain an understand of the physics process behind the results. Simulated events so form the basis of for the conclusions that ultimately are to be drawn from the experiment [33].

This chapter will give an introduction to the tools used in the simulation process. Simulation of the ATLAS experiment consists of two main steps; event generation and detector simulation. There exists different methods for solving both these tasks. Some of them will be mentioned here, and the basic set-up will be described. Further, a short introduction to ROOT, the framework used for data analysis, will be given.

5.1 Event Generators

Event generators are computer programs using Monte Carlo (MC) methods in generating particles produced in particle collisions, and in the case for ATLAS, particles produced in hadron collisions. The event generator codes are used to produce hypothetical events with a probability distribution pre-

dicted by theory, i.e. the frequency at which we expect the events to appear in nature [36].

The event generators considered here are so-called *showering and hadronization* generators (SHGs). They start with a leading order hard sub-process, which is the fundamental interaction between two partons in the protons. The probability for a parton candidate, i.e. quarks and gluons, to take part in the hard sub-process is given by parton distribution functions (PDF's). These PDF's rely upon knowledge of the distribution of the momentum fraction x of the partons in the incoming hadron in the relevant kinematic range [36]. The PDF's can not be calculated perturbatively but are obtained by using experimental data.

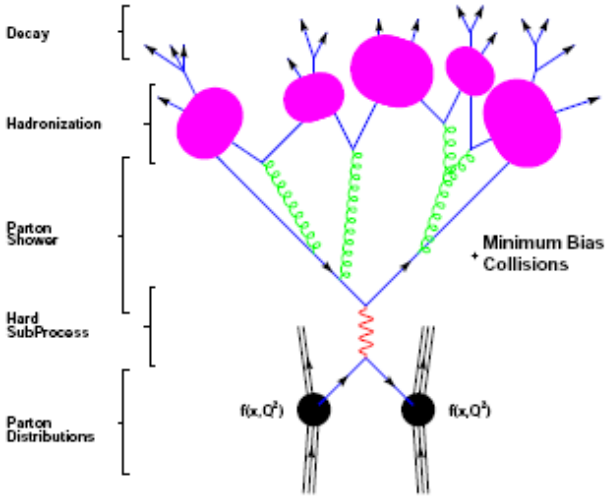

Figure 5.1: The figure shows the general structure of the final state of an event from an SHG event. The figure is taken from Ref. [36].

The hard sub-process is usually a $2 \to 2$ scattering process, e.g. $u\bar{u} \to Z^0 \to d\bar{d}$. Higher order effects are added by *evolving* the event using the parton shower, which allows partons to split into pairs of other partons. Other radiative corrections can be taken into account, although higher-order QCD corrections are highly technical.

The resulting partons are then grouped together (hadronized) into colour-singlet hadrons, and unstable particles (or short-lived resonances) are decayed further. Next, underlying structures of the event are generated. This

includes *beam remnants*, which are the coloured remains of the protons left behind when the partons participating in the hard sub-process are 'pulled out', interactions from other partons in the hadrons (multiple parton interactions), and collisions between other protons in the same bunch crossing, so-called *pile-up*. [36]. Figure 5.1 shows the general structure of the final state of an event from an SHG. The time evolution of the event goes from bottom to top.

Two frequently used SHGs are HERWIG [37] and PYTHIA [38]. They are so-called general purpose MC event generators for simulation of lepton-lepton, lepton-hadron and hadron-hadron collisions. In simulating proton-proton collisions, they follow the structure indicated in Figure 5.1. Supersymmetric events of a large range of MSSM can be generated with both of them. They use different underlying structures for solving their tasks, but this will not be lightened here. All samples used throughout this thesis are generated with PYTHIA. The samples are identified with a specific run number, identifying different processes and physics scenarios. Information about these identification numbers can be obtained from Ref [39]. CSC stands for *computing system commissioning*, and CSC samples denotes the officially produced data sets made within the third data challenge for ATLAS, DC3.

5.1.1 Tauola

There also exists specialised decay programs for decaying certain particles. Tauola is such a program, and it is used for generating tau lepton decays. The Tauola package is a library of MC programs for leptonic and semileptonic decays for the tau lepton. It provides final states with full topology including neutrinos, resonant distributions for intermediate particles and complete spin structure throughout the decay. The program is constructed in such a way that it can be easily attached to any MC program simulating the production of taus [40].

5.2 Detector Simulation

To simulate a full event in ATLAS, it is not enough to simulate the event itself. A simulation of how the detector material affects the event and how the detector responds to the event, is required. A simulation of the ATLAS detector is an ambitious task, as it is one of the largest and most complex

detectors ever designed. A simulated event in ATLAS should enable detailed physics studies to lay the basis for the first physics discoveries [41]. A schematic representation of the full simulation and analysis chain is shown in Figure 5.2, where the blue blobs corresponds to output data and the rectangles to the different processes that are to take place in a full simulation of the ATLAS experiment.

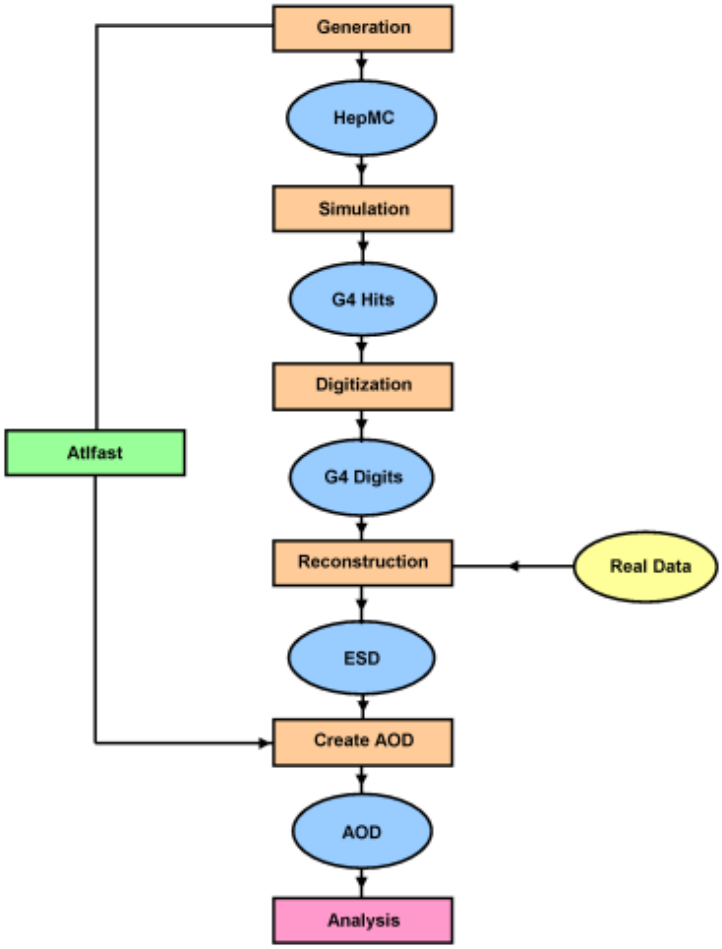

Figure 5.2: Schematic representation of the Full Chain Monte Carlo production. The figure is taken from Ref. [42].

The tool used for simulating particles interaction with matter in the ATLAS detector is GEANT4. GEANT4 simulates how outgoing particles, i.e. particles produced at generator level, interact with the detector material as they are 'transported' through the different detector layers. Thus GEANT 4 sim-

ulates hits in the tracking devices and energy deposits in the calorimeters, denoted G4 Hits in Figure 5.2.

The next step is the digitisation. From the GEANT4 hits, the detector response is simulated. The hits from the tracking devices and the energy deposits in the calorimeters are converted into detector digits, corresponding to the output from the ATLAS detector.

The final step in the simulation chain is the reconstruction of the original event. Digitised hits from the tracking system are collected to track the path of charged particles and digits in the calorimeter are collected in clusters providing information about the energy deposits. Different reconstruction packages then associate these tracks and clusters to reconstruct the momentum and charge of different particle candidates. These candidates have to fulfill certain criteria to be identified as one particular particle. This is done by different reconstruction algorithms.

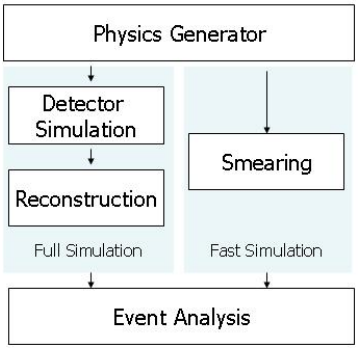

Figure 5.3: Schematic illustration of full versus fast simulation. The figure is taken from Ref. [43].

5.2.1 Fast simulation

The simulation process described above is called a full simulation. An alternative is the fast simulation package called Atlfast. Atlfast performs a fast simulation of the ATLAS detector response, in order to simulate large samples of signal and background events for physics studies [44]. As illustrated in Figure 5.3, Atlfast replaces the full detector simulation and reconstruction phases of the MC reconstruction chain. Fast simulation is performed

by smearing the MC truth information directly with resolutions measured in full simulation studies [43].

5.3 The Athena framework

Athena is a framework used in the ATLAS experiment to control simulation and analysis jobs. It controls and interfaces different components in a simulation and/or analysis chain, such as shown in Figure 5.2. As an example, Athena interfaces the output from PYTHIA with the full simulation chain. The output data after the reconstruction process described above, is so-called *event summary data* (ESD), which contains all information about the event from the detector. This includes, for instance, detailed information about the inner detector tracking and about calorimeter clusters, quantities not necessarily useful for an analysis process. From the ESD, Athena can produce *analysis object data* (AOD). The information stored in the AODs are a slimmed down version of the ESD, containing most objects relevant for physics analysis. From the AODs one can create *nTuples*, containing physical information from the event. The nTuples are stored in a format accessible by the ROOT framework. As an Athena user, one only has to specify certain job options (parameters controlling the job) for the data sample one wants to simulate. These parameters may be for instance physics processes and the alignment of the detector. The Athena framework simplifies the process of simulating events in the ATLAS experiment.

5.4 ROOT

ROOT is a data analysis framework based on an object oriented programming design. It was originally developed by René Brun and Fons Rademakers. ROOT is aimed at solving the data analysis challenges of high energy physics [45]. Previous analysis frameworks, such as PAW (used in the LEP experiment), are based on the FORTRAN 77 libraries. These non-object oriented frameworks do not scale sufficiently to satisfy the demands given by the amount of data produced by the LHC experiments. Object oriented programming gives the ability to easily modularise the analysis code, thus making many parts of the code reusable. In addition, an object oriented approach has a number of other advantages such as data encapsulation and data protection, making the code more robust. The programming language

chosen as a basis for ROOT is C++. Since C++ is based on the C programming language, the user is given the ability to do low level programming, such as direct memory manipulation. This creates several pitfalls for the programmer, e.g. memory leaks, but it also adds a lot of flexibility.

The ROOT framework consists of two main parts, ROOT libraries and CINT. CINT is a C++ interpreter, developed by Masahuaru Goto. It is an independent product, which ROOT is using for command line and script processors [45]. This means that with CINT one can run small scripts based on C++ without compiling the code. The ROOT libraries are developed to make physics analysis more about physics, and less about programming.

Chapter 6

The Tau Lepton

Chapter 7 will focus on the discovery potential of supersymmetry in the ATLAS detector in one benchmark point in the mSUGRA parameter space, where the invariant mass distribution of two tau leptons involved in the decay chain $\widetilde{\chi}_2^0 \rightarrow \widetilde{\tau}\tau \rightarrow \tau\tau\widetilde{\chi}_1^0$ has been investigated. This requires a good understanding of the behaviour and properties of the tau lepton, and especially of the identification and reconstruction of taus in the ATLAS detector.

The output from the ATLAS detector is digital signals. The extraction of particle properties from these signals is done with reconstruction algorithms. A study of simulated taus at generator level can serve as a check for the algorithms reconstructing the tau leptons in ATLAS, and also to justify the decisions they are making. There exist two reconstruction algorithms for the tau lepton implemented in the Athena framework, *tauRec* and *tau1p3p*. This chapter will show some topological properties of Monte Carlo Truth simulated tau leptons originating from different processes both within and beyond the standard model. The events have been simulated with PYTHIA and the TAUOLA package is used for decaying the taus. CSC samples have been used for the analysis. The main criteria the two tau reconstruction algorithms focus on in the tau identification procedure, will be emphasized by discussing the properties of taus in Section 6.2. The results of this section have been developed in cooperation with the editors of the Tau CSC Note, E. Richter-Was and J. Tanaka, where the results have been published, Ref. [46]. In Section 6.3, a more detailed description of the two algorithms and differences between them, will be given. At the end of this chapter, some quantities related to energy and the direction of the energy flow of tau leptons will be shown for both algorithms tauRec and tau1p3p. These quantities are important for invariant mass reconstruction.

6.1 Tau overview

The tau lepton was discovered in 1975 and the first events with signatures of a new type of particle were found at the Stanford Linear Accelerator Center (SLAC) using a magnetic detector at the colliding beam facility SPEAR [47]. The tau lepton is the third generation of charged leptons, i.e. it is unstable, with a mean life time of $\tau_0 = (2.906 \pm 0.01) \cdot 10^{-13}$ seconds [3]. Tau has a mass of $m_\tau = 1776.9 \pm 0.3$ GeV and is hence the only lepton with hadronic decay modes. Due to its short lifetime, the average flight distance for taus is $c\tau_0 = 87.11\mu$m [3]. This makes it hard to detect the tau lepton explicitly, and normally its properties are reconstructed from its decay products. Figure 6.1 show the flight distance divided by the tau γ-factor for *true* taus, i.e. taus implemented at generator level in the MC truth samples used throughout this analysis, for taus originating from the processes $Z^0 \to \tau^+\tau^-$ and $W^\pm \to \tau^\pm\nu$. This corresponds to the flight-distance of tau in its rest frame.

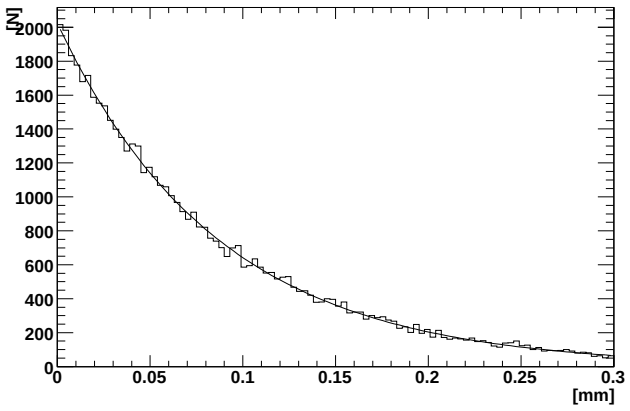

Figure 6.1: The figure shows the flight distance of tau decaying from Z^0 and $W^\pm$ bosons, divided by the tau γ-factor.

An exponential fit of the curve, as indicated in Figure 6.1, gives a slope $a = 11.46 \pm 0.06 \frac{1}{\mu\text{m}}$, where a is the inverse of the tau flight distance in its rest frame;

$$c\tau_0 = \frac{1}{a} = 87.22 \pm 0.46\mu\text{m} \tag{6.1}$$

The flight distance is in good agreement with the PDG value of the tau lifetime, $c\tau_0 = 87.11\mu$m [3].

The transverse impact parameter depends in a linear way on the angle between the charged track from the tau decay products, and the tau flight direction. This angle behaves like γ^{-1}, so the plot of the transverse impact parameter, shown in Figure 6.2, should have approximately the same form and slope as the plot presenting the flight distance, Figure 6.1. Both plots are extracted from the processes $Z \rightarrow \tau\tau$ and $W \rightarrow \tau\nu_\tau$.

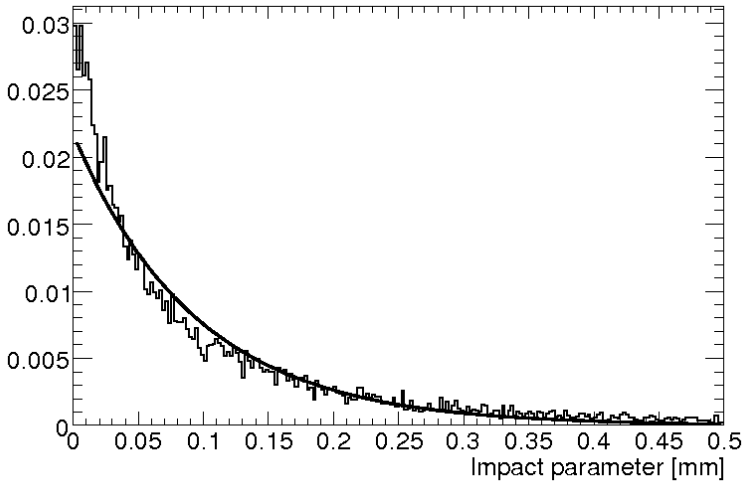

Figure 6.2: The figure shows the transverse impact parameter of taus originating from the processes $Z \rightarrow \tau\tau$ and $W \rightarrow \tau\nu_\tau$.

An exponential fit is indicated in the figure, and although the impact parameter distribution deviates slightly from this fit, the similarity the tau flight distance divided by the tau γ-factor shown in Figure 6.1 is clearly seen.

6.1.1 Tau decays

As mentioned, the short lifetime makes it hard to detect the tau lepton explicitly, and its properties are consequently calculated from its decay products. This section summarises the main decay modes for taus with an emphasis on the hadronic decay modes.

The main decay modes of tau are listed in Table 6.1. It is difficult to distinguish the leptonic decay modes of tau from primary electrons and muons in the detector, due to a small impact parameter. The two reconstruction

Decay modes	Branching fraction
$\tau \rightarrow e\nu_e\nu_\tau$	17.8 %
$\tau \rightarrow \mu\nu_\mu\nu_\tau$	17.4 %
$\tau \rightarrow h^{\pm}(nh^0)\nu_\tau$	49.5 %
$\tau \rightarrow h^{\pm}h^{\pm}h^{\pm}(nh^0)\nu_\tau$	14.6 %
$\tau \rightarrow h^{\pm}h^{\pm}h^{\pm}h^{\pm}h^{\pm}(nh^0)\nu_\tau$	0.1 %
other	0.6 %

Table 6.1: The table shows the main decay modes for tau, $h^{\pm}$ and h^0 labels charged and neutral hadrons respectively.

algorithms tauRec and tau1p3p reconstructing taus in the ATLAS detector, therefore only use the hadronic decay modes in the tau reconstruction process. Hadronically decaying taus will always decay to an odd number of charged hadrons, due to charge conservation, and in some cases an additional number of neutral hadrons. In Table 6.1, the branching fraction of taus decaying to one, three and five charged hadrons are listed. These are normally referred to as single-, three- and five-prongs respectively.

Decay products of tau are always accompanied by a tau neutrino which escapes detection. This means that the properties of tau are reconstructed from those of the visible decay products, meaning the detectable particles. The analysis of Section 6.2 aim to serve as a justification of the tau reconstruction procedure by the study of hadronically decaying taus at generator level in Monte Carlo Truth samples. In this analysis therefore only the visible hadronic decay modes for tau decaying to a single prong or three prong are used for calculating the properties of tau, as this is how taus are reconstructed in the two algorithms, TauRec and Tau1p3p, implemented in the Athena framework. Table 6.2 lists the branching fractions for the hadronic decay modes of taus.

The small fraction of five-prong decays and other decay modes with Kaons are not included in the analysis, due to the difficulties in distinguishing these modes from pion decay modes in the ATLAS detector.

The dominating processes in a hadron collider such as the LHC, are QCD processes. The main task of tau identification is to find a method to distinguish so called *tau-jets* from a multi jetty background of these QCD-processes appearing with an enormous cross section [48]. As shown in Table 6.2, in 76.4% of the hadronic decay modes, tau decays to a single prong. From these single-prong decay products, the mode $\tau \rightarrow \pi^{\pm}\nu_\tau$ contributes 23.5%, whereas

Hadronic decay modes	Branching fraction
$\tau \rightarrow h^{\pm}(nh^0)\nu_{\tau}$	76.4 %
$\tau \rightarrow \pi^{\pm}\nu_{\tau}$	17.1 %
$\tau \rightarrow \pi^{\pm}\pi^0\nu_{\tau}$	39.4 %
$\tau \rightarrow \pi^{\pm}\pi^0\pi^0\nu_{\tau}$	14.4 %
$\tau \rightarrow \pi^{\pm}\pi^0\pi^0\pi^0\nu_{\tau}$	2.1 %
$\tau \rightarrow K^{\pm}(nh^0)\nu_{\tau}$	2.4 %
other	1.2 %
$\tau \rightarrow h^{\pm}h^{\pm}h^{\pm}(nh^0)\nu_{\tau}$	22.5 %
$\tau \rightarrow \pi^{\pm}\pi^{\pm}\pi^{\pm}\nu_{\tau}$	13.9 %
$\tau \rightarrow \pi^{\pm}\pi^{\pm}\pi^{\pm}\pi^0\nu_{\tau}$	6.3 %
$\tau \rightarrow \pi^{\pm}\pi^{\pm}\pi^{\pm}\pi^0\nu_{\tau}$	0.8 %
$\tau \rightarrow \pi^{\pm}\pi^{\pm}\pi^{\pm}\pi^0\pi^0\pi^0\nu_{\tau}$	0.2 %
other	1.3 %
$\tau \rightarrow h^{\pm}h^{\pm}h^{\pm}h^{\pm}h^{\pm}(\pi^0)\nu_{\tau}$	0.2 %
other	0.9 %

Table 6.2: The table shows the hadronic decay modes of tau, $h^{\pm}$ labels charged hadrons and h^0 labels neutral hadrons.These numbers are obtained from Ref. [3]

the modes including one or more neutral pions, $\tau \rightarrow \pi^{\pm}(n\pi^0)\nu_{\tau}$, contribute the remaining 76.5 %. In the three-prong decays, the $\tau \rightarrow 3\pi^{\pm}\nu$ contributes 64.6 %, and $\tau \rightarrow (n\pi^0)3\pi^{\pm}\nu$ only 35.4%. The neutral π^0 has a lifetime of $\sim 8.4 \cdot 10^{-17}$ s, and will in 98.8 % of the cases decay to 2γ [3]. This leaves a clear and strong electromagnetic component in jets originating from taus, and this is one of the main criteria the ATLAS tau reconstruction algorithms use to distinguish tau-jets from those of QCD-processes.

6.2 Tau topology

6.2.1 Energy of the hadronic decay products of τ's

Motivations for this study of taus at generator level is to gain a good understanding on the behaviour and properties of the tau lepton, but also to

provide information justifying the reconstruction process for the tau-lepton in the ATLAS detector. This process will be introduced for the two tau reconstruction algorithms tauRec and tau1p3p towards the end of this chapter. This section will focus on some highlights of the topology of hadronically decaying tau leptons at generator level, keeping in mind the three main criteria laying the basis for the reconstruction process of these taus, namely

- Low multiplicity of tracks in the tau-jet.
- A strong electromagnetic component in tau-jets due to neutral pion decays.
- The width of the tau-jet should be narrow.

The transverse energy, or the transverse momentum of τ's is calculated from that of its visible decay products and it spans over a wide range, from below 5 GeV up to 500 GeV. Since the neutrinos escape detection this is not true information, but will serve as an estimate of the transverse energy of the tau. This means that whenever the energy or momentum of tau is mentioned, this is the quantity referred to, when not otherwise specified. Figure 6.3 shows the transverse energy spectrum of taus originating from different processes, normalised to the cross-section at which they are expected to be produced at the LHC.

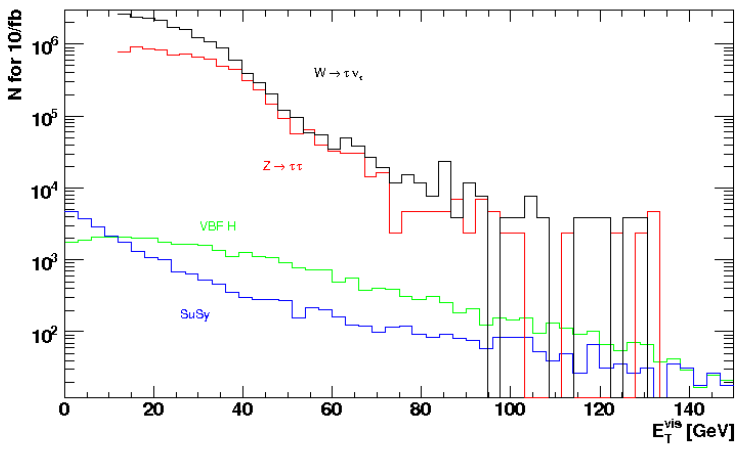

Figure 6.3: The transverse energy distribution for taus origin from different processes. This figure is taken from Ref. [46].

The number of events corresponds to an integrated luminosity of 10 fb^{-1}, equivalent to data stored after around one year of LHC running with low luminosity, $\mathcal{L} = 10^{33}$ $\text{cm}^{-2}\text{s}^{-1}$.

It is interesting to see how the energy is distributed between the charged and neutral pions. This is shown in Figure 6.4, where the l.h.s shows the fraction of the energy carried by the charged pions as a function of total visible transverse energy for the single-prong decay modes, and the r.h.s shows the same for the three-prong decays.

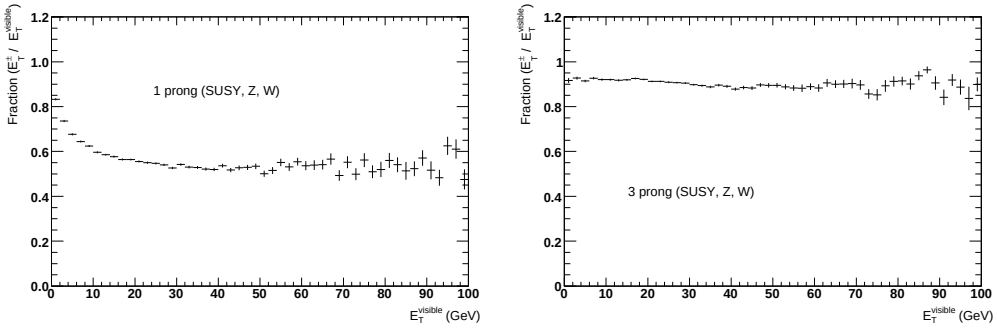

Figure 6.4: The figure shows the ratio of charged to total visible transverse energy as a function of the total visible transverse energy, the l.h.s for single-prong decays, and r.h.s for three-prong decays.

The distribution of the energy between the charged and neutral pions does not appear to vary with energy for either the single- or the three-prong decays, except for very low energies, $E_T \leq 10$ GeV, in the single-prong case. The charged pions carry $\simeq 55\%$ of the total transverse energy in the single-prong decays, whereas for the three-prong decays they carry nearly 90% of the total transverse energy. This makes the electromagnetic component in the single-prong taus much stronger, and hence a clearer signal for the reconstruction process for taus in the ATLAS detector.

Another criterion the tau-reconstruction algorithms use for identifying hadronically decaying taus in ATLAS is the narrowness of the tau-jets. This is also a good criterion for discriminating between tau-jets and jets originating from QCD-processes. To see this, the distance ΔR in $\eta - \phi$ space between the bary center of the charged pion system, weighted with energy, and the direction of the total visible decay products has been plotted against the total visible transverse energy of the system, and is shown in Figure 6.5.

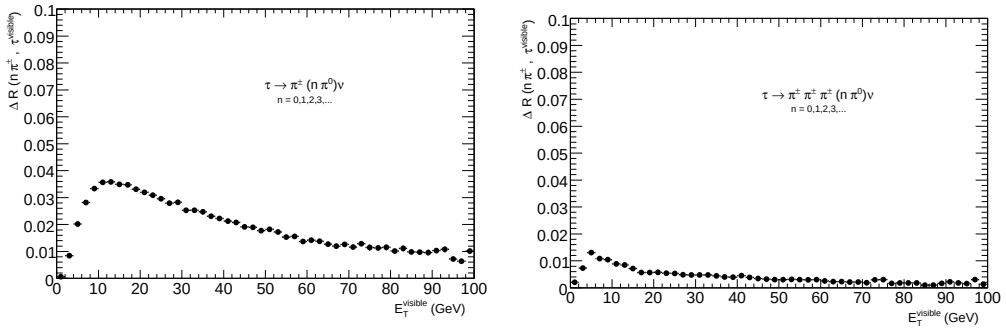

Figure 6.5: The figure shows a profile plot of the distance ΔR between the direction of the visible decay products of tau and the bary center of the charged pion system, for single-prong decays and three-prong decays respectively.

We see that the distance ΔR is decreasing with increasing energy. This so-called *shrinking cone* effect agrees with our expectations, since it illustrates that the charged hadronic decay products of taus are more collimated at higher energies. Figure 6.6 shows the same for the neutral pion system. We see the same effect, but the distance ΔR is larger here, due to the fact that the neutral pions carry a smaller fraction of the total transverse energy than the charged pions, as was illustrated in Figure 6.4. The difference is much smaller for the single-prong case, where the neutral pions carry 45% of the total energy. In the three-prong case the neutral pions carry in average only 10% of the total transverse energy.

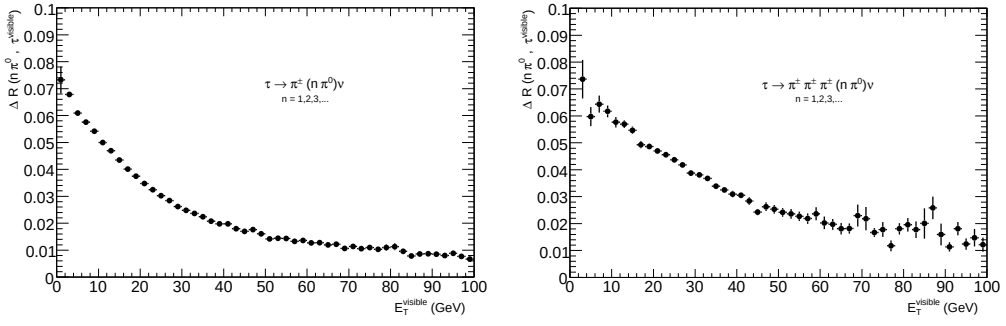

Figure 6.6: The figure shows a profile plot of the distance ΔR between the direction of the visible decay products of tau and the bary center of the neutral pion system, for single-prong decays to the left and for three-prong to the right.

6.2.2 Polarization and spin correlations

The tau lepton will carry information about the polarization of its mother particle. In the case of pair production it will also carry some information on the spin correlations between the two taus[46]. The fact that tau has hadronic decay modes, allows for an efficient measurement of its polarization. This property was exploited at LEP to make a precision measurement of $\sin^2\theta_W$ by studying the tau polarization P_τ, in the process $e^-e^+ \to Z \to \tau^-\tau^+$. The polarization for this process is given by

$$P_\tau \equiv \frac{\sigma(\tau_R) - \sigma(\tau_L)}{\sigma(\tau_R) + \sigma(\tau_L)} \simeq -2(1 - 4\sin^2\theta_W) \tag{6.2}$$

where $\sigma(\tau_{R,L})$ are the cross sections for producing τ^- with right- and left-handed helicity states respectively, and θ_W is Weinberg angle [49]. In the process where tau decays to an electron or a muon, two neutrinos are involved ($\tau \to e\nu_\tau\bar{\nu}_e$). Since the neutrinos escape detection, the electron helicity distribution in this decay mode is not very sensitive to the helicity state of the tau. In the hadronic decay modes however, only one neutrino is present, resulting in a much better determination of P_τ.

As an example, consider taus decaying from the W boson, which has spin = 1, in the case where the decay $W^- \to \tau^-\bar{\nu}_\tau$ takes place in the W rest fame. This is illustrated on the l.h.s of Figure 6.7. Since anti-neutrinos only have a right-handed helicity state (spin along its direction of propagation), the tau-lepton in this case has to be left-handed for the spin to be conserved. Further, we consider the simplest case where the now left-handed τ^- decays as $\tau^- \to \pi^-\nu$, in the tau rest frame, illustrated on the r.h.s of Figure 6.7. The π has spin = 0.

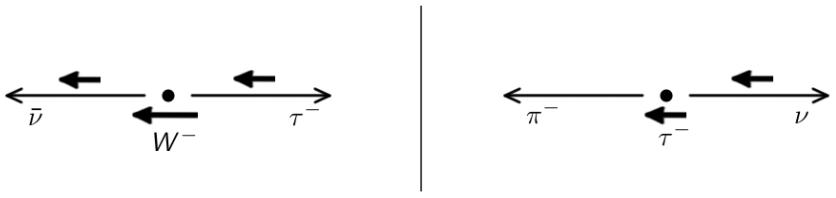

Figure 6.7: The figure shows the helicity states of particles in the decays $W \to \tau\nu$, on the l.h.s., and $\tau \to \pi\nu$, on the r.h.s., in the rest frame of W and τ respectively. The bold arrow refers to the spin of the particles.

This decay is only allowed if the neutrino involved is left-handed. This implies that the neutrino, since it has spin along the spin of the tau, flies in the direction of the tau momentum in the laboratory frame. This again means that the momentum of the π in the laboratory frame is sensitive to the helicity state of the neutrino and hence the helicity state of the tau. This is a drastical simplification of the situation, but can serve as a motivation factor for introducing a quantity R, where

$$R = \frac{p_{\pi^{\pm}}}{p_{\tau-jet}} \tag{6.3}$$

is sensitive to the spin of the particle from which tau decays. Figure 6.8 shows the polarisation of single-prong decaying taus origin from different processes.

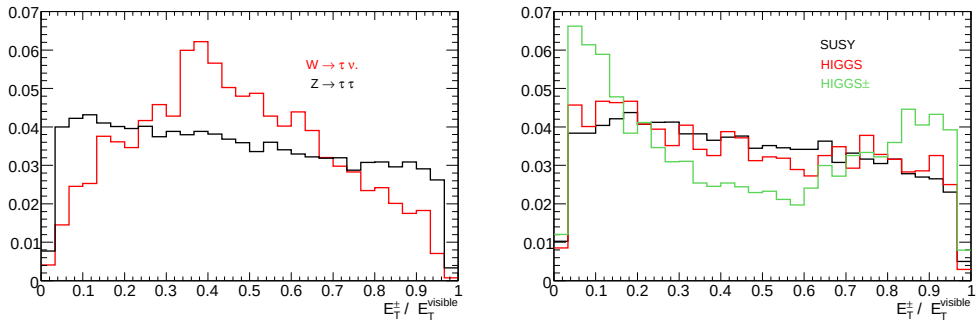

Figure 6.8: The plot shows the ratio of charged to total visible energy of taus from different processes, decaying into a single prong mode. The left-hand side shows the polarization of taus (P_τ) decaying from the vector bosons W and Z, while the right-hand side shows P_τ decaying from charged and neutral Higgs bosons, and from SUSY cascades.

We see polarisation effects from taus decaying from W bosons and from charged Higgs bosons. The charged Higgs bosons have spin zero, thus taus originating from this process have opposite polarisation than taus decaying from the W bosons. For taus decaying from Z^0 and neutral Higgs bosons, this effect is not seen, nor for the $SU(1)$ SUSY sample used in this analysis. Thus the polarisation information could provide information about the process from which the taus originate.

6.2.3 The width of the tau-jet

One of the criteria used for distinguishing tau-jets from jets originating from QCD processes is the requirement of narrowness of the tau-jet. Taus with higher energy lead to more collimated jets, as its decay products tends to travel in the same direction as high energetic taus. In fact, the angular size of the cone in which the tracks of the tau decay products are collected for a reconstruction process, is expected to be in the order of m_τ/E_τ, and hence ΔR is decreasing with increasing energy. This was shown in Figure 6.5 and (Figure 6.6) where the distance ΔR between the bary center of the charged (and neutral) pion system and the total visible energy were shown as a function of the total transverse energy. The probability distribution of this distance ΔR in $\eta - \phi$ space between the direction of the visible decay products of the τ lepton and the bary-center of the charged π system for single and three prong decays are shown in figure 6.9. The distribution of the size of the cone is shown for different energy ranges.

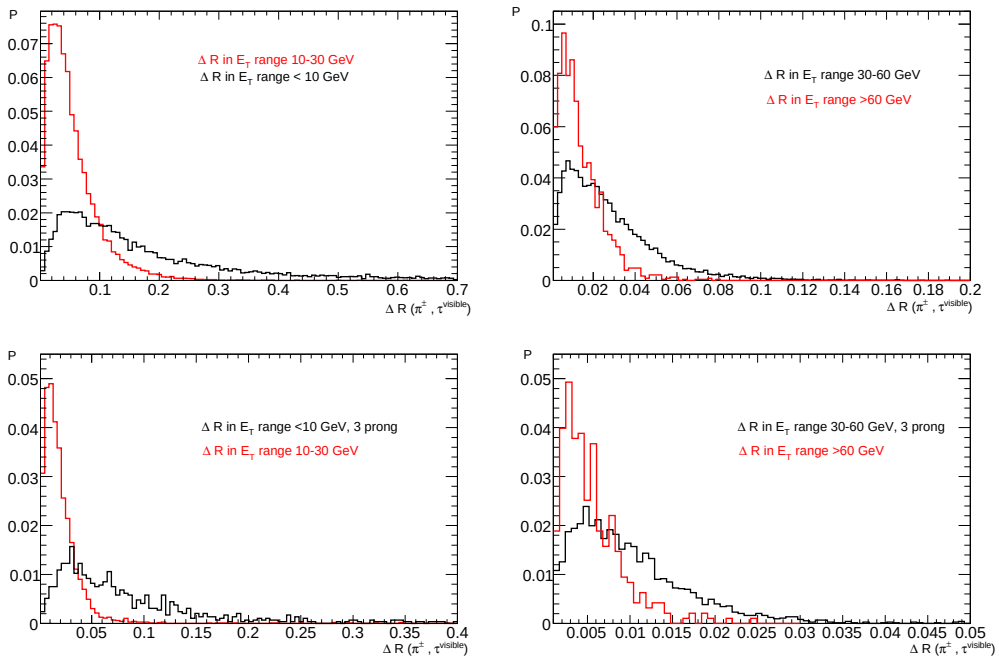

Figure 6.9: The figure shows ΔR in different energy ranges, for single-prong decays (top) and three-prong decays (bottom). Note that the scale is different for all plots.

One can see that it is sufficient to collect energy of hadronic decaying taus in a cone $\Delta R \leq 0.4$, even in the low energy regions.

6.3 Tau identification and reconstruction

In principle, tau-leptons are considered as "long-lived" particles at collider energies, meaning that their decay vertex can be measured by vertexing detector [50]. This, though, would require an excellent accuracy of detector alignment and is initially not the case. There exist two different reconstruction algorithms for tau leptons within the ATHENA framework, tauRec and tau1p3p, both reconstructing taus from its hadronic decay products. Their main task is to find a good method on discriminating tau-jets from QCD-jets. The criteria for a jet to be originating from a tau decay that was listed in Section 6.2 need to be quantified for the reconstruction process. Some of the variables used in tau identification for both reconstruction algorithms are listed in the following. The definitions are taken from Refs. [29], [48],[51],[52], and readers interested in a more detailed description are referred to these. The specific values for these variables for tauRec and tau1p3p are given in Section 6.3.1 and 6.3.2 respectively.

- **Electromagnetic radius.** As emphasized in the previous discussion, tau-jets have a strong electromagnetic component. This means that a significant fraction of the energy of the tau-jet will be deposited in the EM calorimeter. The EM-radius measures the radius of the energy deposited in the EM calorimeter cells around the seed, and it is defined as

$$R_{EM} = \frac{(\sum \Delta R \cdot E_T^{cell})}{(\sum E_T^{cell})}. \tag{6.4}$$

  The quantity ΔR is here defined as the distance in $\eta - \phi$ space between the EM calorimeter cells and the seed.

- **Isolation in the calorimeter.** To measure how well collimated the tau-jets are, and also how well isolated they are from QCD jets, a quantity referred to as *isolation fraction* is introduced. It defines a region around the barycenter of the cluster in the hadronic calorimeter, and is given as

$$\Delta E_T^{12} = \frac{(\sum E_T^{cell}) \text{ in region 1}}{(\sum E_T^{cell}) \text{ in region 2}}. \tag{6.5}$$

Both tauRec and tau1p3p use the same ring region $0.1 < \Delta R < 0.2$ for region 1, but have different values defining region 2.

- **Number of hits in the η-strip layer.** The η-strip layer is the first layer in the EM calorimeter. The number of hits here, within some cone around the cluster can be used as a criteria to separate against QCD-jets. The size of the cone varies for the different algorithms.

- **The width of the energy deposition in strips.** The $(\textit{Strip Width})^2$ is calculated as the variance in the η-coordinate, weighted by the transverse energy deposition in a given strip. The deposited energy is calculated for different cone sizes for the two algorithms.

Both algorithms separate the tau candidates in single- and three-prong taus. In the following, a short description of tauRec and tau1p3p will be given.

6.3.1 TauRec

TauRec is a calorimeter-based algorithm, using clusters in the hadronic calorimeter to qualify τ candidates. Only clusters with $E_T > 15$ GeV are used. When the tau candidate is initialised, or seeded, the algorithm collects cell energies and tracks in different cone sizes around the initial seed. The cone sizes for the variables listed above are

- The EM radius is measured in a cone $\Delta R < 0.4$ around the seed.
- Region 2 in the isolation fraction is defined by $\Delta R < 0.4$.
- Number of strips associated with the track are collected in a cone $\Delta R < 0.4$
- $(\textit{Strip Width})^2$: The transverse energy deposited in a cone $\Delta R < 0.4$

In addition to these, tauRec uses some additional variables;

- **Lifetime signed impact parameter**. The transverse impact parameter, d_0, is here defined as the smallest distance from the track to the beam axis with a sign depending on the direction of the track in the $x-y$ plane. From this information, together with the jet axis, a quantity commonly referred to as "lifetime signed impact parameter" can be constructed. It is defined as

$$\frac{d_0}{\sigma_{d_0}} \cdot sign(\sin(\phi_{cl} - \phi_{tr}), \tag{6.6}$$

  where σ_{d_0} denotes the error of the impact parameter, ϕ_{cl} and ϕ_{tr} are the coordinates in the calorimeter for the cluster and at the point of closest approach for the track. The lifetime signed impact parameter is constructed in a way to have opposite sign if the decay happens in the flight direction [51].

- $E_T^{\mathbf{rec}}/p_T^{\mathbf{leading\ track}}$: Reconstructed transverse energy divided by the transverse momentum of the leading track.

Based on this information, tauRec calculates a likelihood for each tau candidate.

6.3.2 Tau1p3p

Tau1p3p is a track-based algorithm. It starts with identifying and qualifying a leading hadronic track (see below) and creates tau candidates, single-prong and three-prong separately. The algorithm then defines the position of a seed in $\eta - \phi$ space and the energy scale of the track by checking the charge consistency for three-prong candidates [48]. If the candidate is accepted, the energy and other observable information from the hadronic calorimeter will be calculated.

For a track to be defined as a leading one, its transverse momentum must be over a certain threshold and it has to pass some criteria for a good quality reconstruction. This means requiring a minimal number of hits in the silicon and straw detectors, a threshold on the value of the impact parameter as well as a threshold on the value of the χ^2 of the fit for the trajectory reconstruction [46]. To be specific, $d_0 < 1$ mm, number of TRT hits > 9, number of hits in the SCT and the pixel detector together must exceed 8, and $\chi^2 < 1.7$ [52]. Tau1p3p uses PDE-RS (probability density estimation based on range search)

instead of the likelihood method to discriminate taus from background. It uses the values from the variables listed above, which in the case for tau1p3p algorithm are selected in following cones;

- The EM radius is measured in a cone $\Delta R < 0.2$ around the seed.
- Region 2 in the isolation fraction is defined by $\Delta R < 0.2$.
- Number of strips associated with the track are collected in a cone $\Delta R < 0.2$
- $(\textit{Strip Width})^2$,The transverse energy deposited in a cone $\Delta R < 0.2$.

and in addition two other variables defined as

- $E_T^{\textbf{rec had}}/p_T^{\textbf{leading track}}$: Reconstructed transverse energy from the hadronic cells, divided by the transverse momentum of the leading track.
- $E_T^{\textbf{other EM}} + E_T^{\textbf{other had}} / E_T^{\textbf{calo}}$. The transverse energy in the EM and hadronic calorimeter in a cone $0.2 < \Delta R < 0.4$ divided by the total $\sum E_T^{\text{cell}}$ in a cone $\Delta R < 0.4$ [52].

The tau1p3p algorithm manages to reconstruct taus in the low p_T-region with much higher efficiency than the tauRec algorithm. The default cut on the transverse momentum of taus is $p_T > 9$ GeV.

6.3.3 Comparing the two algorithms

In this section we will compare some quantities reconstructed with the two algorithms tauRec and tau1p3p. Both algorithms distinguish between single- and three-prong taus, and we have chosen only to consider the single-prong taus in this section since the analysis of Chapter 7 will focus on these cases. Taus originating from two different processes, $t \to Wb \to b\tau\nu$ and $\widetilde{\chi}_2^0 \to \tau\widetilde{\tau} \to \tau\tau\widetilde{\chi}_1^0$, will be used. The samples for these are specified in Chapter 7, where the first is a background process and the latter a signal process for the analysis of the next chapter. The processes will therefore be referred to as background and signal processes respectively.

Comparing variables calculated for single-prong taus

A good reconstruction of the transverse momentum distribution of taus is a necessity. As stated above, both algorithms operate with a default cut on the reconstruction of this variable. The tauRec algorithm only reconstructs taus with $p_T > 15$ GeV, whereas tau1p3p reconstructs taus with $p_T > 9$ GeV. Figure 6.10 shows the reconstructed transverse momentum distribution for taus originating from the background process, reconstructed with tau1p3p to the left and tauRec to the right. The cuts are clearly seen. The black line in both plots corresponds to the p_T of taus at generator level that are matched with the ones at reconstruction level. An object match algorithm matches the truth taus with reconstructed taus by taking the coordinates of reconstructed objects in $\eta - \phi$ space and checks for corresponding particles in truth data within a cone $\Delta R \leq 0.1$. We see that both algorithms perform well on reconstructing the transverse momentum.

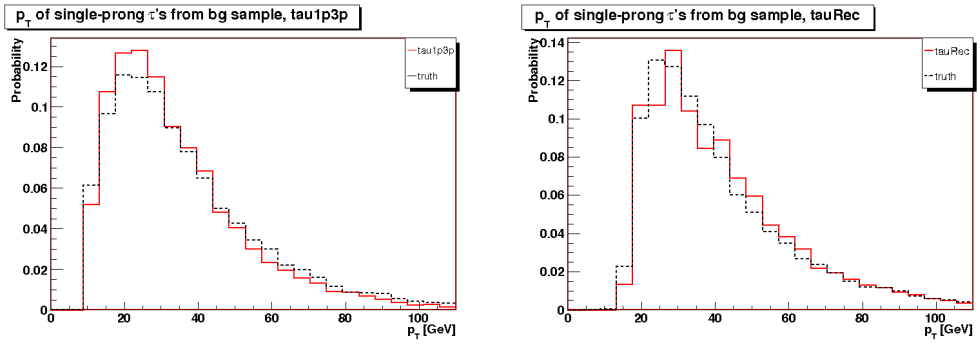

Figure 6.10: The plots show the reconstructed transverse energy distribution for taus from the background process, reconstructed with tau1p3p to the left and tauRec to the right. The black line shows the E_T distribution for taus at generator level that are matched with the reconstructed taus.

Figure 6.11 shows the reconstructed p_T distribution for taus originating from the signal process. This process produces more taus with low p_T than the background process.

Partly due to the lower cut on the p_T in the tau1p3p algorithm, more taus in the low energetic region, $p_T < 20$ GeV, are reconstructed with tau1p3p.

We can also check how good the p_T reconstruction is compared to the p_T of matched taus at generator level, by plotting ΔE_T, where $\Delta E_T = E_T^{truth} - E_T^{reco}$. This is shown in Figure 6.12. For a perfect reconstruction, this quantity should be zero. Thus, the mean value of ΔE_T should be close to zero,

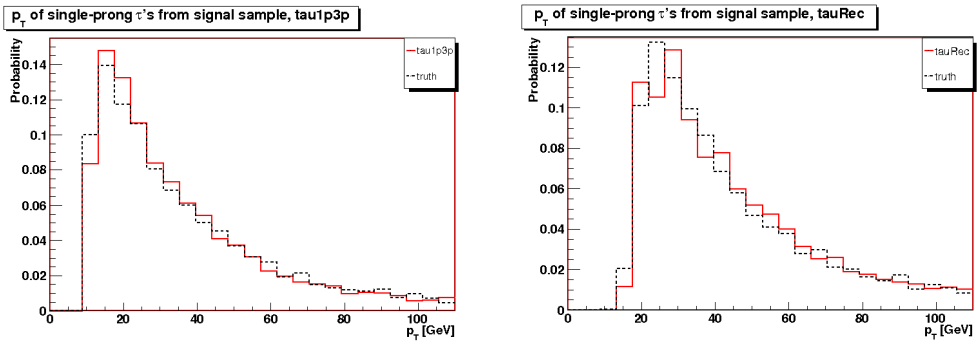

Figure 6.11: These plots shows the same as the ones above, but for taus originating from the signal process.

and the width of the distribution can serve as an estimate for how good the reconstruction is.

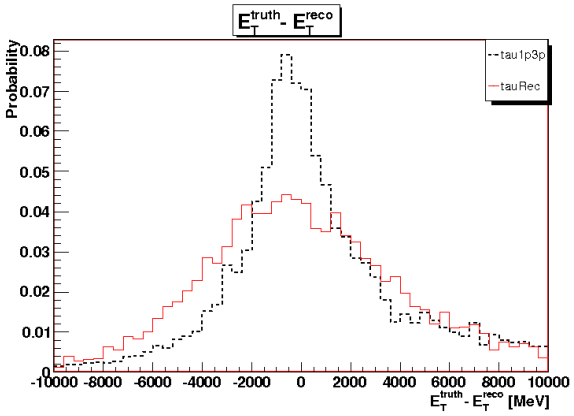

Figure 6.12: The plot shows the difference between the transverse energy for taus at generator level and reconstructed values taus for the two different algorithms. E_T of taus reconstructed with tau1p3p corresponds to the black line, whereas the red line shows the E_T reconstructed with tauRec.

The conclusion would be that the tau1p3p algorithm performs best on reconstructing the transverse energy of taus, in the case of single-prong decaying taus. However, it does not tell us how many taus are reconstructed in the first place, only how well the E_T reconstruction is compared to the E_T of matched taus at generator level.

The difference in the direction of the energy flow between the reconstructed and true taus can be shown in a similar way, by plotting the variables $\Delta\eta$

and $\Delta\phi$. These variables are calculated in the same way as ΔE_T, and the plots are shown in Figure 6.13. The l.h.s shows the $\Delta\eta$ distribution and the r.h.s the $\Delta\phi$ distribution. The values calculated with the TauRec algorithm are shown in red and for tau1p3p in black.

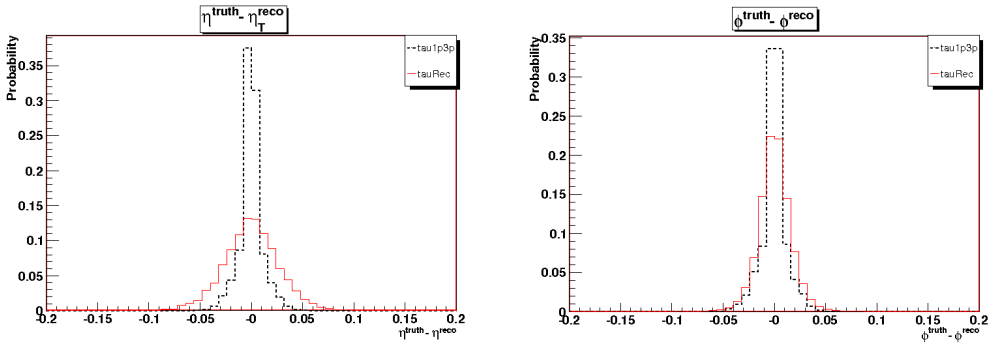

Figure 6.13: These plots show the difference in true and reconstructed values for η and ϕ respectively. The black line shows the tau1p3p reconstruction and the red line the tauRec reconstruction.

Again these variables should be zero for an ideal reconstruction. The conclusion is that the tau1p3p algorithm performs best in reconstructing the direction of the energy flow, in the case for single-prong taus.

A profile plot shows the average of the quantity on the y-axis for each value of the quantity on the x-axis. Figure 6.14 and Figure 6.15 shows a profile plot of ΔR, where ΔR is defined as

$$\Delta R = \sqrt{(\eta^{truth} - \eta^{reco})^2 + (\phi^{truth} - \phi^{reco})^2}, \tag{6.7}$$

as a function of transverse momentum for true taus. For a good reconstruction, this quantity should be as close to zero as possible. The red markers corresponds to tauRec and the black markers to tau1p3p. For both the signal sample, shown in Figure 6.14, and the background sample shown in Figure 6.15, tau1p3p performs best and has less uncertainty than tauRec.

This is a very limited comparison of the two algorithms. Only a few variables has been compared, and the main intention has been to give an impression of how they perform. However, in the low energy range, tau1p3p seems to give the best reconstruction of taus.

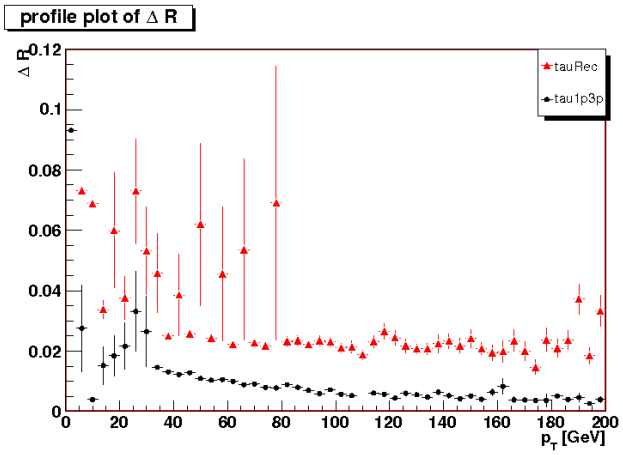

Figure 6.14: The figure shows a profile plot of ΔR as a function of the transverse energy of taus from the signal sample at generator level, where ΔR is defined in Eq. 6.7. The red markers show the values for ΔR for taus reconstructed with tauRec and the black markers for taus reconstructed with tau1p3p.

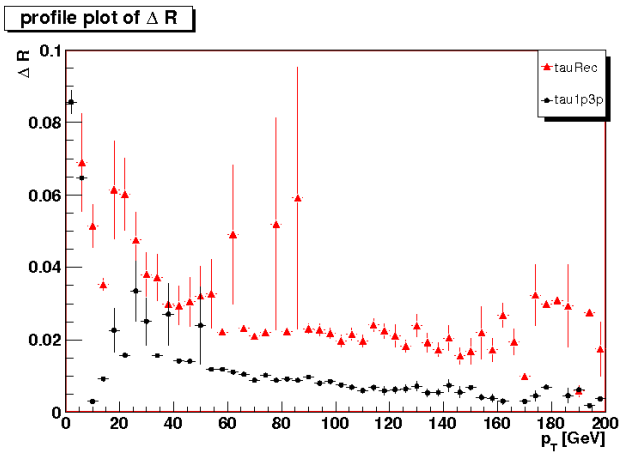

Figure 6.15: The Figure shows a profile plot of ΔR as a function of the transverse energy of taus from the background at generator level, where ΔR is defined in Eq. 6.7. The red markers show the values for ΔR for taus reconstructed with tauRec and the black markers for taus reconstructed with tau1p3p.

Chapter 7

Search for SUSY signals in the mSUGRA coannihilation region

This chapter presents an evaluation of the ATLAS potential to discover supersymmetry in the mSUGRA coannihilation region. This is the first full simulation based analysis of the coannihilation region where the fully simulated standard model background is taken into account. As a result, the study of the background is statistically limited, as there were no resources to fully simulate a substantial amount of background events. In future ATLAS analysis this problem may be solved by combining full and fast simulation of background events. This however, requires very accurate tuning of the fast simulation. There was no time for such tuning in the scope of this work. With the available background, an inclusive and efficient study of background rejection has been performed, where background from $t\bar{t}$ processes were the most challenging SM processes to separate from the desired signal. Subsequently we have made a simple fit to the invariant mass distribution in the similar way as presented in [52], but with subtracting the same-sign tau pair distributions, in order to remove background. The official ATLAS simulation data production, CSC samples, was used. This resulted in the transverse momentum cut-off for reconstructed taus, $p_T > 9$ GeV, and significantly lower efficiency for the signal compared to [52]. The analysis performed in this work corresponds to ca 30 fb^{-1} of collected data. This is equivalent to three years of running with low luminosity, 10^{33} cm^{-2}s^{-1}. The signal statistic surviving after background rejection is quite limited, even if a sensitivity ($S/\sqrt{B+S}$) of 14 were achieved. This allowed only for a very simplified analysis of the kinematic properties of the signal. Lowering the p_T threshold of the tau reconstruction algorithm should allow to increase signal

statistic without compromising sensitivity. Due to time limitation this was beyond the scope of this work.

7.1 Introduction

In Chapter 3, the symmetry called R-parity was introduced, and it was emphasized that conservation of R-parity causes the lightest supersymmetric particle to be stable. In addition, it maintains sparticles to be produced in pairs, allowing studies of supersymmetric decay chains in which the LSP is an end product. If the LSP is electrically neutral, it is a good candidate for dark matter. In this case it will escape detection and leave a signature in form of missing energy in the event. This means that the standard method of reconstructing particles from the invariant mass of their decay products, looking for resonance peaks [53], is not available. The frequently used alternative is to measure end-points of the invariant mass distributions; the position of this end-point contains information about the sparticle masses involved in the decay chain. This method will be discussed in Section 7.4.

In this analysis we have considered the supersymmetric decay chain $\widetilde{q} \rightarrow \widetilde{\chi}_2^0 q \rightarrow \widetilde{\tau}\tau q \rightarrow \tau\tau q\widetilde{\chi}_1^0$, which leads to two opposite sign taus appearing in the detector together with jets and missing transverse energy due to the escaping neutralino. The invariant mass distribution of opposite sign tau pairs has been investigated and the method of end-point measurements has been applied. The study is restricted to consider one benchmark point in the mSUGRA model in a narrow region in parameter space allowed by WMAP results, known as the coannihilation region.

7.2 The mSUGRA model and the coannihilation region

If the idea of supersymmetry is correct, it can provide some elegant solutions to problems that can not be solved with the established theory of particle physics. As was discussed in Chapter 3, SUSY allows for a cancellation of the quadratic Higgs divergence, and incorporation of SUSY to the theory may lead to a unification of the standard model couplings at the energy scale characteristic for grand unified theories (GUT). In addition, SUSY provides a natural candidate for dark matter, as discussed above. Since sparticles have

not yet been observed in experiments, SUSY must be a broken symmetry if it is realised in nature. Supersymmetry breaking and possible mechanisms for mediating SUSY breaking, were mentioned in Chapter 3. One theory suggest that gravity mediates the SUSY breaking, and within the framework of the MSSM, these are known as mSUGRA models. The MSSM sparticle mass sector introduces 105 new parameters to the theory. In mSUGRA, these are reduced to 4 free parameters and a sign by the introduction of some boundary conditions at the GUT scale. The mSUGRA parameters were listed in Section 3.3.1, but are for convenience repeated here;

1. A common soft breaking mass for the gauginos at M_{GUT}; $m_{1/2}$,
2. a common soft breaking mass for the scalars (sfermions and Higgs bosons) at M_{GUT}; m_0,
3. a common value for all trilinear couplings in the Lagrangian; A_0,
4. $\tan\beta$, being the ratio between the two Higgs doublet VEVs, given as $\tan\beta = \frac{\langle H_d \rangle}{\langle H_u \rangle}$,
5. and the sign of the Higgs mass parameter μ.

In addition, there exists experimental constraints which make the mSUGRA parameter space even more manageable. These will not be discussed in detail, but should be mentioned. The constraints include the lower bound on the Higgs mass, $m_H > 114$ GeV, from LEP experiments, the correction of the muon magnetic moment, $g_\mu - 2$, the branching fraction for the process $b \to s\gamma$, and WMAP measurements of the dark matter relic density. These constraints exclude most of the mSUGRA parameter space, leaving four main distinct regions. One of these regions that has so far not been ruled out by experimental constraints is the coannihilation region, and it is the largest allowed region in parameter space within mSUGRA [54]. We have considered one benchmark point in this region for this analysis, defined by the following values of the mSUGRA parameters:

$$m_0 = 70 \text{ GeV}, \quad m_{1/2} = 350 \text{ GeV}, \quad A_0 = 0, \quad \tan(\beta) = 10, \quad \mu > 0. \quad (7.1)$$

Figure 7.1 shows the mSUGRA parameter space in the $m_0 - m_{1/2}$ plane with the other parameters set as above, where the coannihilation region is indicated with an arrow.

Readers who are interested in a general discussion about choices of mSUGRA parameters are referred to Ref. [23].

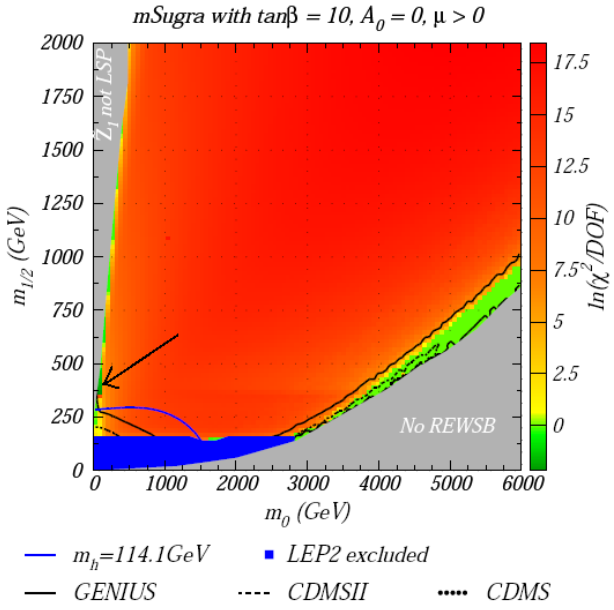

Figure 7.1: The mSUGRA parameter space in the $m_0 - m_{1/2}$ plane where $A_0 = 0$, $\tan(\beta) = 10$ and sgn $\mu > 0$. The figure is taken from Ref. [55].

7.2.1 Coannihilation process

Most SUSY models predict too much DM compared with WMAP measurements of the current relic density of DM. To be consistent with these measurements, the presence of a mechanism to suppress the relic density is required. One such mechanism is a coannihilation process. This situation occurs when another particle lies near in mass to the DM-particle. The relic abundance of the LSP is determined not only by its annihilation cross section, but also by the annihilation of the heavier particle which will later decay into the LSP [56]. If the process sketched in Figure 7.2 were to take place in the early universe before the temperature T falls below the freeze-out temperature, T_f, when LSP annihilation freeze out, it would reduce the relic density. In the coannihilation region in the mSUGRA parameter space, the mass difference between the stau and the lightest neutralino is restricted to be $\Delta m = m_{\tilde{\tau}} - m_{\tilde{\chi}_1^0} \simeq 5 - 15$ GeV, to allow this coannihilation process in the early universe.

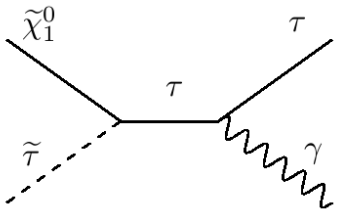

Figure 7.2: The figure shows a Feynman diagram of the coannihilation process of $\widetilde{\tau}$ and $\widetilde{\chi}_1^0$ that may have occurred in the early universe if the two particles are almost degenerate in mass.

7.3 Signal process

The signal process for this analysis is the supersymmetric cascade decay possibly starting with a gluino that decays as $\widetilde{g} \rightarrow \widetilde{q}q$, where the $\widetilde{q}$ decays as indicated in Figure 7.3. The $\widetilde{\tau}$ in this decay chain is assumed to be the lightest $\widetilde{\tau}_1$.

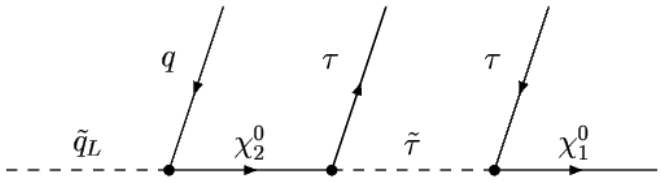

Figure 7.3: The figure illustrates the cascade decay chain producing a pair of τ-leptons of opposite charge.

Typical signatures for this process are missing transverse energy due to the escaping neutralino, $\widetilde{\chi}_1^0$, two tau-leptons with opposite charge, and at least two highly energetic jets. Since the mass difference between the stau and the lightest neutralino is small in the benchmark point under consideration, the tau decaying from $\widetilde{\tau}$ should be soft, i.e. with transverse momentum $p_\tau \lesssim 30$ GeV, if the system is not too boosted. This feature has been exploited in the attempt of separating standard model background from the SUSY signal process, and is discussed in Section 7.7.2.

7.4 Invariant mass

A stable and electrically neutral LSP, such as the $\widetilde{\chi}_1^0$, will traverse ATLAS, leaving no tracks or energy deposit in the detector. Since the $\widetilde{\chi}_1^0$ is very massive, it will, however, leave a signature in form of a large amount of missing energy in the event. This complicates the process on gaining information about the sparticle masses, since it prevents invariant mass distributions of decay products to peak at the mass of their mother particle, resulting in a distribution that is effectively smeared within some kinematic limits. The end-point of an invariant mass distribution will yield information about the unknown masses, as will be discussed in the following.

The extraction of masses of supersymmetric particles in a decay chain requires as many kinematic end-points as unknown masses. In the decay chain $\widetilde{\chi}_2^0 \to \widetilde{\tau}\tau \to \tau\tau\widetilde{\chi}_1^0$ there are three unknown masses; $m_{\widetilde{\chi}_2^0}$, $m_{\widetilde{\tau}}$ and $m_{\widetilde{\chi}_1^0}$. However, only two particle momenta are measured; those of the two taus, from which only one mass distribution can be constructed [23]. This means that the system is underdetermined for extracting the three masses; only a relation between them can be given.

Obtaining an expression for this relation is straightforward. By considering the decay in the rest frame of $m_{\widetilde{\chi}_2^0}$ and for simplicity treat the τ's as massless[1], we have from energy and momentum conservation;

$$\begin{aligned} m_{\widetilde{\chi}_2^0} &= E_{\widetilde{\tau}} + E_{\tau} \\ \mathbf{p}_{\widetilde{\tau}} &= -\mathbf{p}_{\tau} \end{aligned} \tag{7.2}$$

The relativistic energy-momentum relation then gives

$$\begin{aligned} p_{\widetilde{\tau}}^2 &= E_{\widetilde{\tau}}^2 - m_{\widetilde{\tau}}^2 \\ &= (m_{\widetilde{\chi}_2^0} - E_{\tau})^2 - m_{\widetilde{\tau}}^2 \\ &= (m_{\widetilde{\chi}_2^0} - p_{\tau})^2 - m_{\widetilde{\tau}}^2 \\ 2m_{\widetilde{\chi}_2^0} p_{\tau} &= (m_{\widetilde{\chi}_2^0}^2 - m_{\widetilde{\tau}}^2) \\ p_{\tau} &= \frac{(m_{\widetilde{\chi}_2^0}^2 - m_{\widetilde{\tau}}^2)}{2m_{\widetilde{\chi}_2^0}} \end{aligned} \tag{7.3}$$

It is useful to distinguish between the two taus, which one is the closest to the $\widetilde{\chi}_2^0$ in the decay chain. They are normally labeled τ_N and τ_F, describing

[1] To justify this simplification we remark that the SUSY mass spectrum of the model under consideration spans from ∼150 GeV to about 800 GeV, see Table 7.1.

which of them is near and far from $\widetilde{\chi}_2^0$ respectively. In the rest frame of $\widetilde{\tau}$, expressions for p_{τ_N} and p_{τ_F} are obtained in the same manner as above, resulting in

$$\begin{aligned} p_{\tau_N} &= \frac{(m^2_{\widetilde{\chi}_2^0} - m^2_{\widetilde{\tau}})}{2m_{\widetilde{\tau}}} \\ p_{\tau_F} &= \frac{(m^2_{\widetilde{\tau}} - m^2_{\widetilde{\chi}_1^0})}{2m_{\widetilde{\tau}}} \end{aligned} \tag{7.4}$$

The invariant mass for the two taus τ_N and τ_F is given as

$$\begin{aligned} m^2_{\tau\tau} &= (E_{\tau_N} + E_{\tau_F})^2 - (\mathbf{p}_{\tau_N} + \mathbf{p}_{\tau_F})^2 \\ &= 2p_{\tau_N}p_{\tau_F} - 2\mathbf{p}_{\tau_N}\mathbf{p}_{\tau_F} \\ &= 2p_{\tau_N}p_{\tau_F}(1 - \cos(\theta)) \end{aligned} \tag{7.5}$$

The maximum value of the invariant mass corresponds to the situation where the two taus are back-to-back in the rest frame of $\widetilde{\tau}$, i.e. where $\cos(\theta) = -1$. The resulting mathematical expression for the maximum value of the invariant mass for the two τ's can then be given as

$$m^{max}_{\tau\tau} = m_{\widetilde{\chi}_2^0}\sqrt{1 - \frac{m^2_{\widetilde{\tau}}}{m^2_{\widetilde{\chi}_2^0}}}\sqrt{1 - \frac{m^2_{\widetilde{\chi}_1^0}}{m^2_{\widetilde{\tau}}}} \tag{7.6}$$

Equation 7.6 shows that the theoretical end-point of the invariant mass distribution of the two taus is determined by the masses of the supersymmetric particles involved in the decay chain.

7.4.1 The sparticle masses

The parameters given in Eq. 7.1 uniquely define the SUSY model under consideration, and hence the masses of the sparticles in this benchmark point. The sparticle masses for lower energy scales are obtained by solving the renormalisation group equations (RGEs). There exist different computer programs deriving the sparticle masses using RGEs, so-called SUSY spectrum generators. We have used a web-page written by Sabine Kraml *et al* [57] that

compares different spectrum generators [58] [59]. The results calculated with the Isajet spectrum generator are listed in Table 7.1.

Particle	Mass [GeV]	Particle	Mass [GeV]	Particle	Mass [GeV]
Gauginos:		**Higgs:**		$\widetilde{e}_R, \widetilde{\mu}_R$	152.7
$\widetilde{\chi}_1^0$	136.7	h^0	112.7	$\widetilde{\tau}_1$	147.7
$\widetilde{\chi}_2^0$	262.0	H^0	516.5	$\widetilde{\tau}_2$	253.2
$\widetilde{\chi}_3^0$	462.0	A^0	512.8	$\widetilde{u}_L, \widetilde{d}_L . \widetilde{s}_L \widetilde{c}_L$	~ 765.0
$\widetilde{\chi}_4^0$	480.2	$H^\pm$	522.3	$\widetilde{u}_R, \widetilde{d}_R . \widetilde{s}_R, \widetilde{c}_R$	~ 735.0
$\widetilde{\chi}_1^\pm$	262.2	**Sfermions:**		$\widetilde{t}_1$	564.9
$\widetilde{\chi}_2^\pm$	479.4	$\widetilde{\nu}_{e,\mu,\tau}$	237.4	$\widetilde{t}_2$	765.4
$\widetilde{g}$	829.1	$\widetilde{e}_L, \widetilde{\mu}_L$	252.5	$\widetilde{b}_1$	702.3
				$\widetilde{b}_2$	732.3

Table 7.1: The table shows the theoretical masses of the supersymmetric particles within our benchmark point defined by the parameters listed in Eq. 7.1. The masses are calculated with the *Isajet* SUSY spectrum generator, obtained from Ref. [57].

The helicity states of the sfermions, which have spin = 0, refer to the helicity states of their SM partners, where L and R, denoting left- and right-handed states respectively. Table 7.1 shows that the three sneutrinos, as well as the two first generations of charged sleptons for each helicity state, are degenerate in mass. The u, d, s, c squarks are almost degenerate in mass for the corresponding left- and right-handed partners separately. The stau, together with the top- and b-squarks are partners of mixed helicity states of the corresponding SM particles and are hence labeled 1 and 2 instead of L and R.

Inserting the masses of the SUSY particles involved in the decay chain of this analysis, $m_{\widetilde{\chi}_2^0}$, $m_{\widetilde{\tau}_1}$ and $m_{\widetilde{\chi}_1^0}$ in Eq. 7.6 gives an end-point

$$m_{\tau\tau}^{max} = 82 \pm 2 \text{ GeV}. \tag{7.7}$$

The sparticle masses listed in Table 7.1 and hence the end-point of the invariant mass distribution, $m_{\tau\tau}^{max}$ given in Eq. 7.7 depends on the value of some SM parameters. These are the top-quark mass, which in this calculation is set to the value $m_t = 175.0$ GeV, the mass of the b-quark, set to $m_b = 4.2$ GeV, and the value of the strong coupling constant, which is set to the value $\alpha_s = 0.1172$. As mentioned, there exists different SUSY spectrum generators, and the SUSY masses obtained from them differs slightly. This means

that the theoretical end-point of an invariant mass distribution depends not only on the SM input, but also on how the RGEs are solved to calculate the SUSY masses. Hence, the value of $m_{\tau\tau}^{max}$ given in Eq. 7.7 is not unique. It should be noted that the mass of the lightest Higgs boson in listed in Table 7.1 is just below the LEP limit. This mass is very sensitive to the top-quark mass, meaning that higher accuracy of m_t will influence m_{h^0}. By varying the top-quark mass $\Delta m_t \pm 1$ GeV would effectively cause a variation in the Higgs mass $\Delta m_{h^0} \pm 1$ GeV.

7.5 Samples used in the analysis

This is a full-simulation study of the ATLAS detector. Since we are expecting one of the taus in the decay chain shown in Figure 7.3 to be soft, we have chosen the tau1p3p algorithm for reconstructing taus in all samples used in this analysis. Table 7.2 lists the samples used in this analysis together with the cross sections at which the different processes are expected to be produced at the LHC.

Sample	**Number of events**	**Cross section [pb]**	**Data set**
BACKGROUND:			
$t\bar{t}^*$	349 800	461	5200
$Z \to \tau\tau^{**}$	149 200	246	5188
$W \to \tau\nu^{***}$	338 700	5536	5107
QCD[1] $35 \leq p_T \leq 70$ GeV	153 750	$9.33 \cdot 10^7$	5011
QCD[2] $70 \leq p_T \leq 140$ GeV	335 550	$5.88 \cdot 10^6$	5012
QCD[3] $140 \leq p_T \leq 280$ GeV	10 000	$3.08 \cdot 10^5$	5013
SIGNAL:			
SUSY	198600	7.43	5401
GENERATOR LEVEL‡:			
$t\bar{t}$	10000	11.66	5200
SUSY	80 000	7.43	5401

Table 7.2: Table of data sets used in this analysis with corresponding cross section at which the different processes are expected to be produced at the LHC. The cross sections for the samples labeled with asterisks corresponds to the following processes: *) $t \to Wb$, where one of the W's is required to decay leptonically, **) $Z \to \tau\tau$, ***) $W \to \tau\nu$. ‡: The generator level samples are private productions, generated using ATHENA 12.06 with CSC jobOptions.

7.6 Invariant mass distributions at generator level

At generator level, information about the *true* tau is available, that is information about the tau implemented at generator level in the MC Truth samples. At this level, the invariant mass distribution for the SUSY signal is expected to have a triangular shape with a sharp cut-off at $m_{\tau\tau}^{max}$, given by Eq. 7.6, due to the energy carried by the LSP, $\widetilde{\chi}_1^0$. Figure 7.4 shows the invariant mass distribution for true taus, for the signal process to the left and for taus origin from $t\bar{t}$ processes, where each t decays as $t \rightarrow b \rightarrow \tau\nu b$, to the right. As we will see later the background is dominated by $t\bar{t}$ processes, and the background is therefore restricted to this process throughout this section, since it is shown mostly for illustration.

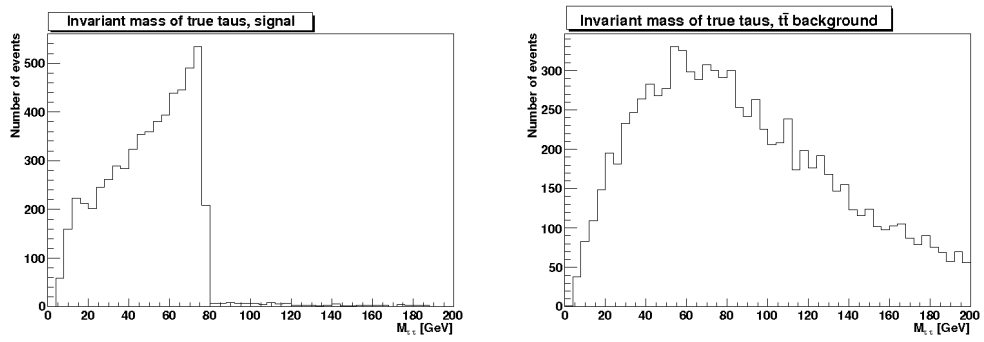

Figure 7.4: The figure shows invariant mass distributions for true taus at generator level. The l.h.s shows $m_{\tau\tau}$ for taus originating from the SUSY signal process, and r.h.s shows this for taus originating from the process $t \rightarrow Wb \rightarrow \tau\nu b$. In both cases, only opposite sign taus originating directly from the process in question were taken into account.

In both cases, only opposite sign taus originating directly from the process in question were taken into account. We see a clear end-point in the invariant mass distribution for taus originating from the signal process at ∼80 GeV. The two distributions are easy to distinguish at this point. It should however be kept in mind that the cross section for the $t\bar{t}$ background at reconstructed level, listed in Table 7.2, is ~ 60 times larger than the cross section for the signal process.

It is not possible to detect the tau directly, due to its short lifetime, $\tau_0 \sim 2.9 \cdot 10^{-13}$ seconds [3], as was discussed in Chapter 6. In reconstructed data, tau-leptons are reconstructed from its visible hadronic decay products, meaning the detectable particles. Since the neutrino escapes detection, the energy of

reconstructed taus are less than for true taus, which influences the invariant mass distribution of the taus, and hence also the end-point. Figure 7.5 shows the invariant mass distribution where the energy and momentum of taus have been calculated from its hadronic single- and three-prong decay products. The distributions are here effectively smeared for both the signal and the $t\bar{t}$ background distribution, and the end-point for the signal sample slightly shifted.

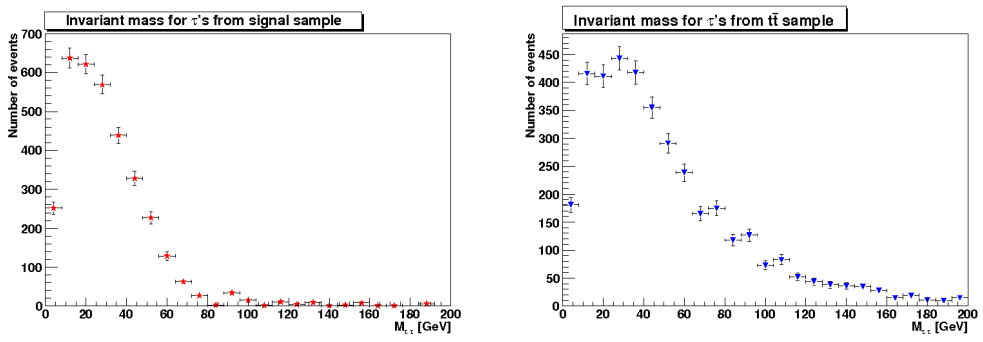

Figure 7.5: The figure shows invariant mass distributions of hadronically decaying taus at generator level. The l.h.s shows $m_{\tau\tau}$ for taus originating from the SUSY signal process, and r.h.s shows this for taus origin from $t\bar{t}$ processes. In both cases, only opposite sign taus originating directly from the process in question were taken into account.

Figure 7.6 shows the invariant mass distribution of taus where energy and momentum have been calculated using only the single-prong decay products. It is verified that reconstruction of these decay modes contains less uncertainty than the reconstruction of three prongs taus [60], since the latter cases are more difficult to distinguish from QCD jets.

Again, only opposite sign taus originating directly from the process in question were taken into account. This information, i.e. information about the particle from which tau decays, is not available at reconstructed level. Figure 7.7 therefore shows the invariant mass distributions for all single prong decaying taus in the samples used, where different tau pairs have been constructed with combinatorics. As mentioned in Section 7.3, the two taus originating from the signal process will have opposite electric charge, as they are both a result of the $\widetilde{\chi}_2^0$ decay. By combining all possible pairs of taus occurring in the signal sample we also get contributions from same sign (SS) tau pairs. This means that underlying processes producing taus are present in the signal sample. By subtracting the invariant mass distribution for tau pairs with SS from that of tau pairs with opposite sign (OS), we can reduce contributions

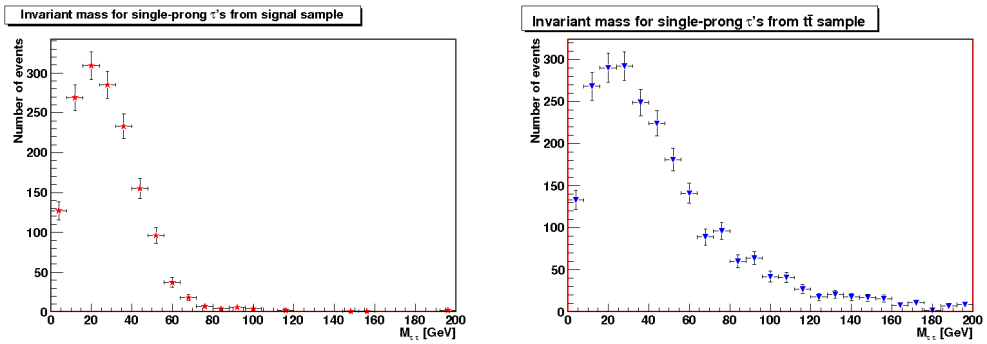

Figure 7.6: The figure shows the invariant mass distributions of hadronically single-prong decaying taus at generator level. The l.h.s shows $m_{\tau\tau}$ for taus originating from the SUSY signal process, and r.h.s shows this for taus origin from $t\bar{t}$ processes. In both cases, only opposite sign taus originating directly from the process in question were taken into account.

from these underlying processes, by assuming that processes producing uncorrelated taus have equal probability of producing SS tau-pairs as OS pairs. With this method we can also reduce the rate of misidentified taus within the signal sample at reconstructed level. In Figure 7.7 distributions for OS tau pairs and SS tau pairs are shown, as well as the distribution where that of SS pairs has been subtracted from the OS distribution.

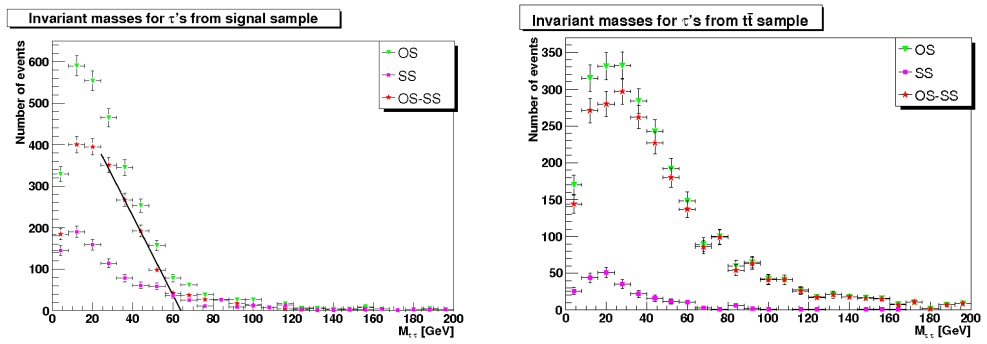

Figure 7.7: The figure shows invariant mass distributions for single prong decaying taus originating from processes within the SUSY signal sample at generator level.

At reconstructed level, there is a cut in the transverse momentum of taus; only taus with $p_T > 9$ GeV are reconstructed[2]. By introducing this cut at generator level we can see how much the invariant mass distributions are

[2] This cut is actually on the leading charged pion in the tau decay.

affected by this cut, and hence get a clearer view of the shape of the distribution at reconstructed level. Figure 7.8 shows invariant mass distributions for SS tau pairs, OS tau pairs and the distribution where that of SS pairs has been subtracted from that of OS pairs, for single prong decaying taus with $p_T > 9$ GeV.

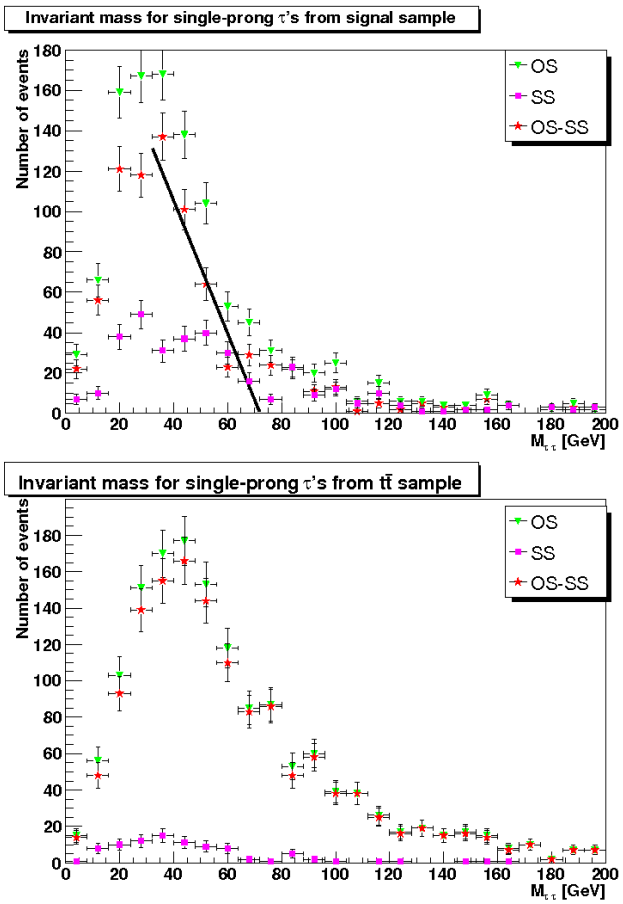

Figure 7.8: The figure shows invariant mass distributions for single prong decaying taus at generator level with a cut in the transverse momentum of taus, $p_T > 9$ GeV, for taus originating from processes within the SUSY signal sample at the top and for taus originating from processes within the $t\bar{t}$ sample at the bottom.

We see that the cut on the transverse momentum of taus has a certain impact on the distributions; number of events is drastically reduced and the peaks in the distributions are shifted to higher energies. The distributions for taus from the signal sample have a clear bump located around 70 GeV. This bump was also visible in Figure 7.7, but due to lower statistics it is

much more pronounced in Figure 7.8. At this point we have selected taus that should correspond to selections performed by the tau reconstruction algorithm tau1p3p, for single prong taus at reconstructed level, and the shape of the invariant mass distribution in Figure 7.8 should hence be recognisable at reconstructed level. This will be discussed in Section 7.8.

In the process of determining an end-point of the invariant mass distribution for taus originating from the SUSY signal process at reconstructed level, a linear fit procedure has been carried out throughout this analysis. Figure 7.7 and 7.8 show a linear fit to the invariant mass distribution in the case where that of SS pairs has been subtracted from the OS distribution. Due to the differences in the distributions, the fit ranges in the two cases are different. This excludes a comparison of the fit parameters, i.e. slope and end-point, in this case.

At reconstructed level, the statistic is low and the method of a linear fit is not ideal. However, it may provide an indication of the position of the desired end-point if a linear fit to the invariant mass distribution at reconstructed level, in the same range as the one at generator level, shown in Figure 7.8, has a similar slope. This will be discussed in Section 7.8. In the further analysis, we are considering only single prong taus decaying hadronically.

7.7 Background rejection

The cross section for standard model processes range many orders of magnitude over the cross section for the SUSY signal process. The number of events for the different samples used in this analysis, listed in Table 7.2, are incidental. To be in accordance with the expected amount of data produced from different processes within a certain time frame , the number of simulated events should have been in agreement with corresponding cross sections. There was no resources to fully simulate a substantial amount of background events, and the study of background rejection is therefore statistically limited.

To give an estimate of the order of magnitude of the production rate for the different processes, we have selected events from the different processes containing two taus and *scaled* it up such that the number of events corresponds to 30 fb^{-1}. Figure 7.9 shows the invariant mass distribution for two taus originating from different processes, where the distribution of SS tau pairs has then been subtracted from that of OS tau pairs. The QCD background

has been omitted since these processes are 100 % rejected with a simple cut requiring the missing energy in the event to be above 100 GeV, see Table 7.3.

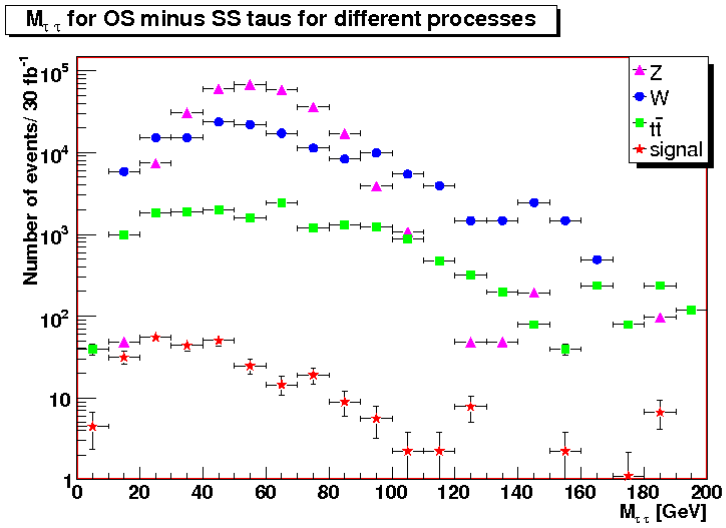

Figure 7.9: The figure shows invariant mass distributions for tau pairs originating from different processes, where the distribution of SS tau pairs has been subtracted from the OS tau pair distribution. Number of events are normalised to 30 fb^{-1}.

It should be stressed that this is a drastic simplification and that the purpose of Figure 7.9 is to give an estimate of the order of magnitude at which the different processes are expected to be produced at the LHC. In Figure 7.9, the scale on the axis corresponding to number of events is logarithmic, and it is clear that the signal will be drown by background events. The shapes of the invariant mass distributions are affected by the logarithmic scale.

We have attempted different strategies in the process of reducing this standard model background, and some of them will be summarised in this section. We start by discussing some general cuts which will remove most of the standard model background, based on the main characteristics of the SUSY signal, discussed in Section 7.3, before discussing cuts to optimise the analysis.

7.7.1 General cuts

The main characteristics for the SUSY signal process is the presence of two taus with opposite sign in the event, a significant amount of missing energy,

and some high energetic jets. Table 7.3 shows the background rejection for different standard model processes and for the SUSY signal process where the cuts performed are divided in three criteria. Criteria 1 selects event containing at least two single prong decaying taus, criteria two selects events with number of taus > 2 and $E_T^{miss} > 100$ GeV, and criteria 3 selects events with an additional cut, requiring the transverse momentum of the leading jet to be above 100 GeV. The numbers in parenthesis corresponds to number of events normalised to 30 fb^{-1}.

Process	**Number of events**	**Passed cut 1**	**Passed cut 2**	**Passed cut 3**
Z	149 200 (7 380 200)	6953 (336 900)	35 (1670)	32 (1551)
W	338 700 $(1.7 \cdot 10^8)$	651 (319 300)	6 (2940)	4 (1800)
QCD^1	153 750 $(2.8 \cdot 10^{12})$	16 $(2.9 \cdot 10^8)$	0 (0)	0 (0)
QCD^2	335 550 $(1.8 \cdot 10^{11})$	29 $(1.5 \cdot 10^7)$	0 (0)	0 (0)
QCD^3	10 000 $(9.2 \cdot 10^9)$	1 (924 000)	0 (0)	0 (0)
$\mathbf{t\bar{t}}$	349 300 (13 830 100)	870 (34 350)	161 (6360)	116 (4582)
SUSY	198 600 (222 450)	569 (640)	478 (535)	454 (508)

Table 7.3: To reduce background we perform cuts on some criteria characteristic for the SUSY signal process. Here we distinguish the cuts in three different criteria: cut 1 selects events containing at least two single prong decaying taus, cut 2 selects events which in addition have $E_T^{miss} > 100$ GeV and cut 3 select events with the extra condition that the energy of the leading jet in the event is above 100 GeV.

These cuts reject most of the background from standard model processes, but a significant amount of the top events pass criteria 3. In this $t\bar{t}$-process, each top decays as $t \to Wb \to \tau\nu b$, resulting in a final state consisting of $2\tau + 2b$-jets $+E_T^{miss}$, the latter due to escaping neutrinos. This signature is very similar to that of the SUSY signal process discussed in Section 7.3. Figure 7.10 shows a sketch of the signal and background processes where the similarities of the two processes have been emphasized, indicated by different colours.

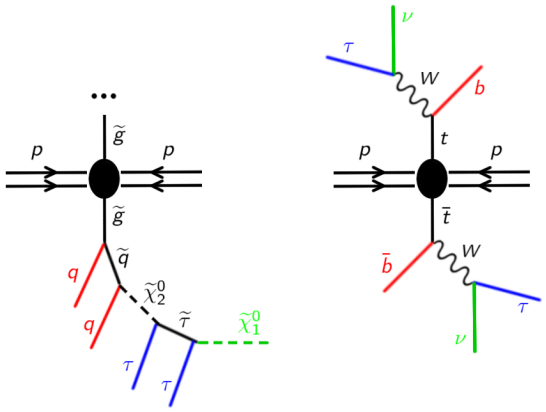

Figure 7.10: The figure shows a sketch of the SUSY signal process to the left, and the $t\bar{t}$-process to the right, where each top decays as $t \to Wb \to \tau\nu b$. The similarities of the final products of both processes are indicated with colours. The red lines denotes two high energetic jets, the blue lines corresponds to the two outgoing taus and green represents undetectable particles which gives rise to missing energy in the event.

Some of the events originating from the processes $Z \to \tau\tau$ and $W \to \tau\nu$ also pass criteria 3, but the statistics for these cases are quite limited, especially for the W sample. We believe that the W background can be reduced by 50% by requiring that the two taus selected should have opposite electric charge, but due to low statistics this requirement has been omitted.

7.7.2 Optimisation cuts

The cross section for $t\bar{t}$ processes, where at least one of the top quarks is required to decay leptonically, is 461 pb, whereas the cross section for the SUSY signal process is 7.43 pb. The cross section for the process $Z \to \tau\tau$ is 246 pb. This means that the cross section for the $t\bar{t}$ background is ~ 60 times larger than the cross section for our signal process, whereas the cross section for the Z background is ~ 30 larger. It is therefore necessary to find a good and efficient way to reduce this background and at the same time to keep as much of the signal events as possible. Different strategies have been attempted in order to get the most effective result. In the following, 4 different cut methods will be discussed. Due to low background statistics, we have not required the two taus in the events selected to have opposite charge.

Method 1: High energetic taus versus low energetic taus

The SUSY signal process $\widetilde{\chi}_2^0 \rightarrow \widetilde{\tau}\tau_N \rightarrow \tau_N\tau_F\widetilde{\chi}_1^0$, is expected to produce one high energetic and one low energetic tau, τ_N and τ_F respectively. The high energetic τ_N is a result of the large mass difference between $\widetilde{\chi}_2^0$ and $\widetilde{\tau}$, whereas the soft tau is a result of the small mass difference between $\widetilde{\chi}_1^0$ and the $\widetilde{\tau}$ which characterizes the coannihilation region. For the $t\bar{t}$ and the W background, no such correlation is expected since each tau is produced separately in these processes. For the Z background, where $Z \rightarrow \tau\tau$, both taus are expected to carry an approximately equal amounts of the energy of the decaying resonance. A scatter plot between the momentum of the two taus should hence provide some information that could be used in order to reduce this background. Figure 7.11 shows the transverse momentum of the leading tau versus the transverse momentum of the next-to-leading tau in the event for single prong decaying taus at generator level.

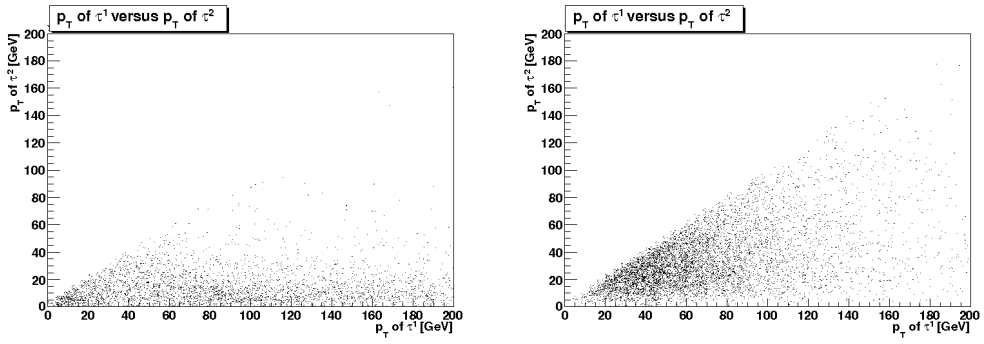

Figure 7.11: The figure shows the correlation between the transverse momentum of the two taus for the signal sample. The l.h.s. shows this correlation for taus from the SUSY signal sample, whereas the r.h.s shows this correlation for taus from the $t\bar{t}$ background sample.

For the signal sample, we see that more events contain one tau with $p_T \lesssim 10$ GeV than for the $t\bar{t}$ background sample, especially in the region where the leading tau has $p_T > 70$ GeV. However, in the tau-reconstruction algorithm tau1p3p used to reconstruct taus in the samples used in this analysis, there is a default cut on $p_T^{\pi^\pm} = 9$ GeV. This means that most of this information is not available at the reconstructed level, as is shown in Figure 7.12.

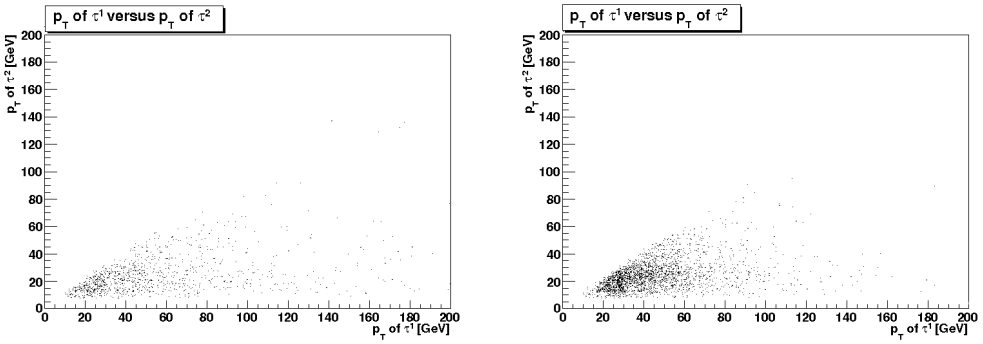

Figure 7.12: The figure shows a scatter plot between the momentum of the two taus at reconstructed level, for the signal sample to the left and for the $t\bar{t}$ background sample to the right. The default cut on the transverse momentum of taus reconstructed with tau1p3p is at 9 GeV.

Method 2: Missing energy versus jet-energy

Figure 7.13 shows the correlation between missing transverse energy, E_T^{miss}, and the energy of the leading jet, E^{jet1} for the signal sample to the left and for SM background samples to the right. The distribution is shown for events before requiring the presence of at least two taus in the events.

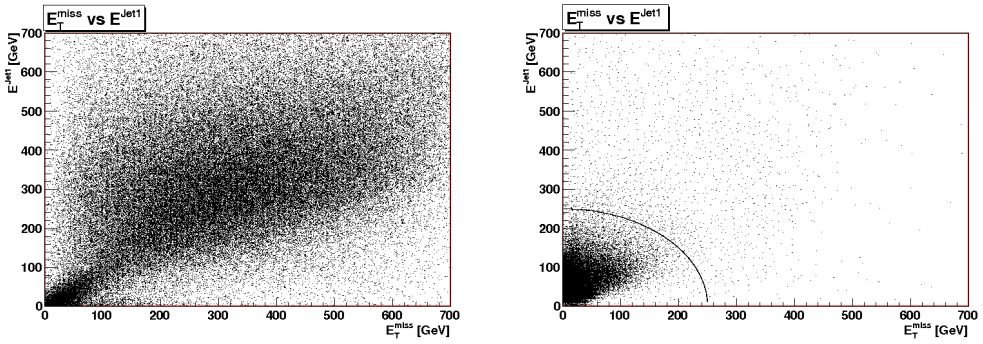

Figure 7.13: The figure shows scatter plots of the missing energy and the energy of the leading jet in the event, before requiring the presence of at least two taus in the event. The l.h.s shows this for the signal sample, and the r.h.s. for all background samples.

There is a significant difference in the E_T^{miss} vs. E^{jet1} distributions for the signal and the background processes. The distribution for the background events tends to cluster in a *cone* in the low energetic area of the scatter plot, whereas the signal distribution is more spread. This led to the introduction of a correlated circular cut in the plane spanned by these two variables. The

circular cut is indicated in the plot representing the background events in Figure 7.13.

Figure 7.13 show the correlation between E_T^{miss} and E^{jet1} *without* requiring the presence of two taus in the event. These plots are mainly included to show a good method of rejecting standard model background in general, and specifically $t\bar{t}$ background, in cases where the distribution between these variables is different for the process under investigation. The same distributions are shown in Figure 7.14, where the events selected are required to contain at least two taus. The same circular cut can successfully be applied to reduce the background.

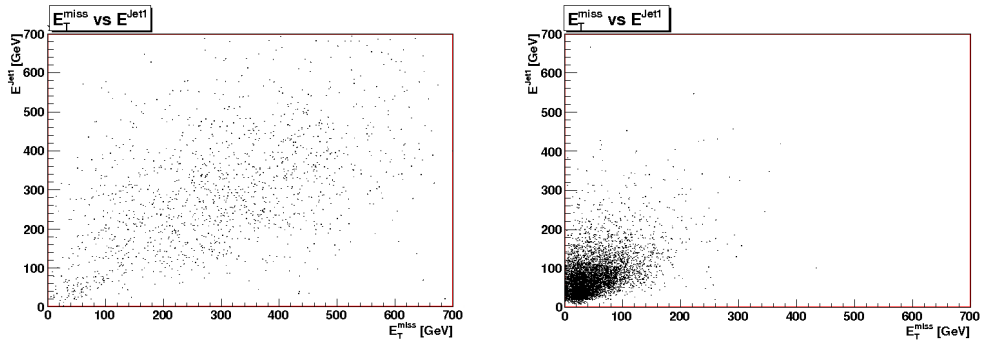

Figure 7.14: The figures shows scatter plots of E_T^{miss} versus E^{jet1}, after selecting events that contains at least two taus. The l.h.s shows the distribution for SUSY signal events, whereas the r.h.s shows the distribution for background events.

The circular cut is very effective for rejecting SM background in general, and especially for rejecting $t\bar{t}$ background which is characterised by missing energy and highly energetic jets. We found however, that by plotting the missing transverse energy versus the sum of the energy of the *two* leading jets in the event and perform cuts in this plane, we could further improve the background rejection. Figure 7.15 shows the scatter plot of E_T^{miss} versus $E^{jet1} + E^{jet2}$, before selecting events containing at least two taus.

In this case, an elliptic cut is introduced to reduce the background. This is indicated in the plot on the r.h.s of Figure 7.15, showing the distribution for the SM background samples before requiring the presence of two taus in the events. Again, these plots are included to show an effective cut method to reject SM background in general. The same distribution for events containing at least two taus is shown in Figure 7.16, where events originating from the SM background processes are shown in black and events from the signal process are shown in red.

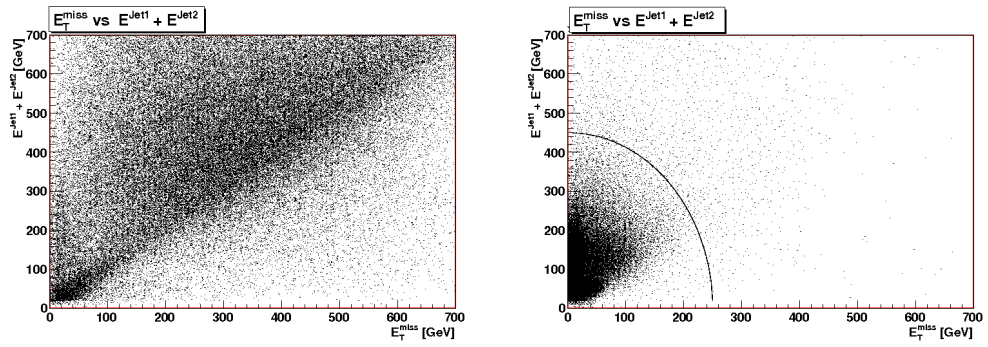

Figure 7.15: The figures shows scatter plots of E_T^{miss} versus $E^{jet1} + E^{jet2}$, before selecting events that contains at least two taus. The l.h.s shows the distribution for SUSY signal events, whereas the r.h.s shows the distribution for background events.

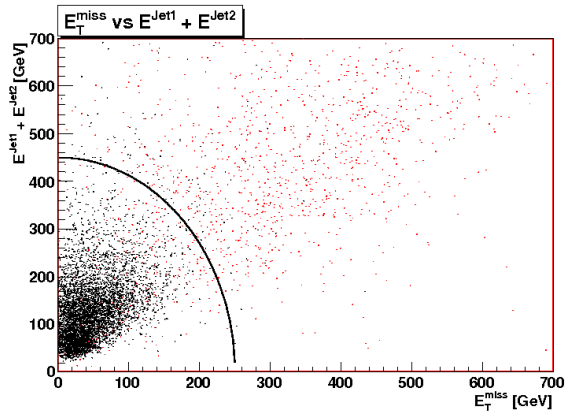

Figure 7.16: The figure shows a scatter plot of E_T^{miss} vs. $E^{jet1} + E^{jet2}$, where the signal distribution is shown in red and the background distribution is in black. The distribution looks quite different for the two processes, and inspired us to introduce an elliptic cut to separate background from signal, as indicated in the figure.

In this specific elliptical cut, the value of the semi major axis, corresponding to the $E^{jet1} + E^{jet2}$ axis, is set to 450 GeV, whereas the value of the semi minor axis, which corresponds to the E_T^{miss} axis, is set to 250 GeV. In order to achieve the best result, i.e. to keep as much signal as possible and at the same time reject as much background as possible, we have tried different sizes and shapes for the elliptic cut by varying the values for the semi major and semi minor axes. The number of events passing different elliptical cuts from the signal process and the $t\bar{t}$- and Z background processes are listed in Table 7.4, together with the *sensitivity* for the different cuts. The sensitivity

S is defined as

$$S = \frac{\#\text{ of signal events}}{\sqrt{\#\text{ of background events} + \#\text{ of signal events}}}, \tag{7.8}$$

and serves as a measure of how good the background rejection is. The first row of each cut in Table 7.4 lists number of events passing the cuts from the sample used, whereas the numbers in parenthesis show the expected number of events for an integrated luminosity of 30 fb^{-1}. The sensitivity is calculated for 30 fb^{-1}. Only one of the events from the W sample passes some of these cuts, and is therefore not listed in the following tables throughout this section. The sensitivities are calculated without this one W event.

Due to low statistics, no errors have been calculated. The highest achieved sensitivity of Table 7.4 is 11.88. However, only certain cut values are listed. By scanning over all cut values in the parameter space spanned by the variables E_T^{miss} versus $E^{jet1} + E^{jet2}$, we could probably achieve a higher sensitivity. Invariant mass distributions and analysis of kinematic properties of the signal will be discussed in Section 7.8.

Missing E_T →	**200 GeV**	**S**	**250 GeV**	**S**	**300 GeV**	**S**
$E^{jet1} + E^{jet2}$ ↓	**signal/tt/Z**		**signal/tt/Z**		**signal/tt/Z**	
350 GeV	464/ 76/ 31 (519/3002/1503)	7.56	450/ 58/ 25 (504/1291/2211)	8.21	433/ 51/ 23 (488/2030/1115)	8.33
400 GeV	455/ 57/ 22 (509/2251/1067)	8.48	438/ 44/ 14 (491/1738/ 678)	9.32	422/ 38/ 13 (473/1501/ 630)	9.50
450 GeV	451/ 48/ 16 (505/1869/ 776)	9.19	428/ 38/ 11 (479/1501/ 533)	9.77	409/ 31/ 9 (458/1225/ 436)	10.16
500 GeV	445/ 42/ 14 (498/1659/ 678)	9.59	417/ 33/ 6 (467/1303/291)	10.44	390/ 21/ 6 (436/ 830/ 261)	11.28

Table cont.:

Missing E_T →	**350 GeV**	**S**	**400 GeV**	**S**	**450 GeV**	**S**
$E^{jet1} + E^{jet2}$ ↓	**signal/tt/Z**		**signal/tt/Z**		**signal/tt/Z**	
350 GeV	429/ 49/ 23 (480/1937/1115)	8.35	422/ 44/ 20 (473/1738/ 969)	8.65	409/ 40/ 20 (458/1580/ 969)	8.63
400 GeV	412/ 32/ 12 (461/1264/ 582)	9.86	398/ 29/ 12 (446/1146/ 582)	9.83	384/ 26/ 11 (430/ 1027/ 533)	9.91
450 GeV	388/ 24/ 8 (434/ 948/ 388)	10.56	366/ 22/ 8 (409/ 869/ 388)	10.28	356/ 22/ 8 (399/ 869/ 388)	10.04
500 GeV	367/ 15/ 6 (411/ 442/ 291)	11.69	352/ 13/ 5 (494/ 513/ 248)	11.88	328/ 12/ 4 (367/ 474/ 194)	11.64

Table 7.4: The table lists number of events passing different elliptic cuts performed in the plane spanned by the variables E_T^{miss} versus $E^{jet1} + E^{jet2}$, together with the sensitivity, S, for events normalised to 30 fb^{-1}. Number of events in the first row of each cut lists number of events passing the cuts from the sample used, whereas the number in parenthesis are normalised to 30 fb^{-1}. The table presents cuts performed with Method 2.

Method 3: E_T^{miss} versus p_T of next-to-leading τ

A third method is to consider the plane spanned by the two variables E_T^{miss} versus p_T of next-to-leading τ in the event. In the signal process, the $\widetilde{\tau}$ decays to $\tau + \widetilde{\chi}_1^0$, where the latter is responsible for missing energy in the event and the τ is expected to be next-to-leading τ in the event. For a boosted system we expect these two variables to be highly correlated; if $\widetilde{\chi}_1^0$ carries a larger fraction of the total energy, the τ carries a smaller fraction and vice versa. This again invites for performing cuts in an elliptic fashion. The number of events from the sample used that passes different cuts, together with the sensitivity, are listed in Table 7.5. The sensitivities have been calculated for 30 fb^{-1}. The numbers in parenthesis corresponds to number of events normalised to 30 fb^{-1}.

This method is particularly efficient for reducing the Z background, but also to a certain degree $t\bar{t}$ background.

We see that with this method we achieve a sensitivity of 13.7 whereas the method discussed above gave rise to a sensitivity 11.6, where the number of signal events passing the cuts are approximately the same (330 vs. 328).

p_T **of 2nd** $\tau \rightarrow$	**250 GeV**	**S**	**300 GeV**	**S**	**350 GeV**	**S**
$E_T^{miss} \downarrow$	**signal/tt/Z**		**signal/tt/Z**		**signal/tt/Z**	
150 GeV	427/ 61/ 13 (478/2434/ 630)	8.21	426/ 57/ 10 (477/2552/ 485)	9.29	426/ 57/ 9 (477/ 2552/ 436)	9.36
200 GeV	388/ 26/ 6 (435/1027/ 291)	10.56	385/ 24/ 2 (431/ 948/ 485)	11.30	383/ 23/ 0 (429/ 909/ 0)	11.74
250 GeV	334/ 12/ 5 (374/ 474/ 242)	11.59	331/ 10/ 1 (371/ 395/ 48)	13.07	330/ 9/ 0 (370/ 356/ 0)	13.73
300 GeV	274/ 7/ 5 (307/ 277/ 242)	11.00	269/ 6/ 1 (301/ 237/ 48)	12.54	269/ 4/ 0 (301/ 158/ 0)	14.06

Table 7.5: The table lists number of events from different processes passing various elliptic cuts performed in the plane spanned by the two variables E_T^{miss} and p_T of 2nd the τ in the event. The corresponding sensitivities have been calculated for number of events normalised to 30 fb^{-1}. The table presents cuts performed with Method 3.

Again, a scan over parameter space with different cuts would help to find the highest sensitivity. The limitation on available background limits this method, but we see that manage to reduce contributions from Z events from the sample used to 0, and the contributions from the $t\bar{t}$ sample to 4 events passing the most drastic cut in Table 7.5. The sensitivity corresponding to this cut is 14.06. The invariant mass distribution for the signal events passing this cut is shown in Section 7.8.

Method 4: E_T^{miss} + jet-energy versus p_T of next-to-leading τ

Another method is to combine the missing transverse energy and the energy of the two leading jets in the event and to plot them against the transverse momentum of the next-to-leading tau in the event. Also here elliptic cuts have been performed, and the number of events passing different cuts are listed in Table 7.6. The sensitivities have been calculated for number of events normalised to 30 fb^{-1}. None of the events from the W sample pass the cuts performed.

We would expect the next-to-leading tau in the signal event to be soft due to the small mass difference between $\widetilde{\tau}$ and $\widetilde{\chi}_1^0$. Still, we see that many of the signal events pass the elliptic cut where the semi minor axis corresponding to this variable is set to values up to 450 GeV. A reason for this could be

$E_T^{miss} + E^{jet1} + E^{jet2} \rightarrow$	**600 GeV**	**S**	**700 GeV**	**S**	**800 GeV**	**S**
p_T **of 2nd** $\tau \downarrow$	**signal/tt/Z**		**signal/tt/Z**		**signal/tt/Z**	
250 GeV	363/ 20/ 12 (407/ 790/ 582)	9.97	312/ 12/ 9 (349/ 474/ 436)	10.20	234/ 10/ 7 (263/ 395/ 339)	8.60
300 GeV	362/ 18/ 7 (405/ 711/ 336)	10.88	310/ 10/ 5 (347/ 395/ 248)	11.35	229/ 7/ 4 (257/ 277/ 194)	9.78
350 GeV	361/ 18/ 6 (404/ 711/ 291)	11.01	309/ 10/ 5 (346/ 395/ 248)	11.32	229/ 6/ 2 (257/ 237/ 97)	10.73
400 GeV	361/ 16/ 5 (404/ 632/ 242)	11.53	309/ 9/ 3 (346/ 355/ 145)	12.10	227/ 5/ 2 (254/ 198/ 97)	11.05
450 GeV	359/ 15/ 4 (402/ 592/ 194)	11.86	307/ 9/ 2 (344/ 355/ 97)	12.34	227/ 5/ 2 (254/ 198/ 97)	11.05

Table 7.6: The table lists number of events from different processes passing various elliptic cuts performed in the plane spanned by the two variables $E_T^{miss} + E^{jet1}$ and p_T of the 2nd τ in the event. The corresponding sensitivities have been calculated for number of events normalised to 30 fb^{-1}. The table presents cuts performed with Method 4.

that the system is boosted.

The three cut methods discussed above give rise to sensitivities in the range 10 to 14. Only certain cut values are listed, and a scan over the cuts in the different parameter spaces would provide a better determination of the best cut method. This however, requires better background statistics. The highest sensitivities are achieved with Method 3. The invariant mass distribution for signal events passing two of these cuts, one with Method 2 and one with Method 3, have been selected for the discussion in the following section.

7.8 Results on invariant mass distributions

This section will show invariant mass distributions for taus, for the SUSY signal sample at generator level as well as at reconstructed level, before and after certain cuts. The SS tau pair distributions have been subtracted from OS tau pair distributions. We have made linear fits to these distributions in order to determine an end-point corresponding to $m_{\tau\tau}^{max}$ given by Eq. 7.6. Three different fit ranges have been selected, motivated by the invariant mass distribution at generator level. The fit parameters, i.e. slope and end-point,

for the different fits are listed in Table 7.7. Invariant mass distributions for the background, where number of events are normalised to 27 fb^{-1}, to be in agreement with signal statistics, will be shown at the end of this section.

Figure 7.8 in Section 7.6 showed the invariant mass distribution for single prong decaying taus with $p_T > 9$ GeV at generator level, where different tau pairs were constructed from all taus within the signal sample. For clarity, this is shown again in Figure 7.17, where the linear fits are indicated.

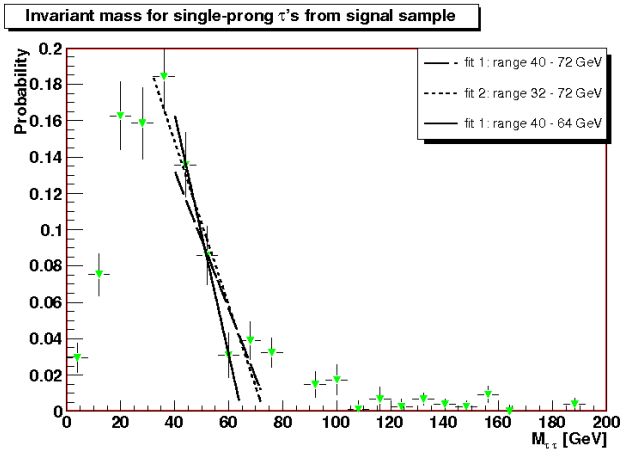

Figure 7.17: The figure shows the invariant mass distribution for single prong decaying taus with $p_T > 9$ GeV at generator level, originating from processes within the SUSY signal sample.

Figure 7.18 shows the same distribution at reconstructed level before any cuts have been performed. The distributions look similar, although the statistic is lower and the statistical error larger for the distribution at reconstructed level, since not all taus from generator level are successfully reconstructed. Due to lower statistics, the extra bump located around 70 GeV is much more pronounced at reconstructed level than at generator level. We believe that this bump is due to $Z \rightarrow \tau\tau$ events, since the invariant mass distribution for single prong decaying taus originating from this process is expected to peak at around 70 GeV. The linear fits shown in the figure will be discussed at the end of this section.

Figure 7.19 and Figure 7.20 show the invariant mass distribution after certain cuts have been performed. Figure 7.19 shows the distribution for signal events which have passed a cut of Method 2 of Section 7.7.2 that gives rise to a sensitivity of 9.77 (Table 7.4), whereas Figure 7.20 shows the distribution for signal events which have passed a cut of Method 3 with corresponding

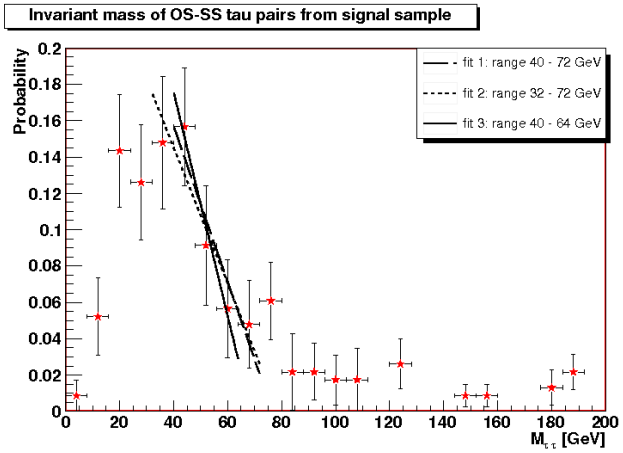

Figure 7.18: The figure shows the invariant mass distribution of two single prong decaying taus originating from processes within the signal sample at reconstructed level.

sensitivity of 14.06, for 30 fb^{-1} (Table 7.5). The statistical error for these distributions are large, but the same shape as in Figure 7.17 and 7.18 is clearly seen. The linear fits indicated in the figures will be discussed below.

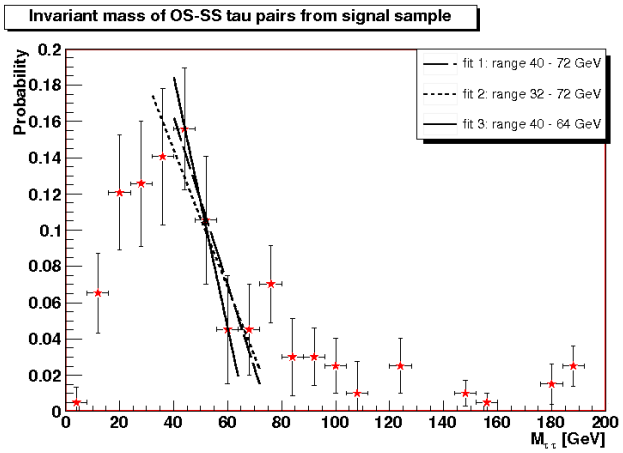

Figure 7.19: The figure shows the invariant mass distributions of two taus originating from processes within the signal sample after a cut of Method 2 in Section 7.7.2 has been performed, which gives rise to a sensitivity of 9.77. This cut is called 'cut 1' in Table 7.7.

For comparison, Figure 7.21 shows the invariant mass distribution for two taus originating from different standard model background processes, normalised to 27 fb^{-1}. The plot on the l.h.s represents the background before

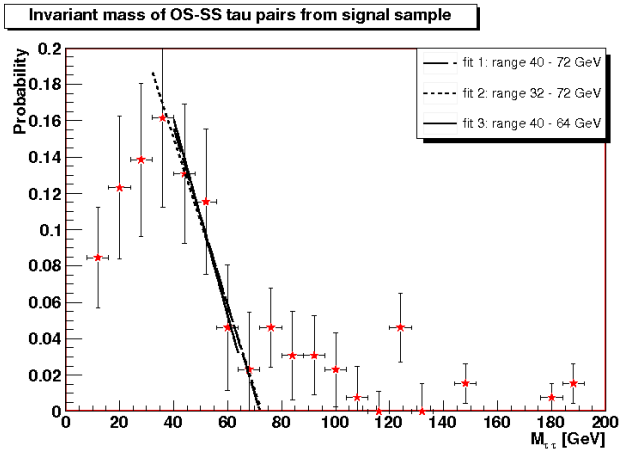

Figure 7.20: The figure shows the invariant mass distributions of two taus originating from processes within the signal sample after a cut of Method 3 in Section 7.7.2 has been performed, which gives rise to a sensitivity of 14.06. This cut is called 'cut 2' in Table 7.7.

any cuts were performed, whereas the plot on the r.h.s. represents the background distribution after performing a cut with Method 2 (Table 7.4), for which the corresponding signal was shown in Figure 7.19. The background corresponding to Figure 7.20 is not shown since only two events within the range of the histogram passed the same cut from all background samples used in this analysis.

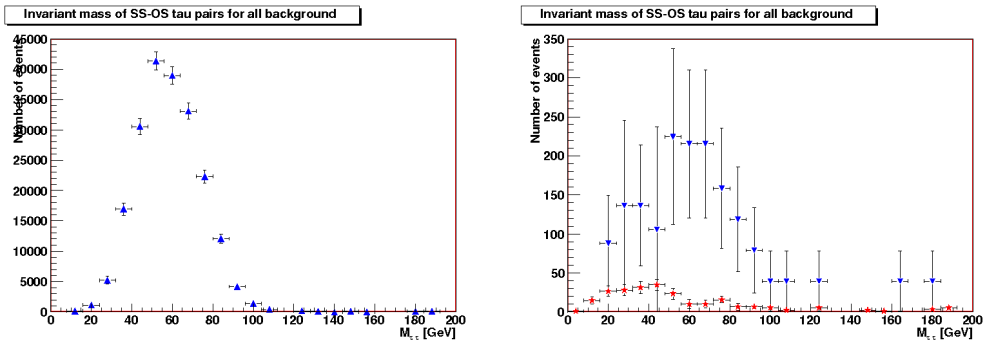

Figure 7.21: The figure shows the invariant mass distributions of two taus originating from SM background processes (W, Z and $t\bar{t}$) where the SS tau pair distributions have been subtracted from the OS sign distribution. The l.h.s shows the background distribution before any cuts have been performed, and the r.h.s shows the distribution together with the signal distribution (in red) after a cut of Method 2 has been performed, which gives rise to a sensitivity of 10.92.

The invariant mass distribution for the background is not significantly different from the signal distribution. This means that a potential discovery of supersymmetry in the coannihilation region requires very efficient methods to separate signal from standard model background. The low background statistics have limited the study of background rejection, although satisfying methods have been developed with the available background. Other ideas for rejecting background could be to search for signal/background differences in a three dimensional space spanned by the variables E_T^{miss}, E_T^{jet1} and p_T of the next-to-leading tau in the event, or to look at the angular distribution between two opposite sign taus as a function of the transverse momentum of the of the next-to-leading tau in the event. These methods have not been investigated in this study.

Table 7.7 lists the slopes and the end-points corresponding to the different fits to the invariant mass distributions for the signal shown above, together with the ranges in which the fits have been made.

Distribution at:	**slope** a $[-10^{-3}$ **GeV**$^{-1}]$	**end-point [GeV]**	**S**
Generator level:			
fit region 1: 40- 72 GeV	3.7 ± 0.4	75.0 ± 3.6	
fit region 2: 32- 72 GeV	4.5 ± 0.3	73.0 ± 2.5	
fit region 3: 40- 64 GeV	6.6 ± 1.3	64.8 ± 2.5	
Reco. level before cuts:			
fit region 1: 40- 72 GeV	4.3 ± 1.6	76.7 ± 7.7	
fit region 2: 32- 72 GeV	3.7 ± 1.2	78.8 ± 8.2	
fit region 3: 40- 64 GeV	6.1 ± 2.2	68.6 ± 7.3	
Reco. level after cut 1:			
fit region 1: 40- 72 GeV	4.6 ± 1.7	75.2 ± 6.9	
fit region 2: 32- 72 GeV	3.8 ± 1.2	78.4 ± 8.2	9.77
fit region 3: 40- 64 GeV	6.9 ± 2.2	66.7 ± 6.3	
Reco. level after cut 2:			
fit region 1: 40- 72 GeV	4.9 ± 2.0	72.1 ± 6.9	
fit region 2: 32- 72 GeV	4.6 ± 1.5	72.6 ± 6.9	14.06
fit region 3: 40- 64 GeV	5.4 ± 3.2	69.9 ± 11.0	

Table 7.7: The table lists slopes and end-points for three different linear fits made to the invariant mass distributions for taus for the signal process.

The fit parameters in all cases are in good agreement within statistical errors. Even in the case where the signal statistic is very limited, specifically after cut 2 in Table 7.7, the kinematic end-points for the different fit ranges do not differ much from those at generator level. This indicates that a kinematic analysis of this kind is possible even with the low signal statistics surviving after background rejection.

It has been checked that 78.4 % of SUSY events pass the trigger on Event Filter level with jet transverse energy cut of 160 GeV (EF_ jet160) before cuts have been performed. After the cuts described in Section 7.7.2, the efficiency for passing the ATLAS trigger chain is $\sim 100\%$.

7.9 Remarks and conclusion

As mentioned in the introduction to this chapter, the background is statistically limited. A full simulation of a substantial amount of background events is a demanding procedure, and in future ATLAS analysis this will be solved by combining full and fast simulation of background events. This however, requires very accurate tuning of the fast simulation. There was no time for such tuning in the scope of this work.

Different cut methods have been performed, and a sensitivity in the order of 14 is achieved. The signal statistic surviving after background rejection is quite limited, thus a balance between high sensitivity and number of surviving signal events has to be kept, to allow kinematic analysis of the invariant mass distribution. The low signal statistics allow only for a very simplified analysis of the kinematic properties of the signal. In order to determine an end-point of the invariant mass distribution of the two taus originating from the signal process, a linear fit procedure has been carried out. The fit parameters of three different fit ranges have been compared, where the ranges selected are motivated by the invariant mass distribution at generator level. Even in the case where the achieved sensitivity is 14.06, and the signal surviving after background rejection is low, both the kinematic end-points and the slopes for the three different fits are in good agreement with the end-points of the same fits at generator level.

All samples used in this analysis use the tau1p3p algorithm for reconstructing taus. This results in the transverse momentum cut-off for reconstructed taus at $p_T > 9$ GeV. We saw that introducing this cut at generator level had a large impact on the invariant mass distribution. We believe that lowering the

p_T threshold of the tau reconstruction algorithm should allow an increase in the signal statistics, without compromising the sensitivity.

In all figures in Section 7.8 showing the invariant mass distribution of two taus originating from the signal sample, there is an extra bump located around 70 GeV. This bump makes it hard to determine an accurate position of the desired end-point since tau pairs may be constructed of taus originating from underlying processes within the signal sample, and not only from the signal process. By subtracting the distribution from SS tau pairs from that of OS tau pairs we reduce contributions from background events within the signal sample, by assuming that processes producing uncorrelated taus have equal probability of producing SS tau-pairs as OS pairs. We believe, however, that the origin of the extra bump may be due to the decay of a Z boson, $Z \rightarrow \tau^+\tau^-$. This process does not produce uncorrelated taus, and the invariant mass distribution for single prong decaying taus would peak at around 70 GeV. A way to investigate this may be to study the invariant mass for other lepton pairs in the decay chain $\widetilde{q} \rightarrow \widetilde{\chi}_2^0 q \rightarrow \widetilde{l}lq \rightarrow llq\widetilde{\chi}_1^0$, to see if the additional peak is present in these distributions as well. In this case the peak should be located around 90 GeV since both muons and electrons can be directly reconstructed and no escaping neutrinos would be involved. If the extra bump is caused by $Z \rightarrow \tau\tau$ decays within the signal sample, a study of the angular distribution between the two taus as a function of the transverse momentum of the next-to-leading tau in the event could perhaps provide some information that could be used to develop methods to prevent contributions from these processes and in this way to obtain a cleaner signal.

The study in this chapter has focused on one certain benchmark point in the coannihilation region. Due to the fact that the invariant mass distribution for the signal is very similar at reconstructed and at generator level, we can envisage the following procedure to treat real data:

The invariant mass distributions at generator level should be constructed for several points in the coannihilation region, and the procedure to determine end-points should be repeated. When real data is available, a selection procedure giving rise to a large sensitivity (for example Method 3 of Section 7.7.2) should be applied to reduce standard model background. The invariant mass distribution for simulated SM background, where the SS tau pair distribution has been subtracted from that of OS tau pairs, should be subtracted from the real data. The resulting distribution should then be compared with the distributions obtained at generator level for the different points in the coannihilation region. If a similar distribution can be found at generator level, a fit region should be chosen using the generator level distribution. A similar

fit should than be made to the real data and to the distribution of simulated events at reconstructed level.

Chapter 8

Conclusion

The main topic of this thesis has been the study of a supersymmetric decay chain involving two tau leptons. Chapter 2 and 3 gave a short introduction to the theories forming the basis on which this work is built. It was shown that the minimal supersymmertic extension of the standard model, the MSSM, provides possible solutions to some of the problems in the well established standard model.

A short description of the experimental set-up was given in Chapter 4. The installation of the ATLAS detector is now almost completed; minor parts of the muon system and the level 1 trigger system are the only remaining parts to be installed. Commissioning with cosmic rays is being carried out, and the data flow chain has been tested with real-like data. The LHC is scheduled to have its first proton-proton collision the 28th of July 2008. The analysis presented in this thesis are hence performed on simulated data. The simulation tools were described in Chapter 5.

The analysis presented in this thesis are performed on simulated data. In Chapter 6, the tau reconstruction algorithms, tauRec and tau1p3p, were discussed. Both algorithms use the hadronic decay products of taus in their reconstruction, but the approach for solving this task is different. The main difficulty in reconstruction hadronically decaying taus, is to distinguish these tau-jets from jets originating from QCD processes. In order to obtain a clean signal, both algorithms operate with a default cut on the transverse momentum of the leading charged $\pi^{\pm}$, since taus with higher energies form more collimated jets which makes them easier to distinguish from QCD-jets. The track-based tau1p3p algorithm is mainly intended to reconstruct taus in a low energy region and the default cut on the transverse momentum in

this algorithm is $p_T^{\pi^\pm} = 9$ GeV. TauRec is a calorimeter-based algorithm and it has a default cut $p_T^{\pi} = 15$ GeV.

Chapter 7 presents a study of the discovery potential in ATLAS in the mSUGRA coannihilation region. We have investigated the invariant mass distribution for taus originating from the supersymmetric decay chain $\widetilde{q} \rightarrow \widetilde{\chi}_2^0 q \rightarrow \widetilde{\tau}\tau q \rightarrow \tau\tau q\widetilde{\chi}_1^0$, in one benchmark point in the mSUGRA coannihilation region, both at generator level as well as at reconstructed level. In this decay chain, one of the taus is expected to be soft, and all samples used in the analysis therefore use the tau1p3p algorithm for reconstructing taus, due to the lower p_T threshold. This is the first study of the coannihilation region where the fully simulated standard model background has been taken into account. The study performed corresponds to ca 30 fb[1] of collected data, corresponding to three years of data taking with low luminosity running, i.e. $\mathcal{L} = 10^{33}$ cm^{-2}s^{-1}. The background is statistically limited. However, satisfying methods to reject the available background have been developed, but better statistics are required to determine which of the methods is the most performant. A sensitivity of 14 was achieved. A simple analysis of kinematic properties of the signal was performed by making linear fits to the invariant mass of the two taus. The fit parameters, i.e. slope and end-point, were compared for different distributions at generator level as well as at reconstructed level, before and after cuts had been performed to separate signal from background. We saw that even after the most drastic cuts, which gave rise to a sensitivity of 14.06, the fit parameters were in good agreement within statistical errors with those corresponding to the distribution at generator level.

The study in this thesis has also involved a study of tau leptons. The topology of taus in Monte Carlo Truth simulated events has been studied in connection with the development of a tau CSC-note, and the results are published in Ref. [46].

Bibliography

[1] L. Spergel *et al.*, "First Year Wilkinson Microwave Anisotropy Probe (WMAP) Observations: Determination of Cosmological Parameters", *Astrophys. J. Suppl. Ser.* **148** (Feb, 2003) 175, `astro-ph/0302209`.

[2] Wilkinson Microwave Anisotropy Probe (WMAP) Web-Page: `http://map.gsfc.nasa.gov/`.

[3] Particle Data Group Collaboration, "Review of Particle Physics", *J. Phys* **G33** (2006) 1–1232.

[4] F. Zwicky, "On the Masses of Nebulae and Clusters of Nebulae", *Astrophys. J.* **86** (1937) 217–246.

[5] `http://hubblesite.org/`.

[6] W. Heisenberg, *Quantentheorie und Philosophie*. Reclam, 1979.

[7] A. Einstein, "Über einen die Erzeugung und Verwandlung des Lichtes betreffenden heuristischen Gesichtspunkt", *Ann. Phys.* **17** (1905) 132.

[8] J. J. Thomson, "Cathode Rays", *Philos. Mag., Ser. 5* **44** (1897) 293–317.

[9] E. Rutherford, "The Scattering of α and β Particles by Matter and the Structure of the Atom", *Philos. Mag.* **21** (1911) 669.

[10] W. Pauli, "Dear Radioactive Ladies and Gentlemen", *Phys. Today* **31** (1978 [1930]), no. 9, 27.

[11] F. Reines and C. L. Cowan, "Detection of the Free Neutrino", *Phys. Rev.* **92** (1956) 830–831.

[12] H. M. Georgi, *Lie Algebras in Particle Physics*. Perseus, 1999.

[13] F. Mandl and G. Shaw, *Quantum Field Theory*. John Wiley & Sons, 1993.

[14] T. D. Lee and C. N. Yang, "Question of Parity Conservation in Weak Interactions", *Phys. Rev.* **104** (Oct, 1956) 254–258.

[15] P. W. Higgs, "Broken Symmetries and the Masses of Gauge Bosons", *Phys. Rev. Lett.* **13** (Oct, 1964) 508–509.

[16] S. P. Martin, "A Supersymmetry Primer", tech. rep., Sep, 1997. `hep-ph/9709356`.

[17] U. Amaldi, W. de Boer, and H. Fürstenau, "Comparison of Grand Unified Theories with Electroweak and Strong Coupling Constants Measured at LEP", *Phys. Lett. B* **260** (Mar, 1991) 447–455.

[18] S. Coleman and J. Mandula, "All Possible Symmetries of the S Matrix", *Phys. Rev.* **159** (Jul, 1967) 1251–1256.

[19] R. Haag, J. T. Łopuszánski, and M. F. Sohnius, "All Possible Generators of Supersymmetries of the S-Matrix", *Nucl. Phys. B* **88** (Nov, 1974) 257–74.

[20] J. Ellis, "Looking Beyond the Standard Model", in *Large Hadron Collider Phenomenology*, M. Krämer and F. J. Soler, eds., pp. 109–216. The Scottish Universities Summer School in Physics, 2004.

[21] M. Drees, R. M. Godbole, and P. Roy, *Theory and Phenomenology of Sparticles*. World Scientific Publishing Co. Pte. Ltd, 2004.

[22] A. Green, "Dark Matter." Presentation at the 20th Nordic Particle Physics Meeting at Spaatind, Jan, 2008.

[23] B. K. Gjelsten, D. J. Miller, and P. Osland, "Measurement of SUSY Masses via Cascade Decays for SPS 1a", *JHEP* **12** (2004) `hep-ph/0410303`.

[24] K. Hübner, "The Accelerators", in *50 Years of Research at CERN: From Past to Future*, G. Giudice, ed., pp. 1–27. CERN, May, 2006.

[25] `http://www94.web.cern.ch/ISOLDE`.

[26] L. Iconomidou-Fayard *et al.*, "Results on CP Violation from NA48 Experiment at CERN", *Int. J. Mod. Phys.* **A: 17** (2002) 3012–25, `hep-ex/0110028`.

[27] `http://ab-div.web.cern.ch/ab-div/Publications/LHC-DesignReport.html`.

[28] ATLAS Collaboration.

[29] ATLAS Collaboration, "ATLAS Detector and Physics Performance Technical Design Report", Tech. Rep. CERN-LHCC-99-014, CERN, 1999.

[30] ATLAS Collaboration, "The ATLAS Experiment at the CERN Large Hadron Collider", Tech. Rep. ATL-COM-PHYS-2007-102, CERN, Dec, 2007.

[31] ATLAS Inner Detector Community, *ATLAS Inner Detector Technical Design Report*. CERN/LHCC 97-16, 1997.

[32] ATLAS Collaboration, "ATLAS Calorimeter Performance, Technical Design Report", Tech. Rep. CERN-LHCC-96-040, CERN, 1997.

[33] B. Gjelsten, *Mass Determination of Supersymmetric Particles in ATLAS*. PhD thesis, Faculty of Mathematics and Science, University of Oslo, 2005.

[34] ATLAS Muon Collaboration, "ATLAS Muon Spectrometer Technical Design Report", Tech. Rep. CERN-LHCC-97-022, CERN, 1997.

[35] L. Johansen, *Radiation Hard Silicon Microstrip Detectors for Use in ATLAS at CERN*. PhD thesis, Department of Physics and Technology, University of Bergen, 2005.

[36] M. Dobbs, S. Frixione, E. Laenen, and K. Tollefson, "Les Houches Guidebook to Monte Carlo Generators for Hadron Collider Physics", 2004.

[37] G. Corcella *et al.*, "HERWIG 6.5: An Event Generator for Hadron Emission Reactions with Interfering Gluons (including supersymmetric processes)", *JHEP* **0101** (2001) 010, `hep-ph/0011363`.

[38] T. Sjøstrand *et al.*, "PYTHIA 6.3 Physics and Manual", `hep-ph/0308153`.

[39] `http://atlas-sw.cern.ch/cgi-bin/viewcvs-atlas.cgi/offline/Generators/DC3_joboptions/share`.

[40] S. Jadach, J. H. Kühn, and Z. Was, "TAUOLA: A Library of Monte Carlo Programs to Simulate Decays of Polarized τ Leptons", *Comput. Phys. Commun.* **64** (Sep, 1990) 275–299.

[41] A. Rimoldi and A. Dell'Acqua, "The Full Detector Simulation for the ATLAS Experiment: Status and Outlook", tech. rep., CERN, Jun, 2003. `physics/0306086`.

[42] `https://twiki.cern.ch/twiki/bin/view/Atlas/WorkBookFullChain`.

[43] `http://www.hep.ucl.ac.uk/atlas/atlfast/`.

[44] D. Cavalli *et al.*, "Performance of the ATLAS Fast Simulation ATLFAST", Tech. Rep. ATL-COM-PHYS-2007-012, CERN, Jan, 2007.

[45] R. Brun, F. Rademakers, P. Canal, I. Antcheva, and D. Buskulic, *ROOT Users Guide*, 5.12 ed., July, 2006.

[46] C. Adorisio *et al.*, "Identification of Hadronic Tau Decays with ATLAS Detector", Tech. Rep. ATL-COM-PHYS-2007-066, CERN, Sep, 2007.

[47] M. L. Perl *et al.*, "Evidence for Anomalous Lepton Production in $e^+ - e^-$ Annihilation", *Phys. Rev. Lett.* **35** (Dec, 1975) 1489–1492.

[48] E. Richter-Was and T. Szymocha, "Hadronic τ Identification with Track Based Approach: The $Z \to \tau\tau$, $W \to \tau\nu$ and Di-Jet Events from DC1 Data Samples", Tech. Rep. ATL-PHYS-PUB-2005-005, CERN, Feb, 2005.

[49] B. K. Bulloch, K. Hagiwara, and A. D. Martin, "Tau Polarization and Its Correlations as a Probe of New Physics", *Nuclear Physics B* **395** (May, 1993) 499–533.

[50] D. Froidevaux, "Particle Reconstruction and Identification." CERN-FNAL 2nd Hadron Collider Summer School, June, 2007.

[51] M. Heldmann and D. Cavalli, "An Improved τ-Identification for the ATLAS Experiment", Tech. Rep. ATL-PHYS-PUB-2006-008, CERN, Dec, 2005.

[52] O. Øye and A. Lipniacka, "ATLAS Soft Tau Reconstruction Performance in the mSUGRA Stau Coannihilation Region", Tech. Rep. ATL-PHYS-PUB-2006-021, CERN, May, 2006.

[53] A. Raklev, *Supersymmetric Cascade Decays at the LHC*. PhD thesis, Department of Physics and Technology, University of Bergen, 2007.

[54] R. Arnowitt *et al.*, "Detection of SUSY Signals in Stau Neutralino Coannihilation Region at the LHC", *AIP Conf. Proc.* **903** (Nov, 2006) 229–232, `hep-ph/0611089`.

[55] H. W. Baer and C. Balzs, "χ^2 Analysis of the Minimal Supergravity Model Including WMAP, $g_\mu - 2$ and $b \to s\gamma$ Constraints", *J. Cosmol. Astropart. Phys.* **305** (Mar, 2003) 6, `hep-ph/0303114`.

[56] K. Griest and D. Seckel, "Three Exceptions in the Calculation of Relic Abundances", *Phys. Rev.* **D43** (1991) 3191–3203.

[57] `http://cern.ch/kraml/comparison/`.

[58] B. C. Allanach, S. Kraml, and W. Porod, "Theoretical Uncertainties in Sparticle Mass Predictions From Computational Tools", *JHEP* **03** (2003) 016, `hep-ph/0302102`.

[59] G. Belanger, S. Kraml, and A. Pukhov, "Comparison of SUSY Spectrum Calculations and Impact on the Relic Density Constraints from WMAP", *Phys. Rev.* **D72** (2005) 015003, `hep-ph/0502079`.

[60] A. Kaczmarska, E. Richter-Was, M. Wolter, and L. Janyst, "Performance of the Tau1p3p Algorithm for Hadronic Tau Decays Identification with Release 12.0.6", Tech. Rep. ATL-COM-PHYS-2007-039, CERN, 2007.